Ministry of Higher Education & Scientific Research

Abdelhamid ben Badis University

Faculty of Exact Sciences and Computer Science

Mostaganem

Doctoral thesis

Field: Chemistry

Major: Physical Chemistry

Presented by

DAIKH ZINE EDDINE

Entitled

Design of nanoparticles from amphiphilic templates

Supported on: 21/05/2026

Before the jury :

Mr Belalia Mahmoud,	**Professor and Chair,**	**University of Mostaganem**
Mr Harrane Amine,	**Professor and Examiner,**	**University of Mostaganem**
Mr AZAYEZ Mansour,	**PhD (MCA), Examiner,**	**University of Chlef**
Mr BOUHADDA Youcef,	**Professor and Co-Director of Thesis,**	**University of Mascara**
Mrs FERGOUG Teffaha,	**Professor and Director of Thesis,**	**University of Mascara**

DEDICATIONS

I dedicate this success to my dear father and mother and brother, who allowed me to discover this world and gave me their unfailing support. With the patience and confidence, you have always placed in me, you have allowed me to move forward with peace of mind. I hope that they will find in this modest work a reward for what they have done, and I ask their forgiveness for all the moments of tension that I caused at home.

To all my loved ones, friends and family, I wish you every success and happiness.

I would like to dedicate this work in particular to my dear professors Fergoug Teffaha, Bouhadda Youcef, and Reguig Abd el Karim and benmouhamed abdelmajid .

Without forgetting my colleagues beki kjaled and aribi rachida and kadiri aicha and Saidi Fatima and chatar Fatima and dadouche meryem

ACKNOWLEDGMENTS

To God, who gave me the strength, courage, and health to make this dream come true. And Before presenting the research work carried out, I would like to express my gratitude to all those who made this thesis possible.

The research presented in this thesis was conducted at the Research Laboratory of Physical Chemistry of Macromolecules and Biological Interfaces, Mustapha Stambouli University Mascara, successively headed by Ms. FERGOUG taffeha my thesis supervisor, who agreed to supervise me throughout my work. First of all, thank you for placing your trust in me on this project that was so important to you, which enabled me, with your support and scientific expertise, to successfully complete this work. Thank you, Madam, for your daily availability, despite your busy schedule, for all the professional and personal discussions we had, for all the hours you spent correcting the manuscript, my reports, my letters, and helping me prepare my oral presentations. Thank you very much for your support and patience, your good humour and kindness, and above all for your friendship! I would also like to thank Mr. BOUHADDA Youcef, Professor at Mustapha Stambouli Mascara University, co-director of my thesis. Thank you for everything you have given me and taught me during my thesis, finaly I would like to thank them both for welcoming me to the laboratory.

I would like to express my sincere gratitude to Mr. reguig abdelkarim , Professor at the University of Mustapha Stambouli , for his wise advice and his particular kindness.

We should not forget those who have been a source of great support to us, our doctors: Khaled SEBAKHY; Mustapha EL HARIRI EL NOKAB; Khaled DERKAOUI

Abstract:

Silica nanoparticles (SiNPs) are highly promising nanocarriers for biomedical applications, particularly in drug delivery and adsorbtion, due to their well-controlled size, porous structure, and tunable surface properties. This study investigates two distinct synthesis approaches: (i) a sustainable, low-temperature aqueous sol-gel method for producing SiNPs in the 500–700 nm range, and (ii) a water-in-oil (W/O) microemulsion technique that employs surfactants and co-surfactants to precisely regulate nanoparticle formation. The study emphasizes the significant influence of surfactant selection—comparing cationic cetyltrimethylammonium bromide (CTAB) and non-ionic Triton X-100 (TX-100)—on SiNP size, stability, and dispersity, thereby offering a highly tunable strategy for nanoparticle morphology control. Comprehensive characterization using dynamic light scattering (DLS), scanning electron microscopy (SEM), X-ray diffraction (XRD), Brunauer-Emmett-Teller (BET) surface area analysis, solid-state nuclear magnetic resonance (ssNMR), X-ray photoelectron spectroscopy (XPS), and photoluminescence (PL) confirmed the successful synthesis and structural properties of SiNPs. The TX-100-mediated microemulsion method proved particularly effective in achieving highly stable, reproducible, and monodisperse SiNPs, with a size limit of approximately 100 nm, making them ideal candidates for drug encapsulation. The successful incorporation of procaine (PRC) into TX-100-derived SiNPs further highlights the crucial role of surfactant-stabilized interfaces in modulating the hydrolysis and condensation of tetraethyl orthosilicate (TEOS), thereby enhancing drug loading efficiency. Moreover, the study underscores the importance of reverse micelle dynamics in nanoparticle synthesis, providing a robust framework for further optimization of SiNP-based drug carriers with improved stability and bioavailability. Overall, this work highlights the critical role of surfactant and medium selection in SiNPs synthesis, demonstrating their impact on nanoparticle stability, dispersity, and drug loading efficiency. The TX-100-mediated microemulsion technique emerges as a superior approach for producing stable, monodisperse SiNPs, advancing the design of nanocarriers for procaine drug delivery applications as well using this SiNPs in adsorption of dyes to minimize a water pollution.

Keywords: Particle size tuning, silica nanoparticles (SiNPs), nanocarriers, CTAB and TX-100 micelles, microemulsion, Procaine drug, adsorbtion.

Résumé :

Les nanoparticules de silice (SiNPs) sont des nanotransporteurs très prometteurs pour les applications biomédicales, en particulier dans l'administration et l'adsorption de médicaments, en raison de leur taille bien contrôlée, de leur structure poreuse et de leurs propriétés de surface ajustables. Cette étude examine deux approches de synthèse distinctes : (i) une méthode sol-gel aqueuse durable à basse température pour produire des SiNPs dans la gamme 500-700 nm, et (ii) une technique de microémulsion eau-dans-huile (W/O) qui utilise des tensioactifs et des co-tensioactifs pour réguler avec précision la formation des nanoparticules. L'étude souligne l'influence significative du choix du tensioactif — en comparant le bromure de cétyltriméthylammonium cationique (CTAB) et le Triton X-100 non ionique (TX-100) — sur la taille, la stabilité et la dispersibilité des SiNPs, offrant ainsi une stratégie hautement modulable pour le contrôle de la morphologie des nanoparticules. Une caractérisation complète à l'aide de la diffusion dynamique de la lumière (DLS), de la microscopie électronique à balayage (MEB), de la diffraction des rayons X (DRX), de l'analyse de la surface spécifique selon la méthode de Brunauer-Emmett-Teller (BET), de la résonance magnétique nucléaire à l'état solide (ssNMR), de la spectroscopie photoélectronique à rayons X (XPS) et de la photoluminescence (PL) a confirmé la synthèse réussie et les propriétés structurelles des SiNPs. La méthode de microémulsion médiée par TX-100 s'est avérée particulièrement efficace pour obtenir des SiNPs hautement stables, reproductibles et monodispersées, avec une taille limite d'environ 100 nm, ce qui en fait des candidates idéales pour l'encapsulation de médicaments. incorporation réussie de la procaïne (PRC) dans les SiNPs dérivées du TX-100 souligne encore davantage le rôle crucial des interfaces stabilisées par des tensioactifs dans la modulation de l'hydrolyse et de la condensation de l'orthosilicate de tétraéthyle (TEOS), améliorant ainsi l'efficacité de la charge médicamenteuse. De plus, cette étude souligne l'importance de la dynamique des micelles inversées dans la synthèse des nanoparticules, fournissant ainsi un cadre solide pour l'optimisation des vecteurs médicamenteux à base de SiNPs avec une stabilité et une biodisponibilité améliorées. Dans l'ensemble, ces travaux mettent en évidence le rôle essentiel du choix des tensioactifs et des milieux dans la synthèse des SiNPs, démontrant leur impact sur la stabilité, la dispersibilité et l'efficacité de chargement des nanoparticules. La technique de microémulsion médiée par TX-100 apparaît comme une approche supérieure pour produire des SiNPs stables et monodispersées, faisant progresser la conception de nanotransporteurs pour les applications d'administration de procaïne, ainsi que l'utilisation de ces SiNPs dans l'adsorption de colorants afin de minimiser la pollution de l'eau.

Mots clés: Ajustement de la taille des particules, nanoparticules de silice (SiNPs), nanotransporteurs, micelles CTAB et TX-100, microémulsion, médicament procaïne, adsorption.

ملخص :

تعد جزيئات السيليكا النانوية ((SiNPsناقلات نانوية واعدة للغاية للتطبيقات الطبية الحيوية، لا سيما في توصيل الأدوية وامتصاصها، وذلك بفضل حجمها الذي يمكن التحكم فيه جيدًا، وبنيتها المسامية، وخصائص سطحها القابلة للتعديل. تبحث هذه الدراسة في طريقتين مختلفتين للتوليف: (1) طريقة سول-جيل مائية مستدامة ومنخفضة الحرارة لإنتاج SiNPs في نطاق 500-700 نانومتر، و(2) تقنية مستحلب دقيق مائي في زيتي ((W/Oتستخدم مواد خافضة للتوتر السطحي ومواد مساعدة خافضة للتوتر السطحي لتنظيم تكوين الجسيمات النانوية بدقة. تؤكد الدراسة على التأثير الكبير لاختيار المادة الخافضة للتوتر السطحي — بمقارنة بروميد السيتيل تريميثيل الأمونيوم الكاتيوني CTAB وTriton X-100 غير الأيوني على حجم SiNPs واستقراره وتشتته، مما يوفر استراتيجية قابلة للتعديل بدرجة عالية للتحكم في شكل الجسيمات النانوية. أكدت الخصائص الشاملة باستخدام التشتت الضوئي الديناميكي ((DLSوالمجهر الإلكتروني الماسح ((SEMوالانعكاس بالأشعة السينية ((XRDوتحليل مساحة السطح بروناور-إيميت-تيلر ((BETوالرنين المغناطيسي النووي للحالة الصلبة ((ssNMRوالتحليل الطيفي للضوء بالأشعة السينية ((XPSوالتلألؤ الضوئي ((PLنجاح التوليف والخصائص الهيكلية ل .SiNPs, أثبتت طريقة الميكروإمولسيون بوساطة TX-100 فعاليتها بشكل خاص في الحصول على جزيئات SiNPs عالية الاستقرار وقابلة للتكرار ومتجانسة الحجم، مع حد أقصى لحجمها يبلغ حوالي 100 نانومتر، مما يجعلها مرشحة مثالية لتغليف الأدوية. إن الدمج الناجح للبروكايين ((PRCفي SiNPs المشتقة من TX-100 يسلط الضوء بشكل أكبر على الدور الحاسم للواجهات المستقرة بالسطح في تعديل التحلل المائي والتكثيف لثلاثي إيثيل أورثوسيليكات ((TEOS، وبالتالي تعزيز كفاءة تحميل الدواء. علاوة على ذلك، تؤكد الدراسة على أهمية ديناميكيات المذيلات العكسية في تخليق الجسيمات النانوية، مما يوفر إطارًا قويًا لمزيد من التحسين لحاملات الأدوية القائمة على SiNPs مع تحسين الاستقرار والتوافر البيولوجي. بشكل عام، يسلط هذا العمل الضوء على الدور الحاسم للسطح الفعال واختيار الوسط في تخليق SiNPs، مما يدل على تأثيرهما على استقرار الجسيمات النانوية وتشتتها وكفاءة تحميل الدواء. تبرز تقنية الميكروإمولسيون بوساطة TX-100 كنهج متفوق لإنتاج جزيئات SiNPs مستقرة ومتجانسة، مما يعزز تصميم ناقلات النانو لتطبيقات توصيل عقار البروكين، فضلاً عن استخدام جزيئات SiNPs هذه في امتصاص الأصباغ لتقليل تلوث المياه.

الكلمات المفتاحية: ضبط حجم الجسيمات، جسيمات السيليكا النانوية SiNPs ، ناقلات نانوية، مذيلات CTAB و TX-100، مستحلب دقيق، عقار بروكايين، امتصاص.

List of abbreviations and symbols

BET: Brunauer, Emmett and Teller

CMC : critical micellar concentration

CPT : camptothecin

CTA : tension actives concentration

CTAB : Cetyltrimethylammonium Bromide

D.I water : Deionized water

Dh: The hydrodynamic diameter

DLS: Dynamic light scattering

Ems: electron microscopes

EO : ethylene oxide

HMSNs : hollow mesoporous silica

IR : infrared

LSiNPs : Large Solide Silica spheres

M(OR)m : alkoxides

MCM-41 : mesoporous silica

MSNs : mesoporous silica nanoparticles

NMR: nuclear magnetic resonance spectroscopy

O/W : oil-in-water

PCS : photon correlation spectroscopy

PDI: particle dispersion index

PL: Photoluminescence Spectroscopy

PRC: Procaine

R : the perfect gas constant

SEM: scanning electron microscopy

SiNPs : Silica nanoparticles

T : temperature

TA : tension actives

TEM: transmission electron microscopy

TEOS : tetraethoxysilane

Tf: fusion temperature

Tk: The Krafft temperature

TX-100 : Triton X-100

UV : ultraviolet

VB : brilliant vert

W/O : water-in-oil

XPS: X-ray Photoelectron Spectroscopy

XRD: X-ray diffraction

γ : interfacial tension

FIGURES LIST:

TABLES LIST :

INDEX:

General introduction:

The field of biomedical engineering and nanotechnology has witnessed remarkable advancements, bringing profound changes to multiple industries by enabling the manipulation of materials at the nanoscale. Silica nanoparticles (SiNPs) defined as promising and attractive type of inorganic nanocarriers, among the diverse range of nanoparticles, have drawn significant interest because of their unique characteristics and their versatility across a wide range of applications, encompassing catalysis, sensing, separation methods[1][2], drug delivery[3], excellent biocompatibility[4], and biodegradability[5], their significant interest is due to their unprecedented internal surface area and pore volume, adjustable pore dimensions, stable colloidal properties, and the potential for targeted modifications on both the inner (pore) surfaces and the external particle surface.[6] Stöber process is used for synthesizing the SiNPs through the implementation of soft template (micelle) strategies, this method involves the hydrolysis of tetraethoxysilane (TEOS) either in an alcohol-water solution[7] or exclusively in a water-based solution, followed by the condensation of the resulting silanols.[8] Typically, ammonia solution or sodium hydroxide is employed to regulate the pH of the medium, aiming for a pH level within the range of 11-13.[9] Considerable advancements have been achieved in regulating the properties of mesoporous and nonporous silica nanoparticles[10], particularly concerning particle size and pore structure[11]. The synthesis of these materials entails the condensation of hydrolyzed silicate species around a supra-micellar assembly of cylindrical ionic and nonionic surfactant micelles, which serve as templates. This procedure is contingent on various experimental factors, including pH, temperature, the nature, and concentration of silicate precursors, as well as the choice of surfactant.[10],[12],[13] However, no straightforward method currently exists for reliably controlling particle diameters across a spectrum of sizes. The existing approaches rely on manipulating various parameters to achieve this goal. In both acidic[14][15] and basic media[16][17], the effect of the silicate/surfactant ratio[18][19], solvent content, temperature, (co)-surfactants, organic and inorganic additives or type of cosolvents was investigated and various particle morphologies have been so far prepared.[20][14] The various methods mentioned previously to control particle size of SiNPs to less than 100 nm all impact the supramicellar assembly through the charge screening effect of cylindrical micelles. Different concentrations of the base catalyst result in different rates of condensation, and because of silica's isoelectric point at pH ≈ 2, these species become deprotonated (charged), which significantly influences the aggregation number of

supramicellar assemblies.[21] [22]Moreover, the interplay between the supramicellar assembly process and the rate of silica formation is further influenced by the concentrations of the surfactant and silicate precursor. Consequently, the structural stability of the supramicellar assembly, including its aggregation number, and ultimately, the particle size, is highly responsive to alterations in the reaction conditions, which justifies the size of silica nanoparticles obtained in the Stöber synthesis which typically falls within the range of 20 to 800 nm.[23][24] In a different research investigation, reverse microemulsion, involving the dispersion of water in oil, has been employed for nanoparticle structural manipulation and functionalization, creating significant prospects for enhancing drug delivery [25]. Within the realm of microemulsion and reverse microemulsion synthesis, the manipulation of the interface between the water and oil phases through surfactants plays a pivotal role in governing the size, shape, and stability of droplets. In the production of SiNPs, renowned for their versatility among inorganic nanoparticles, a substantial body of research has documented their synthesis using the reverse microemulsion approach.[26][27] In many microemulsion synthesis processes that were reported in literature, Triton X-100 (TX-100) stands as the preferred surfactant.[28][29] TX-100 is a non-ionic surfactant characterized by its composition: it features hydrophilic ethylene oxide (EO) units at one end and a hydrophobic end that comprises an aromatic group with an attached alkyl chain. The diversity in TX-100 composition originates from variations in the number of repeating EO units, their polydispersity, and the structure of the alkyl chain linked to the aromatic group. Several studies have highlighted how subtle changes in the structure of TX-100-based micelles, the choice of co-surfactants, and the molar ratios of the three phases (water/oil/alkanol) can lead to alterations in the morphology of SiNPs, affecting their size, shape, and polydispersity.[30],[31] However, through microemulsion synthesis, CTAB was also the surfactant of choice. highlight, a quaternary ammonium compound extensively employed as a surfactant in the synthesis of mesoporous silica nanoparticles (MSNs), hollow mesoporous silica (HMSNs) and core-shell MSNs.[32][33] Schacht and coworkers [34] were the pioneers in showcasing the synthesis of micrometer-sized mesoporous ordered hollow spheres through interfacial reactions in emulsions, utilizing CTAB as the templating surfactant, but the drawback of the process was that it was time-consuming. Methods for producing nanospheres encompass both hard templating and soft templating approaches. Within these methods, the soft-templating approach stands out as the most appealing option due to its advantages of streamlined production procedures, cost-effectiveness, and suitability for large-scale manufacturing. Nonetheless, soft-templating techniques frequently exhibit inconsistent results, even when employing identical chemical reagents, leading to reduced

reproducibility. This inconsistency is likely attributed to the substantial impact of interfacial interactions among solvents and surfactants.[35] In the realm of nanotechnology, the encapsulation process involves ingeniously incorporating therapeutic agents, such as Procaine local anesthetic, which plays a pivotal role in numerous crucial therapeutic procedures,[36], elaborating its extensive application in the field of medicine, renowned for its lower neurotoxicity compared to other local anesthetics commonly employed in clinical settings.[37],[38] Additionally, procaine exhibits numerous commendable attributes, including notable water solubility and a comparatively rapid decomposition rate.[39] In the context of general anesthesia or postoperative intravenous analgesia, procaine further presents distinctive advantages such as quick awakening, minimal hepatotoxicity[40], effective analgesia [41],[42], and reduced postoperative discomfort[43], loaded inside nanoparticles, paving the way for a new frontier in drug delivery systems with enhanced precision and efficiency

The problem is even more acute in the case of industrial effluents, which have a much more pronounced toxic character. The dyes and additives used by the textile industries can pose a serious threat to the environment, as their presence in water, even in very small quantities, is highly visible and undesirable; consequently, their presence in aquatic systems reduces light penetration and thus retards photosynthetic activity. They also have a tendency to complex metal ions, producing micro-toxicity for wildlife and other organisms.

With this in mind, we set out to study the removal of two non-ionic food colorants, cationic Carmine and brilliant vert (VB) in aqueous solution, by a silica-based nanoparticle (NPS).

The initial section of this chapter will focus on fundamental principles concerning emulsions and microemulsions. Subsequently, the second part will detail the procedure for synthesizing silica nanoparticles through the conventional Stöber method. To begin, We'll explore the notion of colloidal silica, examining its characteristics and various practical uses, and we will delve into the basics of the sol-gel process to elucidate the underlying principles governing the synthesis of silica nanoparticles. Next, we will examine the structural properties of reverse micelles as a specific case study. Following that, we explore how reverse micellar systems can be utilized to produce silica nanoparticles through the hydrolysis-condensation of alkoxysilane precursors. In wrapping up this chapter, we delve into an examination of the consistent production of size-regulated silica nanoparticles via microemulsion synthesis.

The synthesis and characterization of silica nanoparticles require a well-defined methodology, precise selection of reagents, and advanced analytical techniques to ensure reproducibility and

comprehensive understanding of the material properties. The second chapter details the experimental procedures employed in the preparation of silica nanoparticles, along with the chemical reagents used.

A range of characterization techniques was utilized to evaluate the physicochemical properties, morphology, surface structure, and functional attributes of the synthesized nanoparticles. Dynamic Light Scattering (DLS) was used to determine particle size distribution and polydispersity index, providing insight into the stability of the colloidal suspension. Electron microscopy techniques, including Scanning Electron Microscopy (SEM), were employed to investigate the morphology and aggregation behavior of the nanoparticles at the nanoscale.

Structural and textural properties were analyzed using X-ray Diffraction (XRD) to assess crystallinity, while Brunauer–Emmett–Teller (BET) surface area analysis provided information on porosity and specific surface area. X-ray Photoelectron Spectroscopy (XPS) was conducted to study the surface chemistry and elemental composition of the silica nanoparticles. Furthermore, Photoluminescence Spectroscopy was performed to explore optical properties, which can be significant for applications in sensing and bioimaging. Nuclear Magnetic Resonance (NMR) spectroscopy was utilized to characterize the chemical environment of silicon and identify potential functional groups within the synthesized materials.

The chapter three explores the synthesis of silica nanoparticles (SiNPs) under varying conditions, including synthesis temperature, template concentration, pH levels, and preparation media. These parameters significantly influence particle size, morphology, and dispersion stability. A systematic investigation was conducted to optimize synthesis conditions and achieve well-defined nanoparticles. Additionally, comprehensive characterization was performed to evaluate the structural, morphological, and surface properties of the synthesized SiNPs, providing insight into their potential applications.

The chapter four investigates the potential of silica nanoparticles (SiNPs) for environmental and biomedical applications. First, the adsorption efficiency of SiNPs for dye removal is explored, highlighting their role in wastewater decontamination. Various factors influencing adsorption performance, such as surface properties and interaction mechanisms, are examined. Additionally, the ability of SiNPs to encapsulate drugs is assessed, emphasizing their potential in drug impregnation. Through these studies, the multifunctionality of SiNPs in both environmental remediation and pharmaceutical applications is demonstrated.

I. Chapter 01: Fundamentals of micellar system aqueous, Emulsions, Microemulsions, for Silica Nanoparticle Synthesis

I.1 Introduction:

There is a very specific type of chemical substance that is both soluble in water and soluble in hydrocarbon or vegetable oils. In a world of technological superlatives, they have recently been called "supermolecules." precisely because of their extraordinary properties and endless practical applications. After reading the title of this thesis, the reader will understand that it deals with surfactants, traditionally called "surface-active agents," which form micelles at a certain concentration. "surfactant" It defines the properties of these substances particularly well: they are compounds that have surface activity. The word surfactant is therefore more precise than surface agent, and is above all much more general than the old word "tensioactive," which literally means "producing an effect on tension." Today, we know of surfactants that are not used for their effect on tension and that can produce emulsifying effects. These microemulsions will be used as templates to make silica nanoparticles which has numerous applications in industry as well as in many scientific fields, such as heterogeneous catalysis, electrochemistry, analytical chemistry, and molecular biology like drug delivery.

I.2 General concepts of aqueous micellar systems, emulsions, and microemulsions.

Classical micelles represent dispersed colloidal systems resulting from the spontaneous organization of surfactant molecules. These molecules, characterized by a dual nature with hydrophobic tails and hydrophilic heads, In fact, when dissolved in water, these molecules adopt a conformation designed to reduce unfavorable interactions between the the hydrophobic part and water. Generally spherical systems in the nanometer range are formed spontaneously **(Figure I.1)**

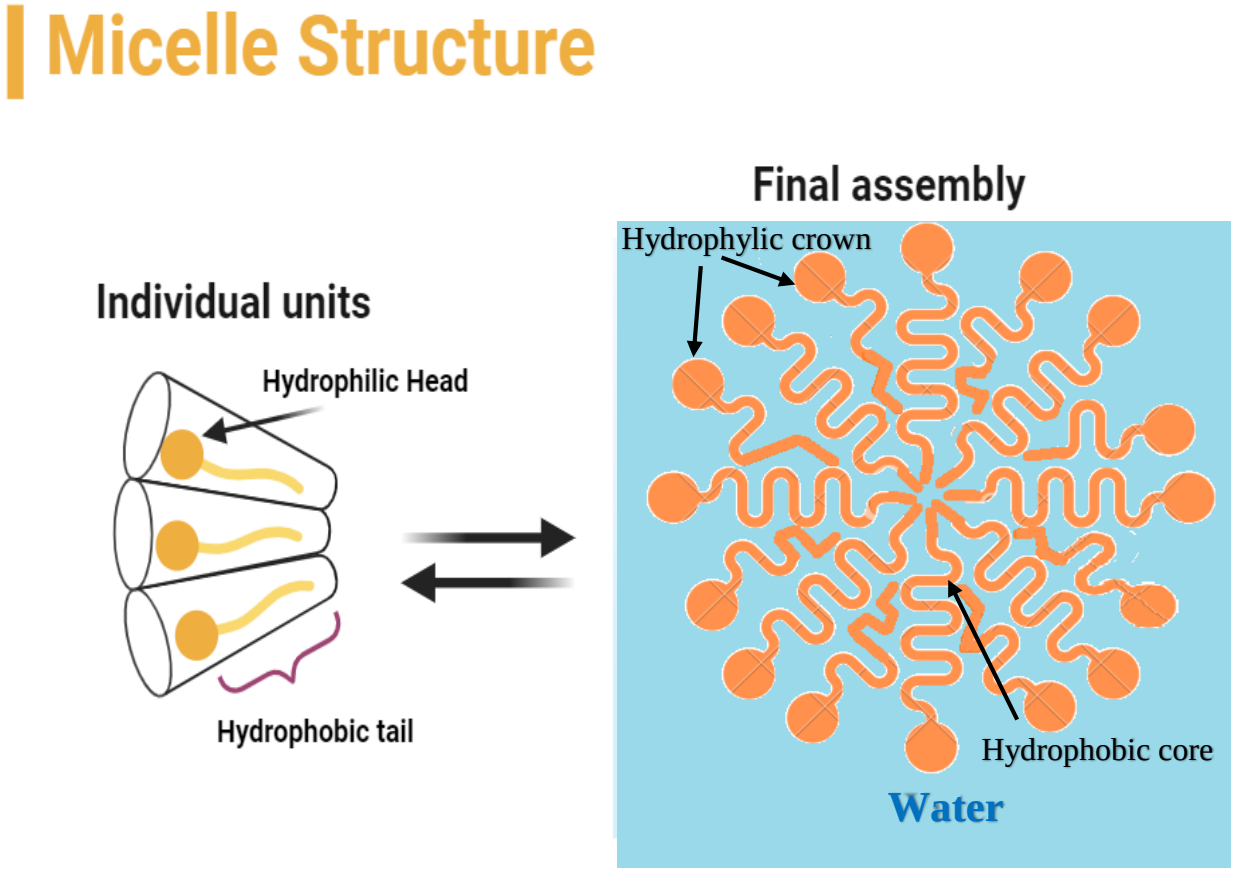

Figure I.1: Diagram of a molecular surfactant and its organization into self-assembled structures within an aqueous environment.

These systems, known as tension actives (TA) micelles, consist of a hydrophobic core and a hydrophilic crown. However, their formation depends on certain conditions such as temperature and concentration. As illustrated in **Figure I.2,** at low concentrations, amphiphilic molecules are dispersed in isolation in water. The accumulation of TA at at the water/air interface gradually lowers the surface tension to a minimum value corresponding to interface saturation. Above this concentration, the TA will organize themselves into micelles. The concentration at which micelles begin to form is called CMC (critical micellar concentration). the concentration at which micelles begin to form **(Figure I.2).**[44][45]

Emulsions and microemulsions are liquid-liquid dispersions. Taking water and oil as reference phases, two types of emulsion can be distinguished: oil-in-water (O/W) emulsions, in which water is the continuous external medium, and their symmetrical counterparts, water-in-oil (W/O) emulsions, in which oil is the dispersant medium.

For emulsions, the size of the dispersed phase is generally between 200 and 10,000 nm. They are characterized by the large number of interfaces separating the two immiscible liquid media. They are therefore thermodynamically unstable systems that tend to revert to the situation where two distinct phases coexist, separated by a limited interfacial zone. To make them stable, it is therefore necessary to add a surfactant or a surfactant/cosurfactant pair whose role is to lower the interfacial tension $\boldsymbol{\gamma}$ by adsorbing at the interface between the two liquids[46]**.** Depending on the experimental conditions, the water/surfactant(s)/oil mixture, which now appears visually single-phase, becomes isotropic and low-viscosity.

Called a microemulsion by Schulman et al[47]. This type of mixture was only demonstrated in 1943, when Hoar and Schulman obtained a translucent solution by gradually adding a co-surfactant, hexanol, to the turbid water/surfactant/oil mixture[48]. Thermodynamically stable, microemulsions are composed of a continuous phase containing a dispersed phase of small dimensions, less than 100 nm, whose coalescence is slowed by the presence of the surfactant film at the interface with the continuous phase. The size and morphology of the dispersed phase as well as the macroscopic properties of the microemulsion such as stability, viscosity or conductivity are mainly governed by two types of variables[49] :

- Composition variables: relative percentages of the system's three main constituents, i.e. water phase, oil phase and surfactant(s).
- Formulation variables: nature of surfactant and oil, ionic strength of water, temperature, for example.

I.2.1 Surfactants and aggregate formation

A molecule is considered surface-active if it has the ability to decrease the tension present at the interface between two different media (liquid/gas, liquid/liquid, liquid/solid). it enhances the affinity of two immiscible phases, and in certain instances facilitates the dispersion of one phase within the other. This characteristic behavior of surfactants arises from their amphiphilic properties, with a structure comprising a segment soluble in aqueous solvents and another segment exhibiting a pronounced affinity for organic solvents.

In aqueous or organic solutions, surface-active molecules combine to provide a favorable environment for each of their two parts. **Figure I.2** describes the empirical evolution of surface tension (γ) as a function of surfactant concentration (C_{TA}) It demonstrates that γ initially

decreases, until it reaches a minimum value when C_{TA} becomes equal to a concentration called the critical micellar concentration (cmc). Above cmc, surface tension remains almost constant.

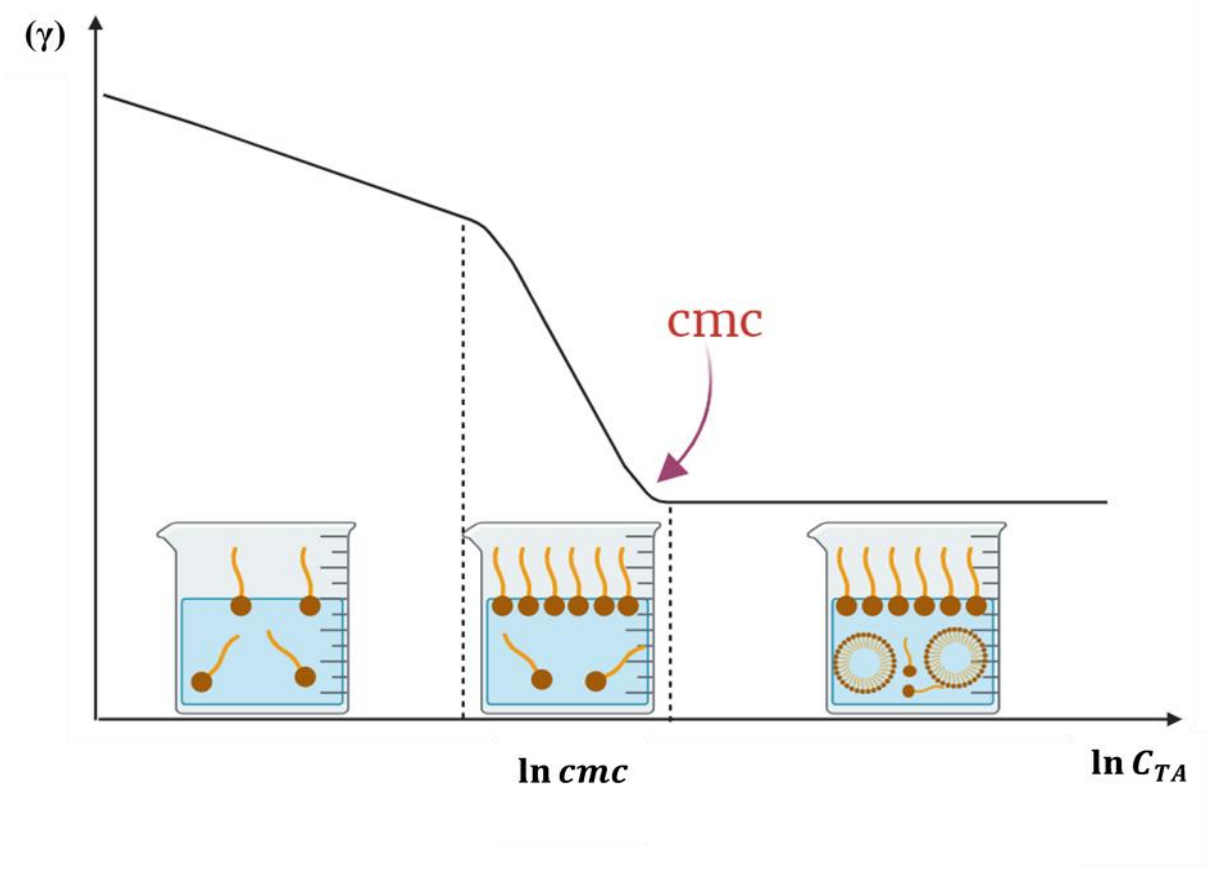

Figure I.2: Variation in surface tension as a function of surfactant concentration

According to Gibbs' fundamental equation for surface effects[50] (Equation I-1), the minimum value of γ is equal to $\Gamma_{TA}RT$ with R the perfect gas constant and T the temperature.

$$\frac{d\gamma}{d\ln C_{TA}} = -\Gamma TART \quad \text{Equation I-1}$$

This relationship means that the surface concentration of surfactant Γ_{TA} becomes invariant when C_{TA} is equal to cmc. Once surpassing the critical micelle concentration (CMC), surface-active molecules lose the ability to intercalate at the interface, leading them to spontaneously form aggregates known as micelles.

Similarly, when surface-active molecules are introduced into a water-in-oil or oil-in-water mixture, they will intercalate at the water/oil interface[51]. The hydrophilic heads maintain contact with the water while the lipophilic tails stay in contact with the oil, facilitating the dispersion of one liquid within the other, contingent upon experimental parameters. The interfacial tension between the two liquids has the potential to decrease significantly ($\gamma << 10^{-3} N/m$), As a result, minimal agitation is needed for the mixture to spontaneously transition into a highly refined, transparent, and enduring dispersion known as a microemulsion[52]. This transformation can be seen as the generation of a pseudo-phase[53] Comprised of aggregates formed through the self-organization of surfactant molecules.

Figure I.3's water/surfactant/oil ternary diagram illustrates that when surfactant proportions are low and water concentrations are high, direct micelles, characterized by spherical or cylindrical aggregates, are formed. These structures consisting of oil stabilized by a surfactant interfacial layer. Conversely, when oil concentrations are high, reverse micelles, also exhibiting spherical or cylindrical aggregates, are formed. On this occasion, water is enveloped and stabilized by an interfacial layer of surfactant. Between the areas where direct and reverse micelles form, there exists a bicontinuous phase where water and oil domains intertwine, resembling spongy microstructures. Underneath the region spanning from direct to reverse micelles, the water/surfactant/oil combination displays a series of phase equilibria referred to as the Winsor zone[49][54][55]. The single-phase microemulsion (Winsor IV) coexists with either the oil phase (Winsor I), the water phase (Winsor II) or both (Winsor III). As surfactant concentration increases, other larger structures appear. These include lamellar, cubic and hexagonal structures.

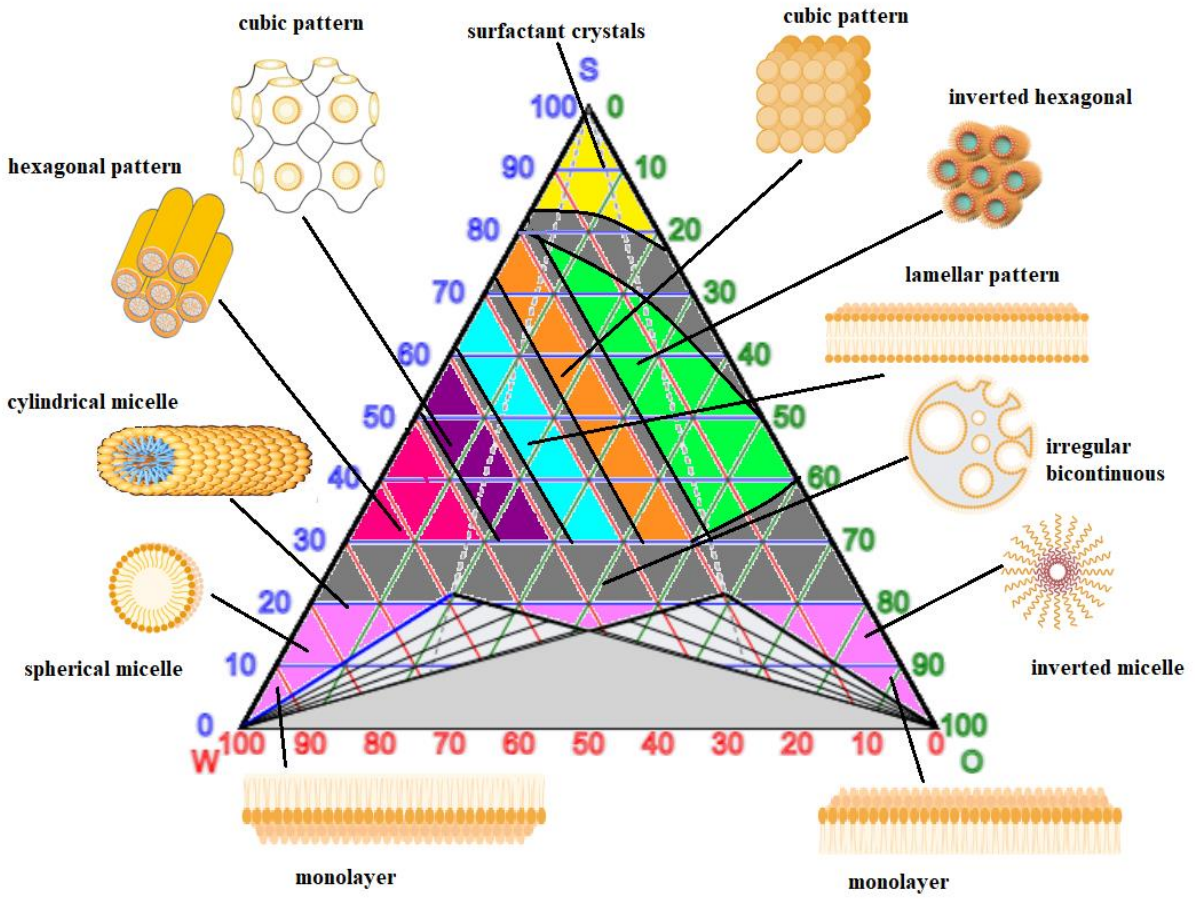

Figure I.3: Water/surfactant/oil ternary diagram

In addition to the ratio of constituents, various parameters may impact the self-assembly of surfactant molecules within the mixture. These factors encompass the chemical composition of both the hydrophilic and lipophilic segments of the surfactant, their geometric configuration, and the respective significance of each component.

I.3 General information on sol-gel methods:

The foundations of the sol-gel process were established in 1845 by J. J. Ebelmen[56], with the first practical application emerging in the 1930s through a patent by the German company Schott for producing rear-view mirrors in 1939[57]. This technique allows for the production of inorganic materials through hydrolysis and condensation reactions of metal alkoxides or other organometallic compounds, typically at lower temperatures than those required by traditional ceramic or glass manufacturing methods. The sol-gel process can create transparent inorganic or hybrid polymers with adjustable porosity, allowing for doping with different substances to achieve specific optical characteristics.

Due to its low production temperature and solvent processing, the sol-gel method enables the incorporation of compounds with low thermal stability, and even facilitates the inclusion of microorganisms[58][59]. Although silicon-based precursors are the least expensive, the cost of precursors for the sol-gel process remains relatively high. For instance, silica glass manufactured through the sol-gel method is priced approximately 100 times higher than its fused alternative.

I.3.1 The fundamentals of sol-gel chemistry

Sol-gel synthesis of ceramics is generally based on alkoxides of formula M(OR)m or R' nm(OR)m where M is usually a metal (typically Al, Ti, Zr, V), or silicon (in our case). where R and R'are organic groups of the CnH2n+1 alkyl type, for example[60][61][62].

Typically, the R' chain remains intact throughout the process and is consequently present in the final material. There exists the potential to introduce functionalities onto the R' chain, such as an amine or epoxy function, to introduce novel properties to the monomer and, consequently, to the final material[63][64].

Similarly, instead of alkoxides, we can also use other organic groups such as carboxylates[65] or chelating groups[66] like Bdicarbonyl derivatives (acetylacetonates, acetoacetates, etc.) or polyols, amino derivatives[67], etc. or simply halides[68] (chloride, for example) or hydrides[69]. It is even possible to use several different groups within the same monomer, to play on their reactivities. Although these groups typically undergo elimination during the hydrolysis stage of the process, their significance remains paramount[66].

An important benefit of this method is that the precursors are often liquid or solid, which are typically soluble in conventional solvents, facilitating mixing. Nonetheless, caution must be exercised regarding the varying reactivity among monomers in such scenarios. As evident, the options are virtually limitless, and the selection of specific group(s) and monomers will be dictated by the intended end-use.

I.4 Colloidal silica

I.4.1 Definitions

A colloidal silica solution is made up of silica particles dispersed uniformly throughout a liquid, with the particle sizes ranging from 2 to 1000 nm. These suspended silica particles are commonly known as colloidal silica or silica colloid. A colloid is considered monodisperse if all its particles possess identical sizes. The stability of colloidal solutions is primarily defined by the fact that particles do not quickly clump together or settle. The visual characteristics of colloidal solutions change depending on the size of the particles. They are transparent to the in the visible range when the particle diameter is below 50 nm (assuming no significant absorption occurs), but become opaque when the particle diameter exceeds 100 nm, especially at higher concentrations. These differences in opacity are due to the scattering of visible light (spectral range: 400 to 800 nm) by the particles. When the size of the particles is smaller than about 1/10th of the wavelength (approximately less than 50 nm), they adhere to Rayleigh's theory. This theory explains that the intensity of scattered light changes significantly with particle size to the 6th power and inversely with wavelength to the 4th power. When particle size approaches the wavelength, they adhere to Mie's theory, which suggests that scattering is minimally influenced by wavelength, and that scattered light has a color similar to incident light (white in the case of daylight).

Nanoparticles are identified by the ISO TS/27687 standard as particles with a diameter of less than 100 nm[70]. Nevertheless, concerning colloidal silica, I'll broaden this concept to encompass submicron particles (with a diameter less than 1 μm). Specifically, colloidal silica exhibits consistent properties within this size range, except for heightened light scattering and accelerated sedimentation with increasing particle diameter.

I.4.2 Colloidal silica properties and applications

The desirable characteristics of colloidal silica have frequently positioned it as a preferred material, commonly utilized as an additive or carrier, in numerous commercial products, as exemplified in **Figure I.4.** These products find utility across diverse applications, including optics, catalysis, electronics, cosmetics, pharmaceuticals, reinforcement of composite materials, coatings, abrasives, the food industry, the textile industry, the paper industry, and more.

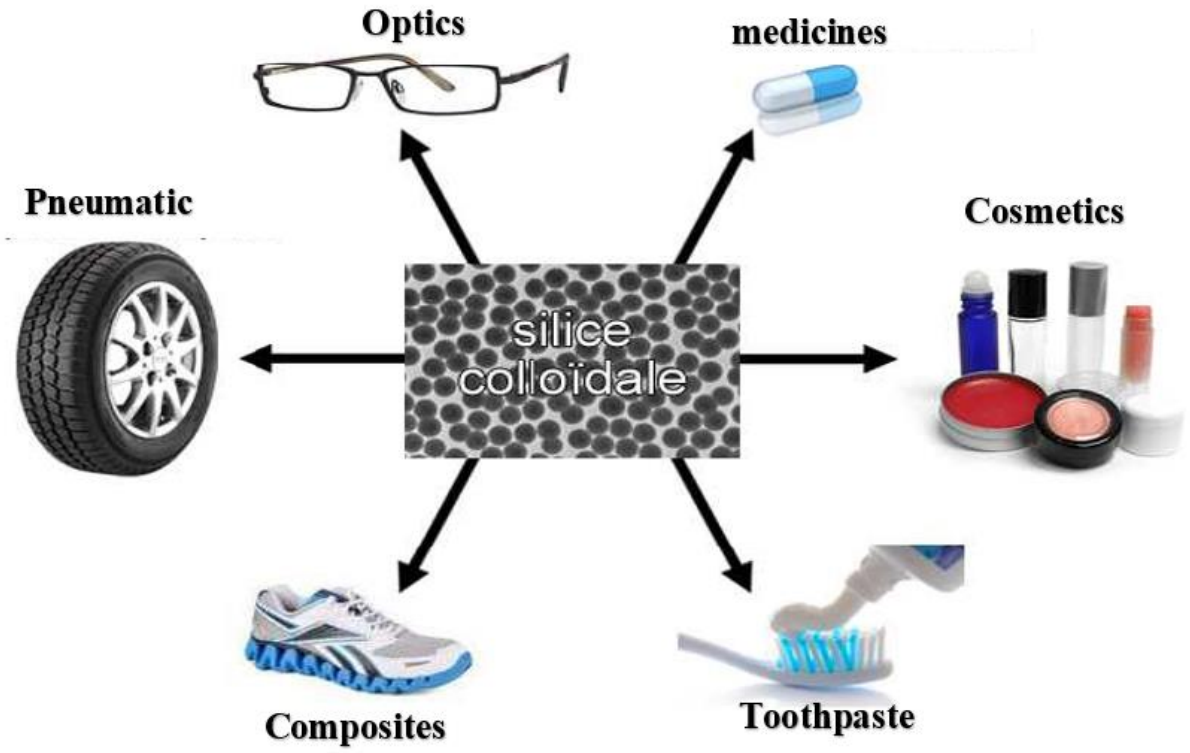

Figure I.4:illustrates how colloidal silica is incorporated into everyday products for various applications.

Silica is a cost-effective substance with well-established and understood synthesis methods. The widespread utilization of amorphous silica and colloidal silica can be attributed to several favorable properties, including:

- transparency from ultraviolet (UV) to infrared (IR),
- biocompatibility and non-toxicity,
- high physico-chemical stability,
- high colloidal stability in aqueous solution,
- a surface that can be easily functionalized,
- an oxygen diffusion barrier,
- a low refractive index.

The utilization of silica particles at the nanoscale has prompted their integration into numerous fields, and we will provide comprehensive examples thereof.

I.4.3 Construction materials

In the construction industry, the ability of silica nanoparticles (SiNPs) to enhance the mechanical strength of cement-based materials is highly desirable **(see Figure I.5).** Zapata and

colleagues[71] investigated the rheological and hardened characteristics of superplasticized cement mortar containing SiNPs. By adding appropriate amounts of superplasticizer, SiNPs were found to boost the compressive strength of the mortar. Similarly, Senff et al[72]. examined the impact of SiNPs on the rheological properties and strength of cement mortars. Their findings revealed noticeable differences in the rheological behavior of the mortars. Moreover, the addition of SNPs led to significant increases in torque, yield stress, and plastic viscosity of the mortars. Lin and colleagues[73] noted that incorporating silica nanoparticles (SiNPs) into sludge/fly ash mortars counteracted the adverse effects of sludge inclusion, particularly in terms of setting time and initial strength. The SiNPs exhibited accelerated formation of structures during rheological testing. The utilization of silica nanoparticles (SiNPs) was observed to enhance various properties of cement-based construction materials, including mechanical, engineering, and physiochemical aspects such as compressive strength, split tensile strength, flexural strength, and setting time.

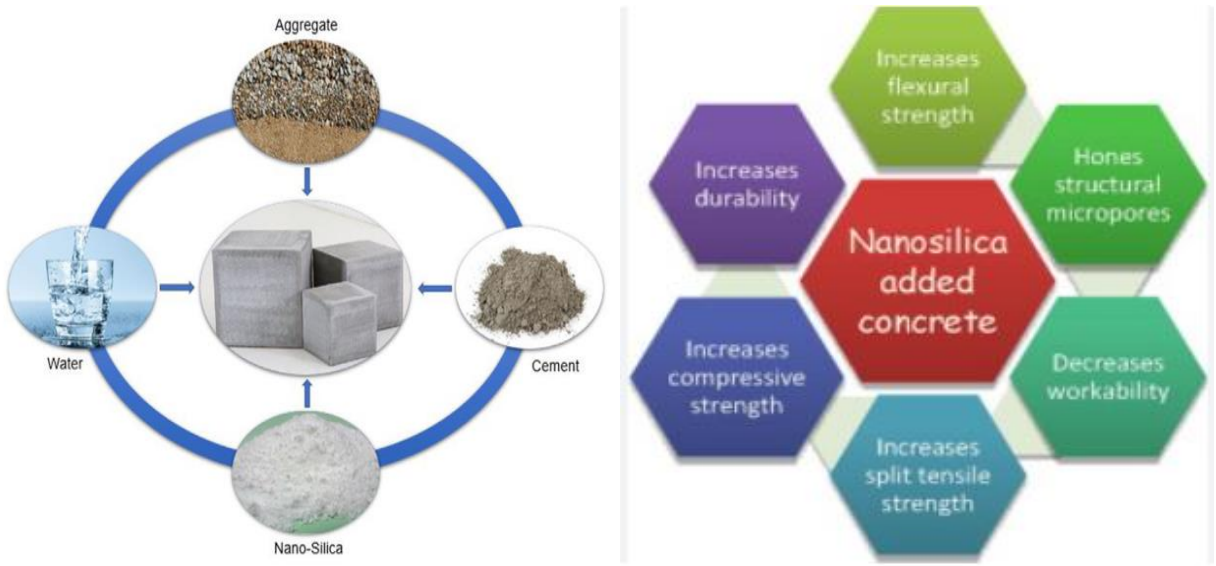

Figure I.5: Utilizing nano-silica in concrete exhibits advantageous enhancements, augmenting its overall performance and properties.[74]

I.4.4 Medication delivery systems

MSNPs offer significant advantages as a drug delivery system, primarily due to their capacity to enclose various drug molecules within their pore channels and their ability to regulate the release of drugs in a controlled manner. The particles incorporate drug molecules

through adsorption, a process by which they are absorbed onto the particle surfaces. Furthermore, SiNPs are engineered for a wide range of biomedical and biotechnological uses including but not limited to cancer therapy, DNA transfection, drug delivery, and enzyme immobilization[75][76].

MSNPs have been employed as drug delivery platforms for a diverse array of pharmaceutical compounds, varying in hydrophobicity/hydrophilicity properties, molecular weights, and biomedical effects. **(Figure I.6)**[76]

Munoz et al[77]. investigated the suitability of MSNPs as carriers for the hydrophobic drug Ibuprofen. According to their findings, the interaction between Ibuprofen molecules and SiNPs primarily stemmed from the bonding between the carboxylic acid group present in Ibuprofen and the silanol groups within the silica matrix. Lu et al[78]. explored the utilization of non-gated MSNPs for delivering hydrophobic anticancer medications, specifically camptothecin (CPT) and paclitaxel (Taxol), to human cancer cells. Their study revealed that these MSNPs successfully transported anticancer drugs into human xenografts implanted in mice, leading to the inhibition of tumor growth.

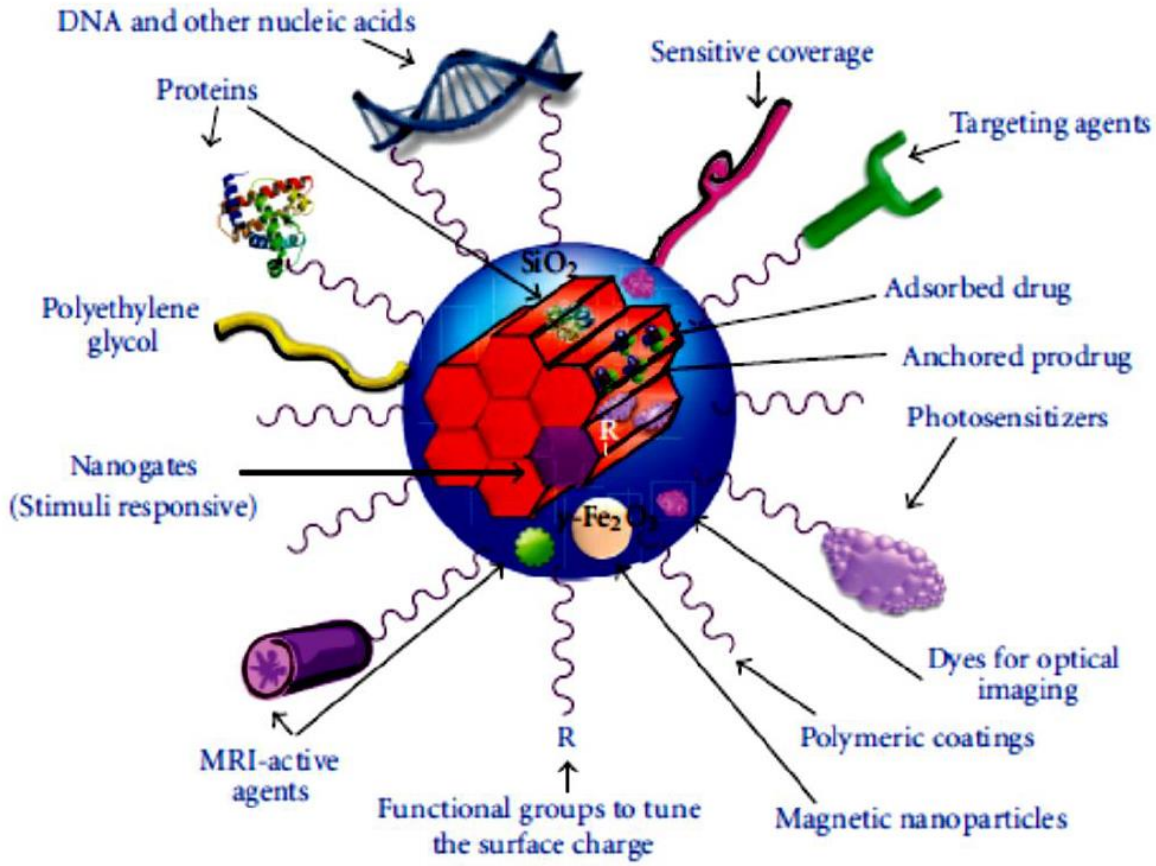

Figure I.6: Encapsulation Capability of MSNPs

I.4.5 Polymer-based nanocomposites

One of the notable uses of SiNPs lies in their incorporation into polymer nanocomposites. In this role, SiNPs function as fillers or reinforcements, enhancing the thermal, mechanical, physical, and chemical attributes of advanced composite materials. **Figure I.7**[79]. Kang et al[80]. noted that incorporating 400nm silica particles into epoxy resulted in a 13% enhancement in thermal properties. Meanwhile, Ragosta et al[81]. found that the epoxy groups interacted with the silanol groups on the silica surface, enhancing interfacial adhesion within the composite. This robust interfacial adhesion contributed to the heightened fracture toughness of the silica-epoxy nanocomposite.

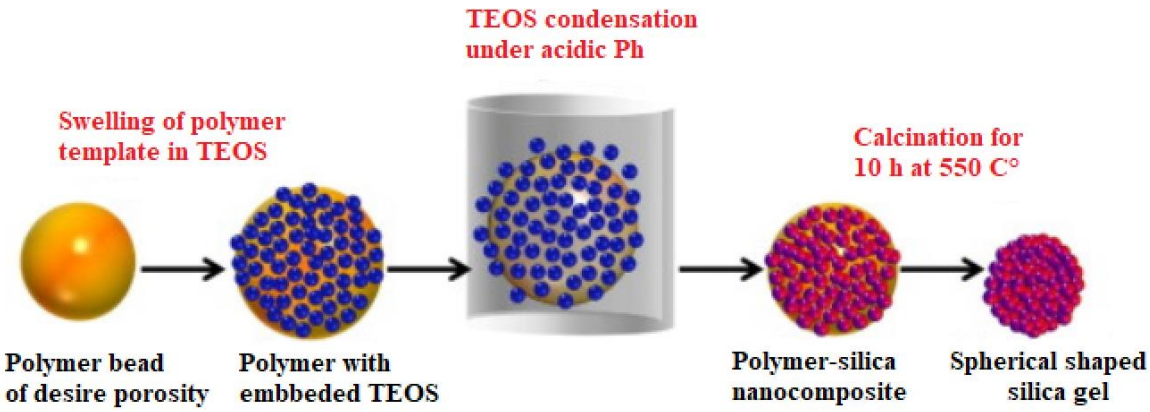

Figure I.7: The preparation of the nanostructured solid Polymer–silica composites

I.5 Preparation of the nanoparticles

I.5.1 The sol-gel process

The processes central to materials development encompass hydrolysis and condensation reactions. These reactions are initiated by introducing the precursors to water, occasionally in conjunction with a catalyst. These two stages are never perfectly separate; their progression can be regulated through pH adjustments in the medium.

In research, colloidal silica is typically produced using the sol-gel method. This process commences with the acid or base hydrolysis of an alkoxysilane like tetraethoxysilane (TEOS), followed by the subsequent basic condensation of the hydrolyzed silica monomers, resulting in the formation of silica particles.

Initially, the alkoxy groups undergo hydrolysis, either partially or completely depending on the conditions, resulting in the formation of -OH groups. Taking tetraethoxysilane (TEOS) as an example, complete hydrolysis leads to this outcome. **Figure I.8**:

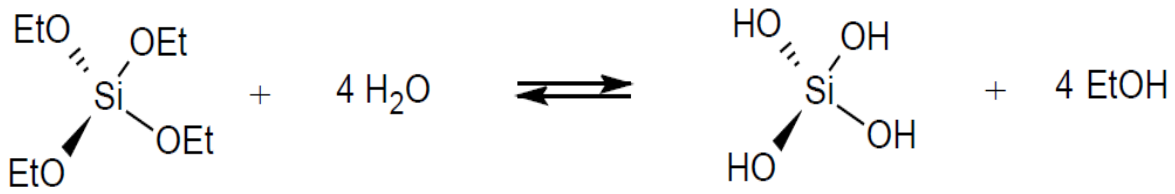

Figure I.8: Reaction diagram for the hydrolysis of tetraethoxysilane.

As ethanol is liberated, silanol groups are generated, which have the capability to undergo condensation reactions, exemplified by the oxolation reaction. **Figure I.9**

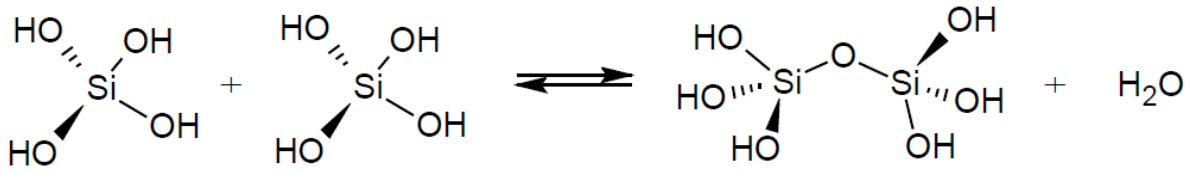

Figure I.9: Reaction diagram for the condensation of two silanol groups: oxolation reaction.

It's important to note that condensation can also occur through the interaction of an alkoxide with the hydrolyzed monomer, known as the alkoxolation reaction. **Figure I.10**

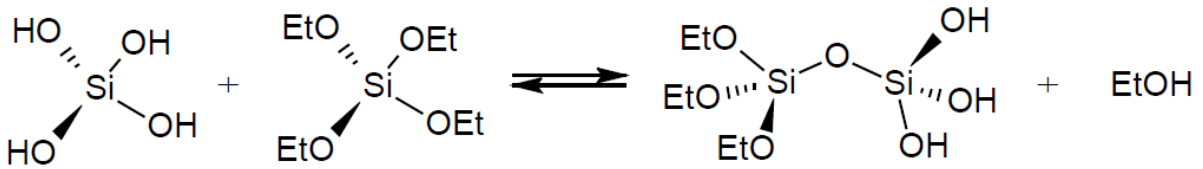

Figure I.10: Alkoxolation reaction diagram.

The advancement of condensation reactions leads to the creation of oligomeric clusters with varying degrees of branching, dispersed within the synthesis solvent, forming a sol. Subsequently, chromophores or nanoparticles can be introduced into this sol, imparting additional properties to the final material.

Afterward, the oligomers undergo intermolecular interactions with each other and branch out more and more, occupying an increasing volume fraction. As viscosity gradually escalates, the liquid undergoes a transition into a solid state, known as the sol-gel transition. Following this transition, the resulting gel is subjected to drying to yield the ultimate material, which could manifest as either a dense or porous monolith, a film if the sol has been coated onto a surface, or even as a powder. **Figure I.11**

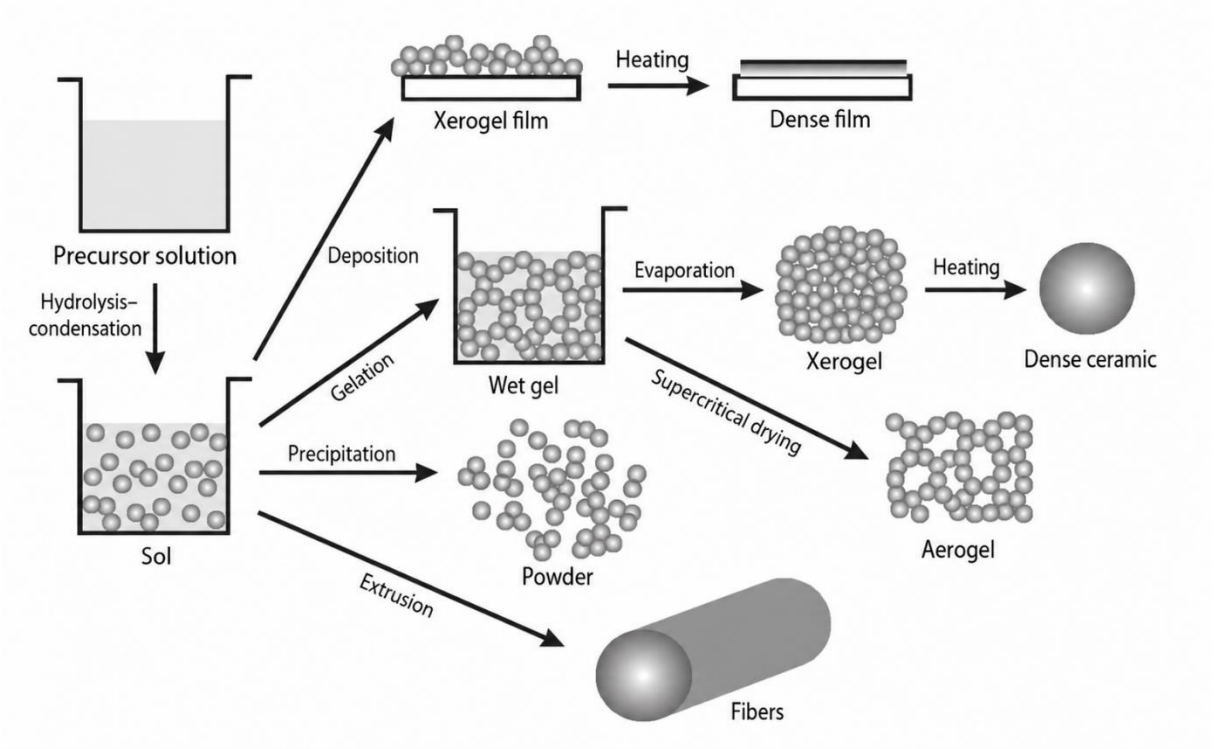

Figure I.11: Diagram of the different possibilities offered by the sol-gel process **[82].**

The texture of materials synthesized through this method is closely tied to the specific characteristics of the monomer employed, as well as the soil preparation and drying conditions. Various parameters such as pH, temperature, among others, can be adjusted to tailor the desired material properties. For instance, incorporating bases or acids can impact gelation kinetics, with bases hastening condensation kinetics and acids expediting hydrolysis kinetics. Additionally, the choice of specific solvents or surfactants can aid in regulating porosity[83][84].

In the sol-gel process, silicon offers the advantage of low reactivity, facilitating precise control over both hydrolysis and condensation stages. This is attributed to the stability of silicon alkoxides, a result of silicon's small ionic radius (0.26 nm), moderate electronegativity, and fully saturated coordination of 4. In contrast, transition metals like titanium form alkoxides with significantly higher reactivity[66], primarily due to their larger ionic radius (0.61 nm for titanium), lower electronegativity, and often unsaturated coordination (typically 6 for titanium). As a result, they can be used in a completely different way, for example by using chelating groups that satisfy their coordination requirements, and by working in a controlled atmosphere.

Hence, silicon stands as the most prevalent choice in materials, owing to its straightforward processing, cost-effectiveness, and the favorable optical characteristics exhibited by the resultant material, silica, particularly when utilizing tetraalkoxysilanes.

I.5.2 Impact of operating conditions

In the realm of controlling sol-gel reactions, the hydrolysis ratio (h), defined as the molar ratio between added water and precursor, is logically the most important factor in hydrolytic sol-gel processes. Consequently, the quantity of water and its method of introduction constitute pivotal elements in the reaction.

The concept is straightforward: when dealing with a highly reactive precursor, the abrupt introduction of significant water volumes will promptly yield unwanted precipitates. Conversely, insufficient water will fail to hydrolyze the entire precursor. This aspect is also influenced by the reactivity of the initial precursor.

Temperature also plays a significant role in controlling the kinetics of hydrolysis-condensation reactions, as higher temperatures accelerate these processes.

Nonetheless, there is another parameter of paramount importance, especially in silicon-based processes: the pH level of the reaction medium, which directly controls hydrolysis and condensation reactions.

I.5.3 Influence of pH on hydrolysis-condensation mechanisms[85][86][87]

Particularly concerning silicon, the significance of pH rivals, and sometimes even surpasses, that of the hydrolysis ratio, largely due to the relatively sluggish kinetics of hydrolysis-condensation reactions. The direct influence of pH on hydrolysis and condensation reactions is well-established, as demonstrated in the subsequent graph depicting TEOS. **Figure I.12**

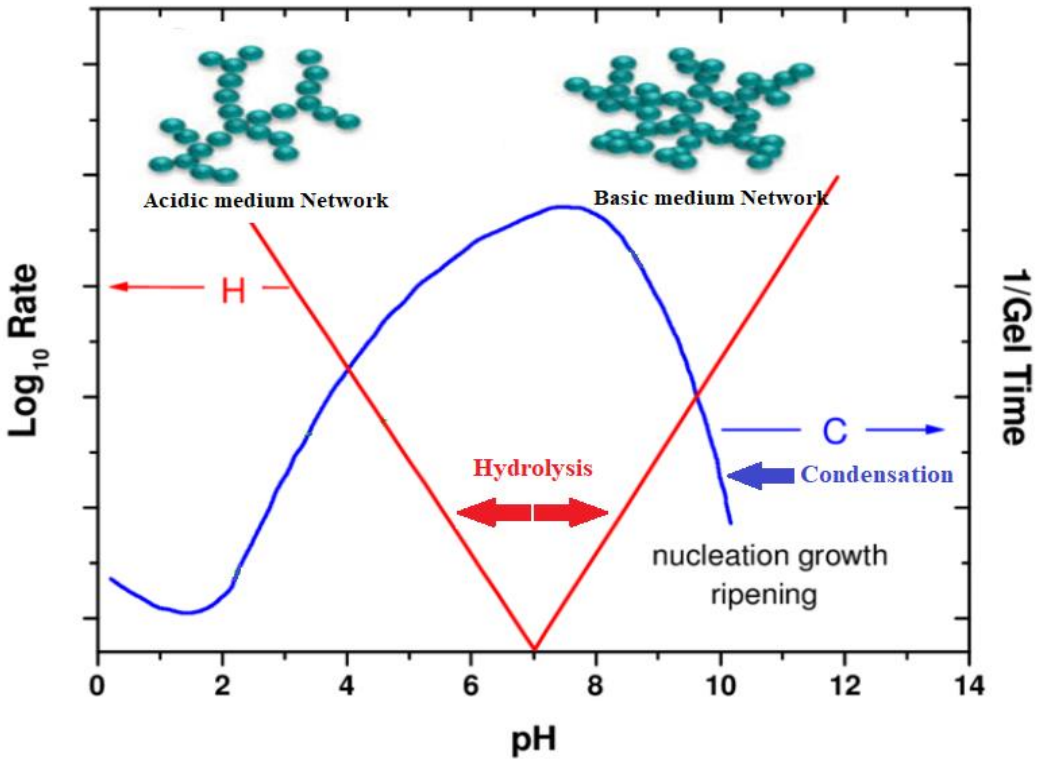

Figure I.12: The graph demonstrates the relationship between pH and the kinetics of TEOS hydrolysis and condensation, Condensation kinetics are estimated through the gelation time**[88].**

This shows the catalytic action of H+ or OH- ions on both reactions. From this simple graph we can deduce the broad outlines of the influence of pH on hydrolysis-condensation reactions.

At pH 7 (neutrality), representing the lowest concentration of H+ and OH-, hydrolysis kinetics are minimal. Consequently, both species seem to act as catalysts for the hydrolysis reaction. Condensation kinetics have a minimum around pH=2, which corresponds to the isoelectric point for silica[86]. We also see a drop in kinetics towards pH>8: in this pH range there is competition with silica redissolution[85], which corresponds to the cleavage of Si-O-Si bridges: depolymerization occurs. The mechanisms governing these reactions have been examined in

existing literature, revealing variations based on pH. Under neutral conditions (pH=7), hydrolysis advances through the following mechanism. **Figure I.13**

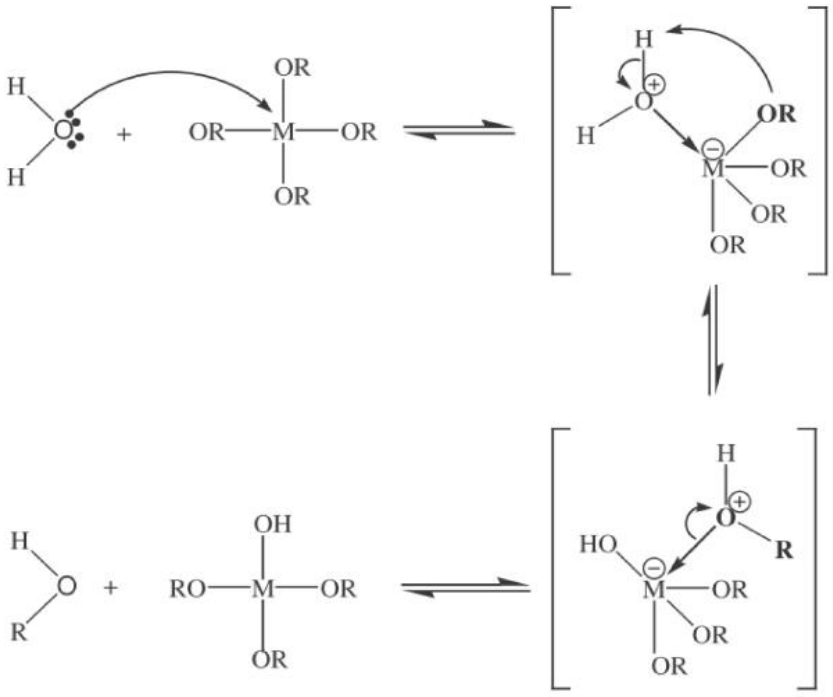

Figure I.13: Mechanism of hydrolysis in neutral media

The absence of a catalyst in the reaction occurs at a sluggish pace due to two primary factors. Firstly, water's efficacy as a nucleophile is limited, resulting in its reduced capability to initiate silicon attack. Secondly, the alkoxy group's inefficiency as a leaving group necessitates its protonation. However, under the prevailing pH conditions, this protonation process is constrained. Introducing H+ ions will thus facilitate the creation of a more effective leaving group by promptly protonating one of the alkoxy groups at the onset of the reaction. **Figure I.14**

Figure I.14: Protonation of the precursor in an acid medium.

The hydrolysis reaction is therefore greatly accelerated, as shown in **Figure I.15.**

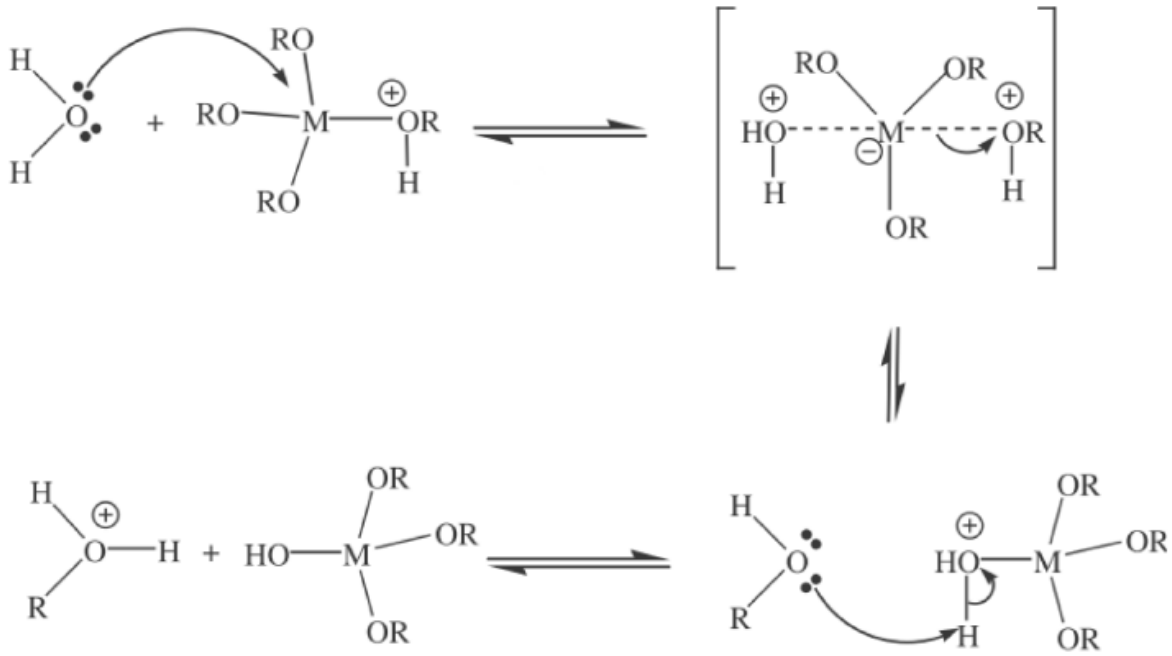

Figure I.15: Acid hydrolysis mechanism.

At the conclusion of the reaction, the alkoxonium species formed can transfer its proton to either an alkoxy or water molecule, thereby regenerating the catalyst. It's worth noting that as the number of hydrolyzed groups increases, the reactivity of the precursor diminishes. This decline stems from the inductive effects exerted by the -OH groups, which deplete the metal of electrons and impede the formation of the positively charged intermediate.

In an alkaline environment, the hydroxide ion supplants water as the nucleophile in the reaction, owing to its heightened reactivity. **Figure I.16**

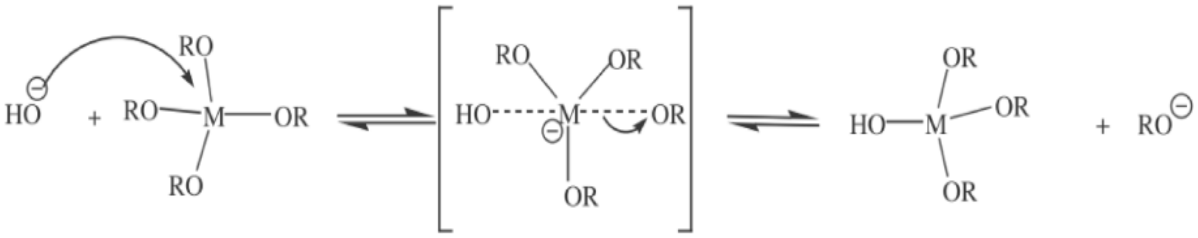

Figure I.16: Hydrolysis mechanism in a basic environment.

In this scenario, the reactivity of the precursor escalates with each hydrolysis step, attributed to the robust negative charge borne by the silicon in the reaction intermediate. This charge is stabilized, particularly in instances involving electron-withdrawing groups like hydroxy, and is further enhanced by steric effects facilitated by the diminutive size of -OH groups. Similarly, the alcoholate generated undergoes a reaction with water to rejuvenate the catalyst.

In the tetraalkoxysilane condensation process, it is observed that two distinct reactions occur. One of these reactions involves alkoxidation, where a non-hydrolyzed molecule reacts with another molecule that has undergone at least partial hydrolysis. **Figure I.17** Producing an alcohol molecule is the result of this reaction, which is thus more advantageous under conditions of low hydrolysis ratios, where in a significant portion of the alkoxy groups remains unhydrolyzed.

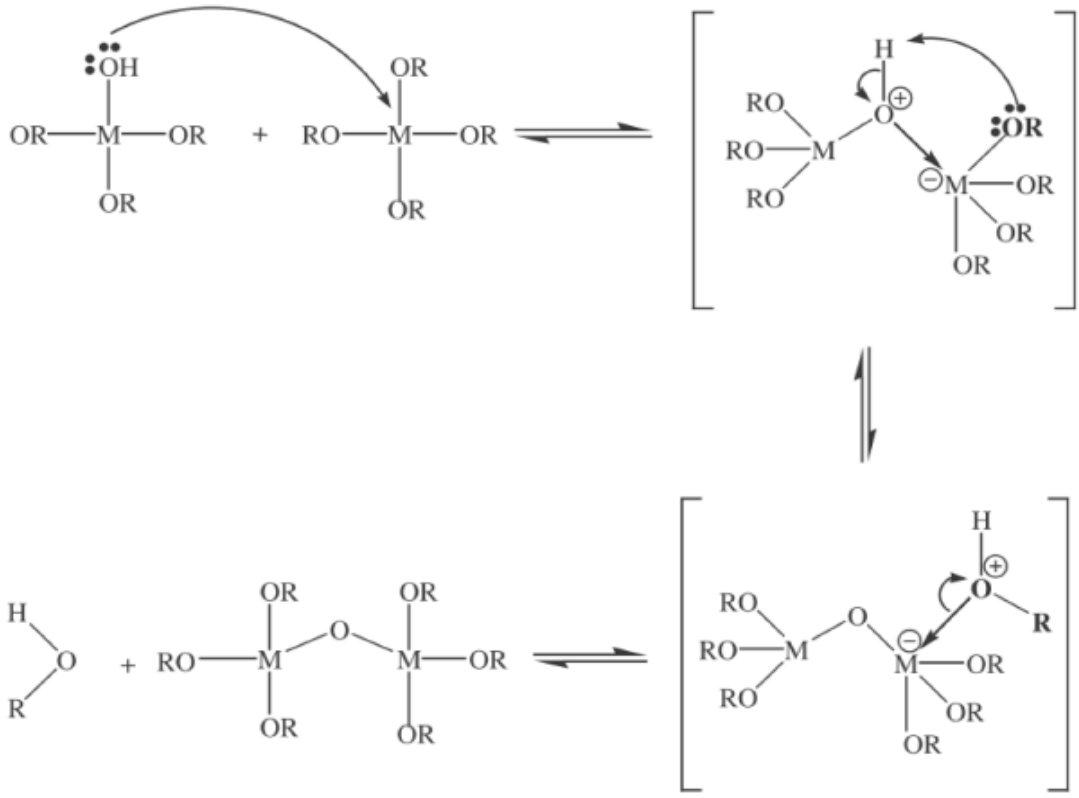

Figure I.17: Mechanism of the alkoxolation reaction.

And the alkoxolation.reaction, which takes place between two at least partially hydrolyzed molecules, ultimately generates a water molecule. **Figure I.18**

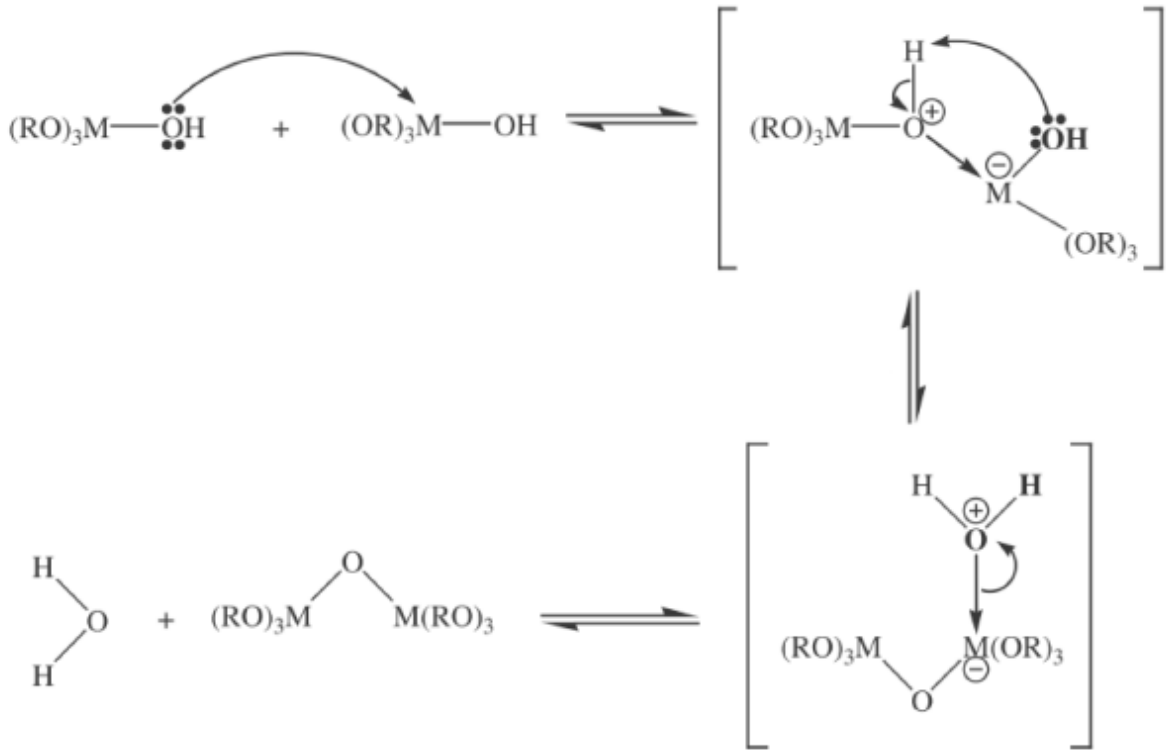

Figure I.18: Oxolation reaction mechanism.

The impact of pH on both reactions mirrors that of the hydrolysis step. This influence is exerted through the protonation of leaving groups under acidic conditions or the deprotonation of a hydroxy group, followed by the action of (OR)3SiO- formed as a nucleophile in a basic medium.

Considering these mechanisms and the observed kinetics **(Figure I.12),** it becomes evident that an acidic pH promotes the replacement of -OR groups by water, thereby facilitating hydrolysis, especially for pH values below 4. Consequently, hydrolysis reactions prevail over condensation reactions. Thus, under such conditions, the formation of species characterized by long, loosely-branched chains can be anticipated. On the contrary, a higher pH level promotes condensation reactions, especially within the pH range of 4 to 10, where the kinetics of condensation reactions significantly surpasses that of hydrolysis reactions. Consequently, one should anticipate the formation of compact particles under these conditions.

It's important to highlight that these reactions are balanced, and under extremely acidic conditions (pH < 2), reverse reactions can take place in the case of hydrolysis, resulting in re-esterification. This occurs as the hydroxy groups attached to silicon are protonated. Conversely,

in a basic environment (pH > 10), reverse reactions can occur for condensation, leading to the cleavage of Si-O-Si bridges and the formation of silanolates.

I.6 Synthesis of silica nanoparticles:

Stöber et al[7] were pioneers in employing the sol-gel technique for the synthesis of silica nanoparticles. Their research illustrated that when tetraethoxysilane (TEOS) dissolved in ethanol underwent hydrolysis and subsequent condensation in the presence of water and ammonia, it resulted in the creation of silica particles.

Two theoretical frameworks have been suggested to elucidate the process of nanoparticle formation, with both revolving around the nucleation and subsequent growth of silica grains.

The model proposed by Matosoukas and Gulari[89][90] mechanism, depicted in **Figure I.19.** It involves an initial nucleation phase triggered by the supersaturation of hydrolyzed TEOS monomers (Si(OH)4), followed by a subsequent growth stage facilitated by the deposition of hydrolyzed TEOS monomers onto the surface of existing particles.

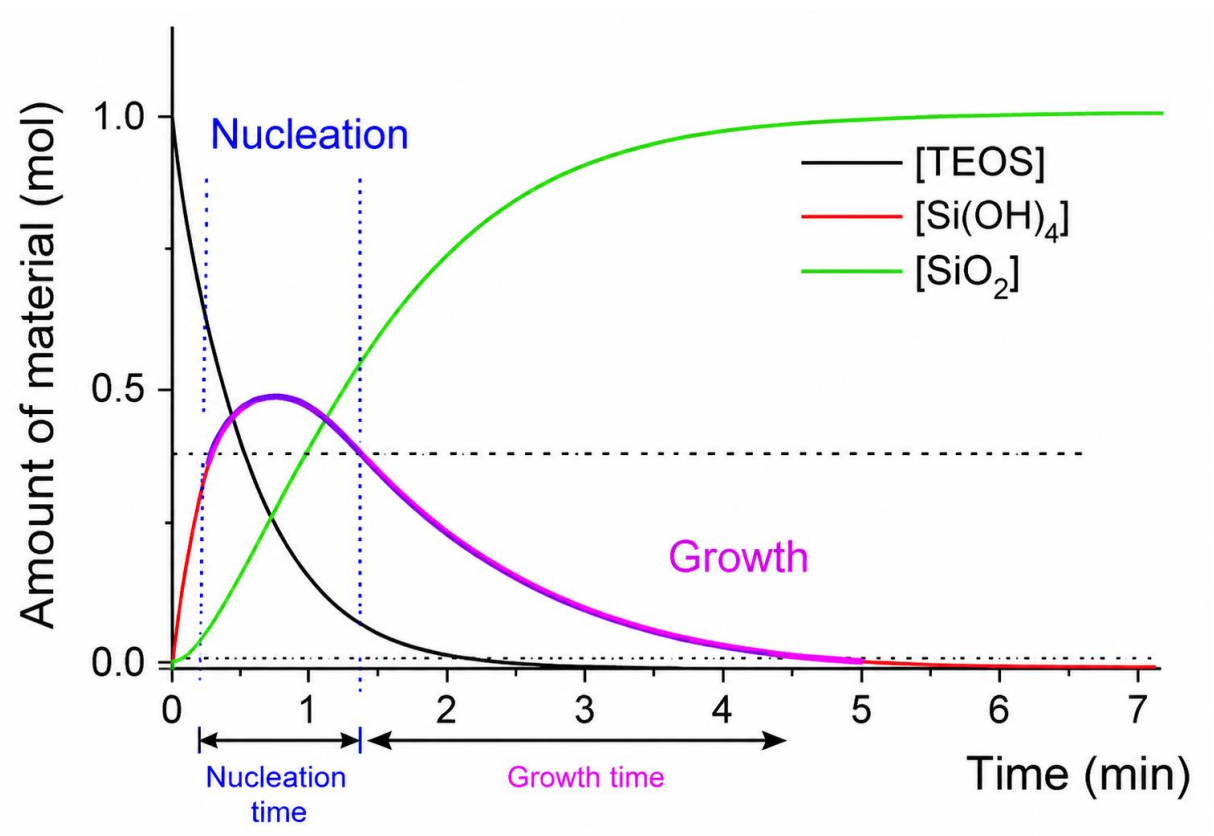

Figure I.19: Evolution of TEOS, Si(OH)4 and SiO2 concentrations as a function of time

I.6.1 Surfactant-assisted Synthesis of Silica Nanoparticles

I.6.1.1 Utilizing direct Systems

There is significant interest in investigating the potential of surfactants for fine-tuning the porous characteristics of silica nanoparticles (SiNPs). Nooney et al. employed both cationic and non-ionic surfactants as templates and demonstrated that by adjusting the TEOS–surfactant ratio under diluted conditions[91], they could synthesize mesoporous silica nanoparticles (MSNPs) with diameters ranging widely from 65 to 740 nm. They observed the formation of spherical MSNPs with uniform surfaces. Additionally, they put forward a mechanism detailing the generation of structured MSNPs employing CTAB as a template **Figure I.20**. Based on this mechanism, particle growth may proceed through one of the following potential pathways.

1. Continuous deposition of monomeric silica and surfactant ions onto pre-existing primary particles.
2. Ordered aggregation, characterized by the systematic clustering of primary particles.
3. Random aggregation, involving the irregular clustering of primary particles.

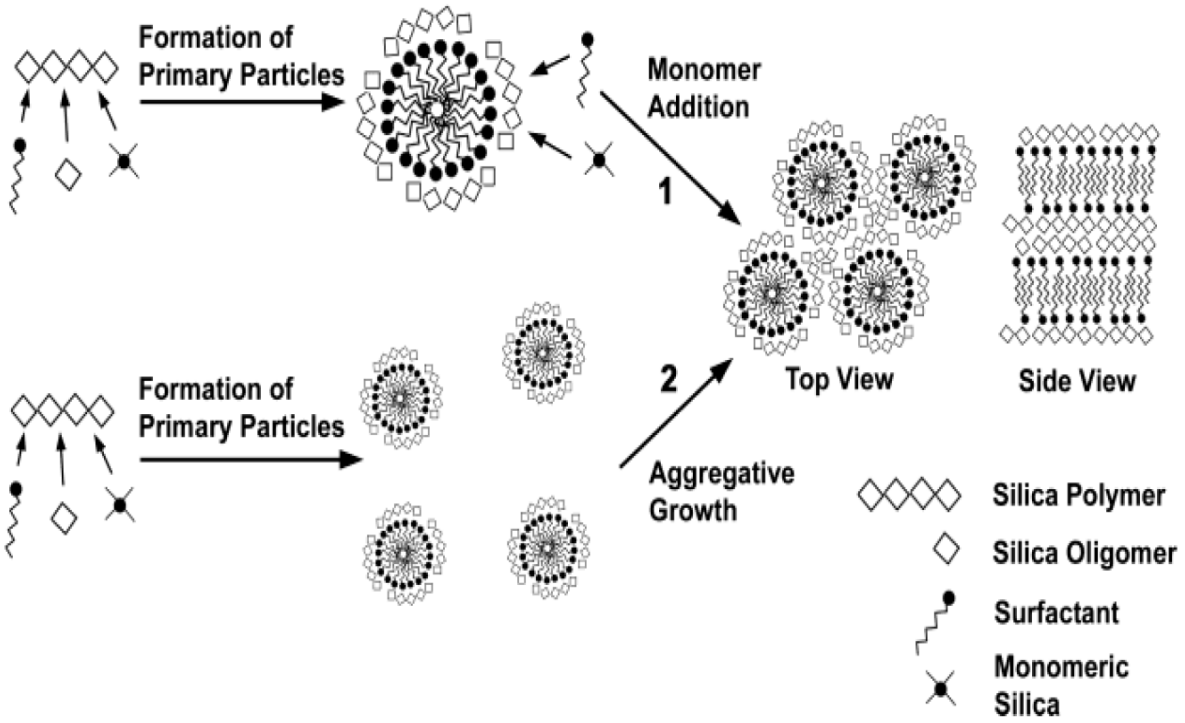

Figure I.20:mechanism detailing the generation of structured MSNPs employing CTAB as a template

Zhang et al[92]. synthesized a novel mesoporous silica sphere with a consistent diameter and mesopore canals resembling a starburst pattern, utilizing CTAB as a templating agent. They adjusted the arrangement of pore diameters within the sphere by modifying the concentration of ethanol. Ethanol was proposed to serve as a "spacing agent," allowing for the modulation of interactions between ethanol, the cationic surfactant, and the hydrophilic-hydrophobic equilibrium within the self-assembly system. The team suggested a "Liquid Crystal Initiated Templating" mechanism to explain the formation of the hexagonal array of micellar rods. In this mechanism, the process initiates with the regular hydrolysis of alkoxide, followed by the organization of surfactant molecules, and ultimately, the surfactant binds with silica oligomers. This mechanism is applicable for the synthesis of mesoporous silica MCM-41. Additionally, a mechanism for producing mesoporous silica featuring an egg-shell and starburst pore canal structure was suggested. According to this mechanism, initially, surfactant micelles and micellar rods were formed in an extremely diluted aqueous solution. Subsequently, these rods underwent self-assembly into a lamellar phase. Furthermore, it was noted that a mixed lamellar-hexagonal membrane, with water layers separating them within the surfactant silicate system, was generated. **Figure I.21**

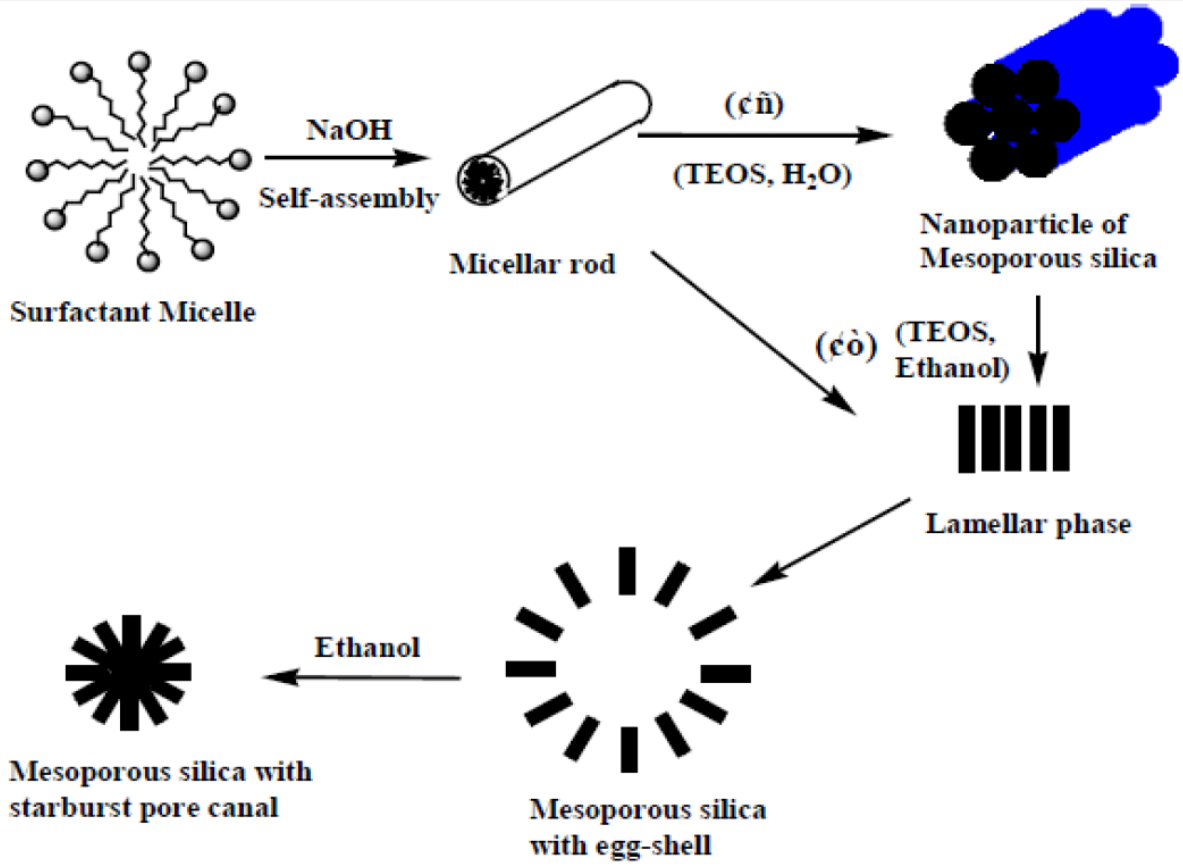

Figure I.21:mechanism explain the formation of the hexagonal array of micellar rods.

I.6.1.2 Utilizing Microemulsion Systems

Initially, emulsions and microemulsions garnered attention primarily within industrial sectors such as petrochemicals, textile impregnation and finishing, pharmaceuticals, cosmetics, and paints, as outlined in the review authored by Schwuger et al[93]. The method of preparing silica nanoparticles through micellar formation was first elucidated in the 1990s by Osseoasare and Arrigada[94]. They conducted the hydrolysis-condensation reaction of tetraethyl orthosilicate (TEOS) within an inverse micellar system, utilizing ammonia as a catalyst.This technique has demonstrated significant appeal for generating nanoparticles with precise size and morphology control, owing to its capacity to manipulate two distinct sets of parameters: the composition of the microemulsion and the amounts of reagents employed. Furthermore, studies have indicated that this synthesis approach achieves both small particle size and uniformity, in contrast to the traditional Stöber method[94][95].

I.6.1.2.1 The water-in-oil microemulsion field

In the realm of water-in-oil microemulsions, a uniform distribution of water nanodroplets is suspended within a continuous oil phase. These nano-droplets of water are held stable at the oil interface through the action of surfactant molecules, which organize into reverse micelles. While water/oil/surfactant ratios are undeniably pivotal for the formation and endurance of microemulsions, they also play a crucial role in determining the dimensions and configuration of the reverse micelles[96].

I.6.1.2.2 Properties of reverse micelles

The prevailing consensus in numerous studies indicates that spherical reverse micelles comprise nano-scale water droplets encased within a monolayer of surfactants, depicted schematically in **Figure I.22.**

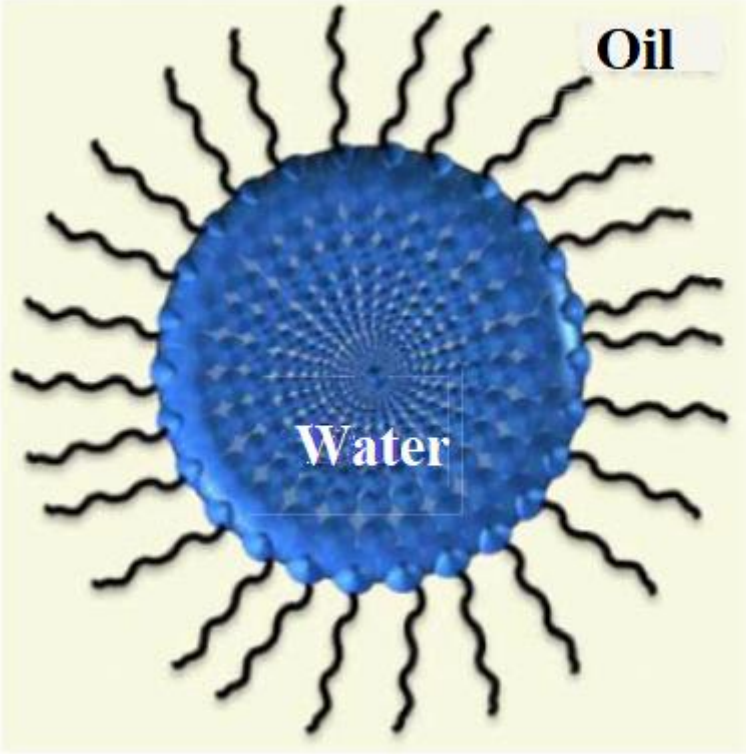

Figure I.22: The structural cross-section of a spherical reverse micelle.

The surfactant film functions as a barrier, effectively separating the water nanodroplets and inhibiting their eventual merging. Consequently, within the reverse micellar phase, the water nanodroplets remain distinct, with their size primarily dependent on the quantity of solubilized

water and can be finely regulated by adjusting the W ratio, which represents the molar concentration ratio of water to surfactant[97]. **Equation I-2**

$$W = \frac{[H_2O]}{Surfactant} \quad \textbf{Equation I-2}$$

Inverse micelles undergo Brownian motion as well. This motion causes collisions where the interfaces can briefly merge to create temporary structures lasting microseconds. This facilitates the exchange of contents between nanodroplets without traversing the continuous oil phase[98]. However, when the particles reach a certain size, content exchange is hampered because it would require a large change in the curvature of the surfactant film surrounding the reverse micelles, which is not energetically favorable. Surfactant molecules adhere to the surfaces of particles, providing stabilization and shielding them from additional growth[99]. As a result, nanoparticles obtained in such a medium are generally quite distinct and characterized by a narrow size distribution.

I.6.2 Exploring the Reverse Micelle: An Enclosed Environment for Chemical Reactions

The reverse micelles comprising the water-in-oil microemulsion serve as nanoreactors facilitating nanoparticle synthesis. The constrained environment of these nanoreactors presents a significant benefit for achieving controlled size and architecture in nanoparticle synthesis. There are two main approaches to nanoparticle synthesis nanoparticles by microemulsion. The initial method entails the preparation of two distinct microemulsions, each containing varied reagents solubilized within their respective micelles, followed by the combination of these two microemulsions. In the second method, nanoparticles are produced within a singular microemulsion. The reagents are incrementally introduced into the microemulsion and subsequently migrate into the micelles due to their affinity with water.

I.6.2.1 Choice of microemulsion components

Managing nanoparticle synthesis via microemulsion inherently requires regulating the parameters governing the microemulsion. The selection of these components holds utmost significance, as they directly influence the interfacial fluidity within the microemulsion,

namely, the elasticity of the surfactant film[100]. This factor directly impacts intermicellar exchange, thereby influencing the size of the synthesized nanoparticles.

I.6.2.2 Surface active agent

Many investigations have documented how the properties of microemulsions are affected by the surfactant, which varies based on factors such as the length or quantity of alkyl chains, the size of the polar head, or its ionic nature[101][102]. It is widely acknowledged that the selection of surfactant directly influences the shape, size, and elasticity of micelles, thereby impacting the size of nanoparticles synthesized within them. A wide array of surfactants is presently accessible in the market. Both ionic and nonionic surfactants are viable options for regulating film elasticity. Some of the frequently employed surfactants include sodium dioctyl sulfosuccinate (AOT), the Triton X series, the Brij® series, Igepal CO-520, cetyl trimethyl ammonium bromide (CTAB), sodium dodecyl sulfate (SDS), and various others. Moreover, there's often a requirement to incorporate a co-surfactant to enhance interfacial fluidity. Although this co-surfactant may be selected from those mentioned earlier, long-chain alcohols like hexanol are also commonly employed for this purpose.

I.6.2.3 The oil phase

The nature of the oil phase, or solvent, can additionally impact the size of the produced nanoparticles. However, its effect is secondary compared to the surfactant and becomes noticeable only with significant variations in chain length. Hence, the primary factors determining its suitability will be its compatibility with the selected surfactant and its toxicity level. Typically, the oil phase consists of cyclohexane or heptane. Occasionally, toluene, chloroform, Hexane, or octane may also be utilized.

I.6.2.4 The aqueous phase

The characteristics of the aqueous phase can exhibit significant diversity. Frequently, it serves as the medium wherein the precursors for in situ nanoparticle synthesis are dissolved. Additionally, it may function as a colloidal entity, indicating that micelles encapsulate pre-synthesized nanoparticles. Selection of the aqueous phase (including factors like pH, composition, etc.) is determined by the solubility or stability requirements of these components.

I.6.3 Microemulsion silica synthesis

The process adheres to the traditional sol-gel mechanism, which entails the hydrolysis of a silica precursor followed by the condensation of the resulting silica monomers. Within water-in-oil microemulsions, nanoparticle generation occurs within the reverse micelles themselves, as depicted in **Figure 1.23**[103].

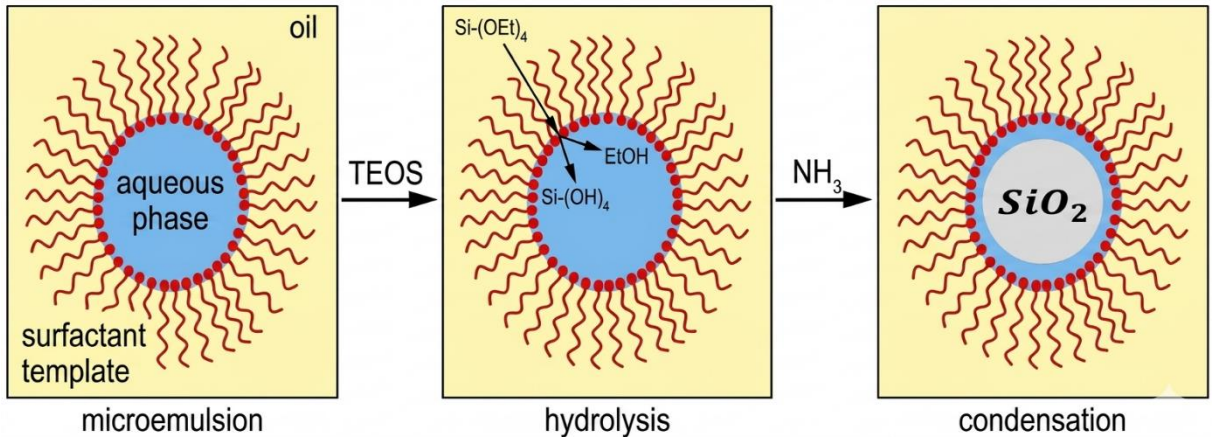

Figure I.23: Visualization of the synthesis of silica nanoparticles using water-in-oil microemulsion.

The silica precursor, initially dissolved in the oil phase, undergoes hydrolysis upon contact with aqueous micelles through diffusion. Subsequently, the hydrolyzed silica monomers migrate into the aqueous phase, where they undergo condensation to produce nanoparticles. The hydrolysis step can be carried out either by acid or base catalysis. On the contrary, the condensation process necessitates catalysis, which must be basic to yield spherical nanoparticles. Thus, this stage involves the introduction of a base, typically ammonia, although alternatives such as sodium hydroxide (NaOH) can yield comparable outcomes. Following a reaction duration spanning from several hours to a few days, the microemulsion is typically destabilized by the addition of a substantial volume of alcohol or acetone. Subsequently, the nanoparticles are retrieved and subjected to washing through centrifugation cycles.

II. Chapter 02: Methods and Materials Employed in Silica Nanoparticle Synthesis

II.1 Introduction

In the first chapter, it was demonstrated that micellar systems provide an effective reaction medium for constructing a silica matrix with precise control over its size and morphology. In this subsequent chapter, we will employ this approach to acquire hybrid nanomaterials that integrate diverse compositions (organic/inorganic) and structures (oxide/metallic). While the microemulsion pathway has been predominantly utilized in this study for synthesizing cluster@SiO2 nanoparticles, we have also explored the Stöber method. Our objective was to produce cluster@SiO2 nanoparticles ranging in diameter from 100 to 700 nm, suitable for our specific applications. These fabrication processes allowed us to assess the merits and drawbacks of both synthesis techniques while confirming their synergistic capabilities.

II.2 Synthesis of Silica Nanoparticles

II.2.1 Chemicals and Reagents

Cationic surfactant Cetyltrimethylammonium bromide CAS:57-09-0 (CTAB, Sigma, Bio Ultra for molecular biology, > 99%)

Nonionic surfactants TX100 (99%) CAS:9002-93-1

Procaine hydrochloride ≥ 97% CAS:51-05-8 were purchased from Sigma-Aldrich

Tetraethyl orthosilicate (TEOS, Aldrich, ≥ 99%) CAS:78-10-4

Sodium hydroxide (naoh, Eka pellets ≥ 98%) CAS:1310-73-2

Ammonium hydroxide 30% solution CAS:1336-21-6

N-Hexane anhydrous, 95% CAS:110-54-3

Butan-1-ol for molecular biology, ≥ 99.5% CAS:71-36-3 Sigma Aldrich,

Absolute ethanol ≥ 99.8%) CAS:64-17-5 was purchased from Honeywell

Deionized water (D.I water) from a Millipore system Milli-Q 18 MX cm was used in all synthesis steps

II.3 Preparation of monodispersed silica nanoparticles (SiNPs)

- **in aqueous medium**

Synthesis of monodisperse SiNPs was carried out according to the method proposed by T. Ribeiro et al[8]. With little modifications. Briefly, a known amount of the surfactant (CTAB or TX-100) was dissolved in water (22 mL) at 25 °C under vigorous stirring. After 35 min, 1.75 mL of sodium hydroxide solution with a concentration of 2M, followed by a dropwise addition of 2.5 mL of TEOS within 5 min. Immediately, the reaction temperature was raised up to 40 C° and left under vigorous stirring for 2 h. After cooling, the obtained dispersion was centrifuged at 12000xg for 30 minutes and washed three times with a 1:1 water/ethanol mixture and one time with absolute ethanol. Afterward, the supernatant was removed and the precipitated gel phase was further dried at 60°C in a ventilated oven for 24 hours. The obtained powder was calcined at 500°C for 2 hours to retrieve pure SiNPs. The same experiment parameters were conducted at a low concentration of NaOH 0.2M.

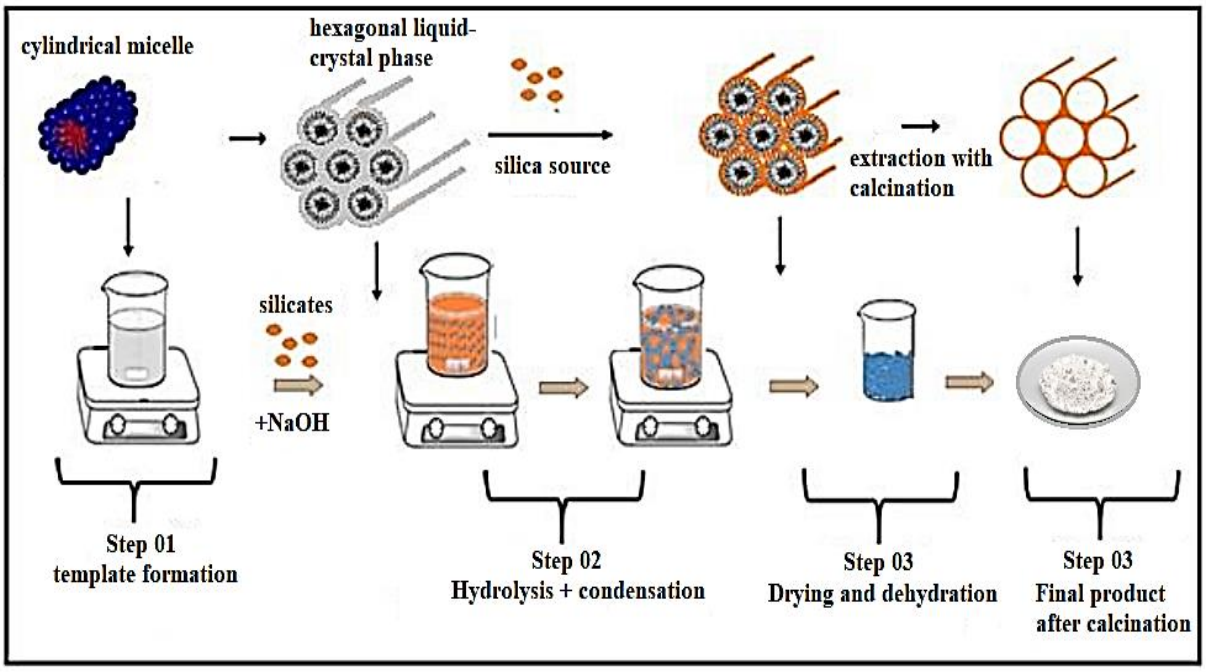

Figure II.1: General diagram showing the synthesis of silica-based mesoporous nanoparticles

II.3.1 SiNPs from Ionic surfactant CTAB:

Large Solide Silica spheres (LSiNPs) were prepared by firstly mixing (0.09 g) of cationic surfactant CTAB with deionized water (1.7 ml) at ambient temperature. After 10 minutes under vigorous stirring, (2 ml) of Butan-1-ol and (8 ml) of n-Hexane were added to the aforementioned aqueous solution. Secondly, after 10 minutes under stirring (800 rpm), a dropwise addition of (0.3mL) TEOS is carried out followed by (0.06ml) of ammonia and the whole mixture is left 24h under stirring. An equivalent volume of ethanol is then added to the mixture to break the formed emulsion. The large LSiNPs were isolated by centrifuging the obtained solution at 14000 rpm for 30 min. The product obtained was further washed several times successively with ethanol and D.I. water to remove the unreacted chemicals. The final product was retrieved after a drying process at 60°C during 24 hours.

II.3.2 SiNPs from Nonionic surfactant TX-100:

For TX-100, 0.25 M of the nonionic surfactant was mixed directly with (2 ml) of Butan-1-ol and (8 ml) of n-Hexane at ambient temperature. The same protocol applied to CTAB preparation from the second step was adopted until the final stage and the purification of the nanoparticles by drying.

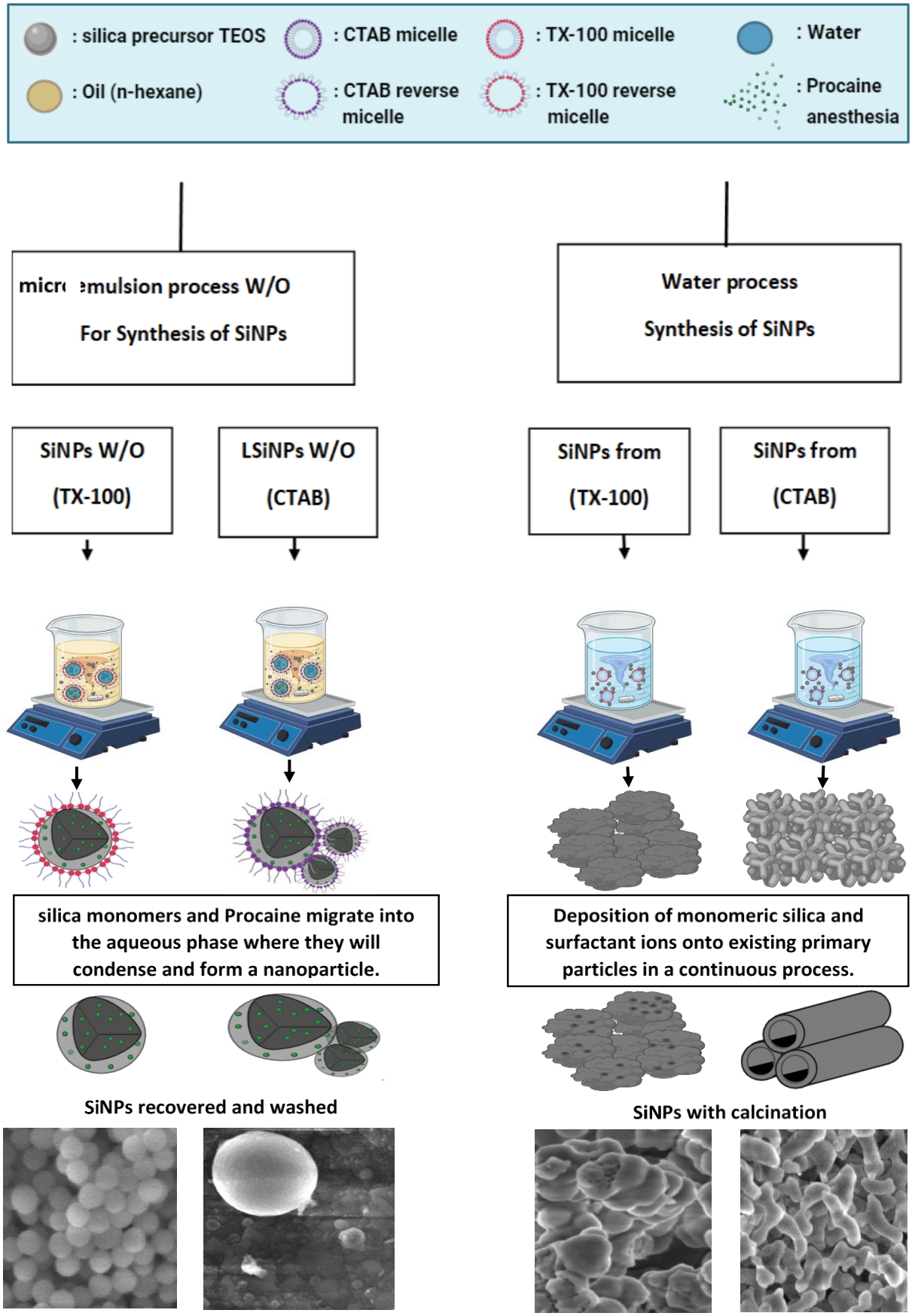

Figure II.2: Schematic illustration of the formation of SiNPs particle structures.

II.4 Characterization Techniques

II.4.1 The theoretical foundation of dynamic light scattering

Dynamic light scattering (DLS), alternatively referred to as photon correlation spectroscopy (PCS), is a technique for assessing variations in light intensity over time. Thanks to its precision, speed, and consistent reproducibility, DLS has emerged as a widely adopted approach in nanotechnology. With advancements in instrument design and data analysis methodologies, contemporary DLS equipment not only enables particle size determination but also facilitates measurements of zeta potential and the molecular weight of macromolecules.

The fundamental principles underlying DLS are as follows: Particles in suspension undergo Brownian motion, causing fluctuations in light intensity. These particles exhibit random movement within the liquid medium, with the velocity of Brownian motion contingent upon both particle size and the viscosity of the surrounding medium (such as water or organic solvents). Studies have shown that smaller particles in less viscous mediums experience faster Brownian motion. As light traverses through the colloidal solution, it interacts with the particles, resulting in light scattering that can be detected at specific angles. The detected signal represents the combination of numerous scattered photons, holding statistical significance. Instantaneous light intensity varies around a mean value, with fluctuation amplitude correlating with particle size. At any given moment, the light intensity is considered comparable to that at another moment within a very brief timeframe[104]. As previously mentioned, particle velocity during Brownian motion follows the Stokes-Einstein equation and is directly related to particle size.

$$D = \frac{K_B T}{6\pi\eta R_H}$$ **Equation 1:** The Stokes-Einstein equation

D Translational diffusion coefficient [m²/s] – “speed of the particles”

K_B Boltzmann constant [m²kg/Ks²]

T Temperature [K]

η Viscosity [Pa.s]

R_H Hydrodynamic radius [m]

- ## The basic DLS setup

Figure II.3 illustrates the essential configuration of a DLS apparatus. Here, a monochromatic laser is directed towards the sample confined within a cuvette. Should particles be present in the sample, the incident laser beam undergoes scattering in various directions. Subsequently, the scattered light is captured at a specific angle over time, and this signal is employed to ascertain the diffusion coefficient and particle size through application of the Stokes-Einstein equation.

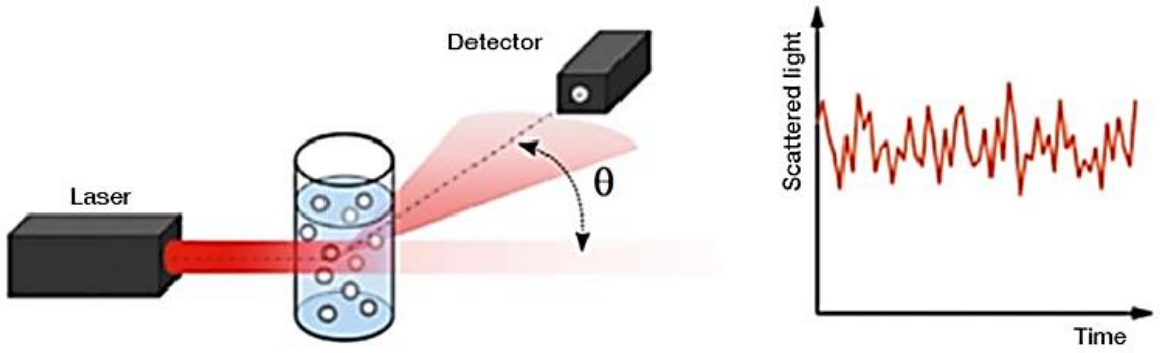

Figure II.3: illustrates the core configuration of a DLS measurement setup. the sample is enclosed within a cuvette, and the scattered light emitted by the incident laser is detectable across various angles **[105].**

Typically, a gray filter is interposed between the laser and the cuvette to attenuate the incident laser light. These filter settings can be automatically regulated by the instrument or manually adjusted by the user. In instances where turbid samples are analyzed, the detector may become overwhelmed by the influx of photons. Consequently, the laser light is attenuated to ensure the detector receives a signal that is both adequate and manageable for processing.

- **Measurement**

When analyzing large particles, the scattered spot's intensity fluctuates slowly owing to their sluggish motion. Conversely, for small particles, the density of scattered spots fluctuates rapidly due to their swift movement. The relationship between large and small particles can be mathematically expressed. Notably, the correlation function's decay rate is indicative of particle size, with small particles exhibiting significantly faster decay rates compared to large particles. Ultimately, particle size and distribution are determined by examining variations in light intensity and the correlation function thereof.

As mentioned earlier, the measurement of particle size in the sample relies on particle movement rather than direct measurement. The term "hydrodynamic diameter" denotes the size of smooth, spherical particles that diffuse at a rate equivalent to the particles within the sample. It is important to consider this distinction when comparing DLS measurement results with those obtained from other techniques, as they may pertain to different physical parameters of the sample.

In data analysis stemming from experiments, the distribution coefficient (or particle dispersion index, PDI) is a crucial parameter. It serves as an indication of the uniformity in particle size and plays a significant role in characterizing particle dimensions. When PDI falls below 0.05, systems are deemed monodispersed, as is often the case with certain emulsions adhering to specific standards. If PDI registers below 0.08, the system is considered near monodispersed, albeit limited to analysis via a single exponential decay method in DLS, which may restrict resolution capabilities. A PDI value ranging from 0.08 to 0.7 signifies a moderately dispersed system, offering optimal suitability for algorithmic applications. Conversely, a PDI exceeding 0.7 indicates a system with a broad size distribution, rendering it less compatible with the light scattering analysis method[104].

II.4.2 Electron Microscopy

Ruska and Knoll introduced electron microscopes (EMs) in 1931, marking the beginning of a continuous evolution that transformed these instruments into remarkably versatile tools[106][107]. Electron microscopy encompasses two primary techniques: scanning electron microscopy (SEM) and transmission electron microscopy (TEM). Despite both methods capable of detecting various signals arising from interactions between electrons and matter, they are conventionally treated as distinct disciplines due to differences in instrument design, sample preparation requirements, and the type of information they provide. Scanning electron microscopes (SEMs) are typically more user-friendly, making them readily available to novice electron microscopists seeking a tool for microstructure analysis. In standard imaging mode, SEMs only examine the surface, allowing for the observation of samples of diverse shapes and sizes without requiring extensive preparation time. Numerous contemporary SEMs enable the observation of samples at low voltages, facilitating the analysis of beam-sensitive materials in a non-destructive manner. Recent technological progress, especially in low-voltage SEM, has significantly enhanced its appeal for investigating materials that were previously challenging to image at high resolutions[108][109].

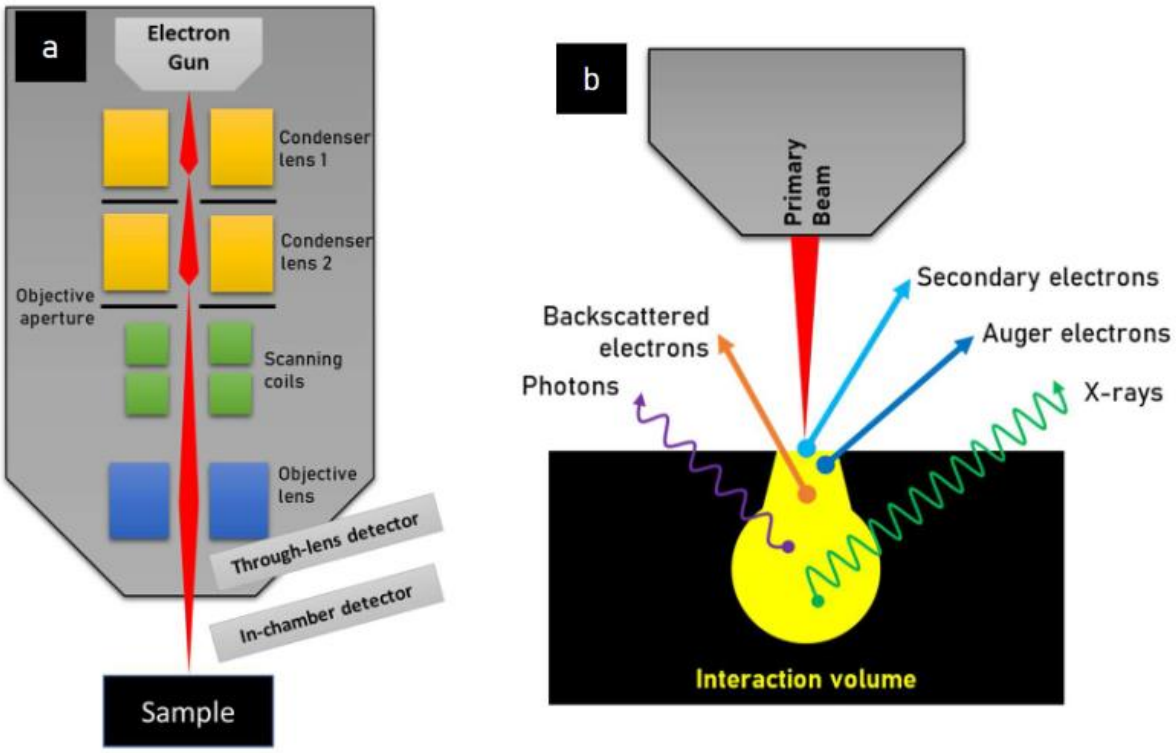

Figure II.4: a) A schematic representation illustrating the configuration of a scanning electron microscope column and the positioning of secondary electron detectors. b) The signals produced when a sample is exposed to an electron beam in the scanning electron microscope

- **Basics**:

Electron microscopy operates on the fundamental principle of electron-sample interactions, where an electron beam interacts with the sample. The interactions between electrons and matter are intricate, leading to various events occurring within the interaction volume when electrons hit the sample. These diverse events generate different signals, as depicted in a schematic summary in Figure II.4. Numerous detection systems exist to capture the emerging signals, enabling a wide range of experiments to be conducted in electron microscopy (EM). Because various signals stem from a series of interactions within the interaction volume, the spatial resolution of an emitted signal hinges not only on the electron beam's probe size but significantly on the interaction volume's dimensions. Typically, X-ray and backscattered electron (BSE) signals are more pronounced at higher accelerating voltages but come at the expense of reduced spatial resolution. Conversely, the secondary electron signal becomes stronger and more precisely localized as accelerating voltages decrease, rendering it the preferred signal for low-voltage scanning electron microscopy (LV-SEM) experiments. In the

context of the upcoming discourse, LV-SEM will be delineated as encompassing primary beam energies ranging from 300 eV to 5 keV, with a project-specific maximum of 2 keV.

II.4.3 X-ray diffraction

X-ray diffraction stands as a potent method for examining crystalline solids. First observed in 1895 by the German physicist Wilhelm Röntgen, X-rays serve as the foundation for a variety of analytical techniques, including radiography, spectroscopy, and diffractometry. These electromagnetic radiations fall within a spectral range characterized by wavelengths in the angstrom (Å) scale. In 1912, Max von Laue demonstrated that the similarity between X-ray wavelengths and assumed interatomic distances mimics the function of light in optical gratings, giving rise to a diffraction phenomenon governed by the same principles as interference. Essentially, a crystal represents an arrangement of atoms, ions, or molecules exhibiting a regularly repeating pattern in all three spatial dimensions. Since interatomic distances are typically of the order of an angstrom, comparable to X-ray wavelengths, a crystal forms a three-dimensional lattice capable of diffracting X-rays. Consequently, in 1913, William Henry and William Lawrence Bragg (father and son) successfully determined the crystal structure of sodium chloride, paving the way for the elucidation of numerous other metal salt structures.

- **Basics:**

X-ray diffraction entails exposing a clay sample, whether oriented or non-oriented, to X-ray radiation with wavelengths ranging from 0.1 to 10 nanometers. This radiation permeates the crystal structure[110], absorbing energy and stimulating the atoms, which subsequently emit radiation in various directions. Radiation emitted by atomic planes in synchrony produces a coherent beam detectable by instruments. Bragg's law expresses the requisite condition for this radiation to synchronize.

- **Bragg's law**

When we analyze the directions in which a signal is detected, we observe a straightforward principle: if we envision parallel planes traversing the atoms and designate d as the distance separating these planes (also known as the "interplanar spacing"), constructive interference occurs under certain conditions.

$$2d_{hkl}.sin\theta_{hkl} = n.\lambda$$

Equation 2: Bragg's law

d_{hkl}: is half of the deflection

n: is an integer called "diffraction order

λ: is the X-ray wavelength (remember, we're working in monochromatic mode).

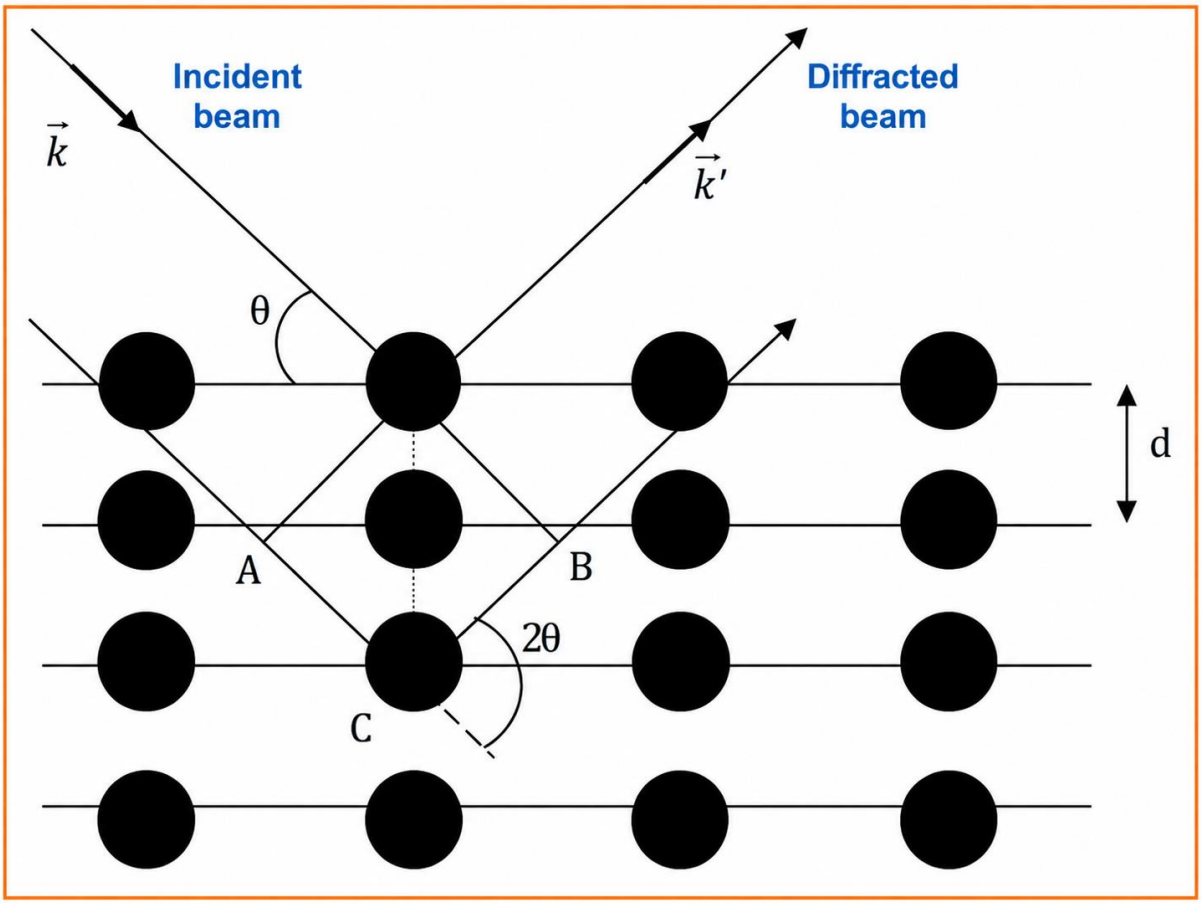

Figure II.5: Reflection of X-rays by a family of reticular planes spaced at distance d**[111].**

In the setup of a Bragg-Brentano diffractometer, the X-ray detector records peak intensities when positioned along a cone. This cone, although truncated within the sample due to X-ray absorption by both the sample and its holder, corresponds to imaginary atomic planes according

to Bragg's law. Each peak can thus be linked to specific sets of atomic planes, known as Miller indices (hkl), in a process referred to as peak indexing.

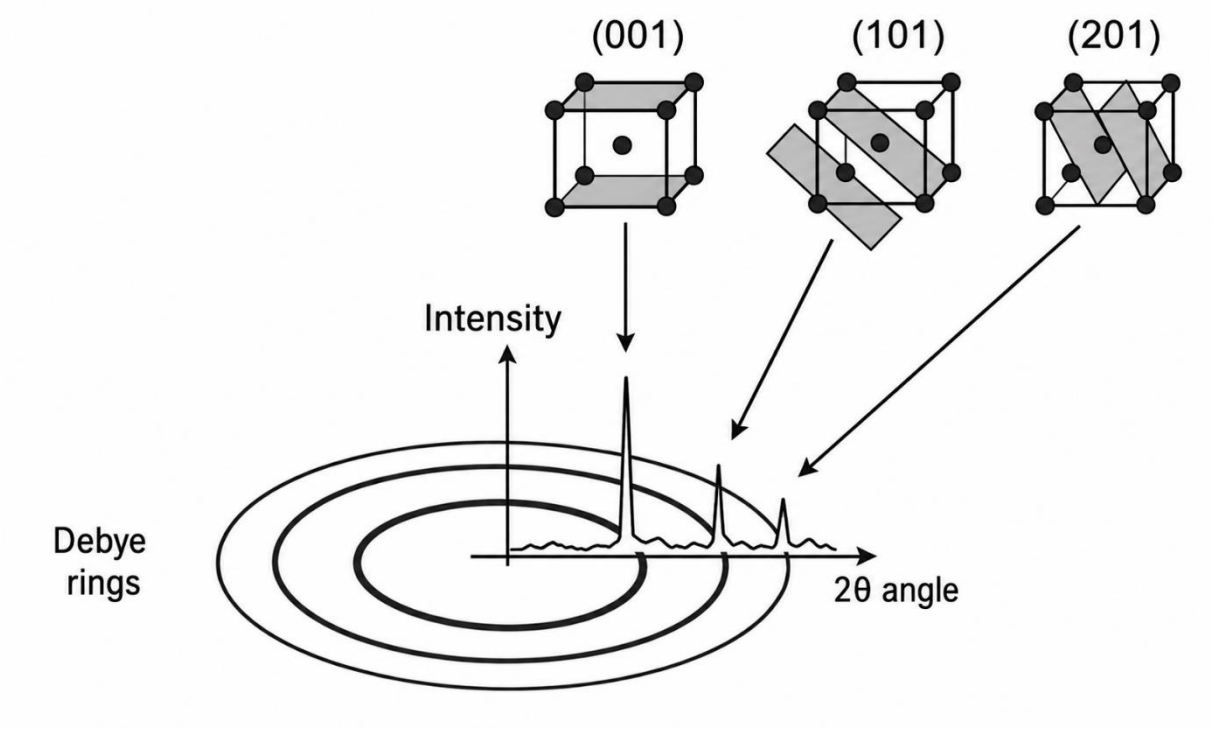

Figure II.6:illustrates the process of peak indexing, depicting the correlation between a diffraction peak and a specific atomic plane represented by Miller indices (hkl). Note the depiction of the incident beam's shape.

II.4.4 BET (Brunauer, Emmett and Teller)

The evaluation of a powder's surface holds significance in determining numerous properties. The method employed and the property under consideration greatly influence the outcome across various assessment techniques.

The BET method assesses the physisorption of gas to ascertain the "surface area" of a specimen.

Gas molecules can penetrate between particles and into all pores, cracks, and surface texture, to obtain a measurement of the microscopic surface area of the sample.

Frequently, the specimen is in powder or granular form, and the outcome is expressed as area per unit mass, mass area, or specific area.

It can also be calculated as area per unit volume, or as the absolute surface area of an object.

- **Application of BET theory (Brunauer, Emmett and Teller)**

The BET model is applied to determine the specific surface area of solids meeting the following assumptions:

- Adsorption is localized at defined sites.
- The adsorbate molecule is small enough to cover the solid surface well.
- Interactions between adsorbed molecules are negligible.
- From the second layer onwards, adsorption energy is constant and equal to the heat of liquefaction.

- **Calculation of specific surface area using the BET method**

The BET method (Brunauer, Emmet, and Teller) enables the determination of the specific surface area, S, of a sample[112]. This approach enables the determination of the volume, Vm, required to cover the surface with a monolayer of N2 molecules. While the fundamental assumptions of this theory seldom align with reality, this method yields consistent outcomes.

Practically, we employ the linear expression to describe monolayer formation, which is valid within the range of 0.05 < P /P0 < 0.35[113].

$$\frac{P}{Va(P_0 - P)} = \frac{1}{Vm} + \frac{C - 1}{C\ Vm} \times \frac{P}{P_0}$$

Va: Represents the adsorbed volume at relative pressure

Vm: The gas volume required to cover the entire surface of a monomolecular layer(volume adsorbed to the monolayer).

C: The BET constant, influenced by temperature and the variance between the adsorption energy of the initial layer and the liquefaction energy of the adsorbate, can be approximated by the following equation:

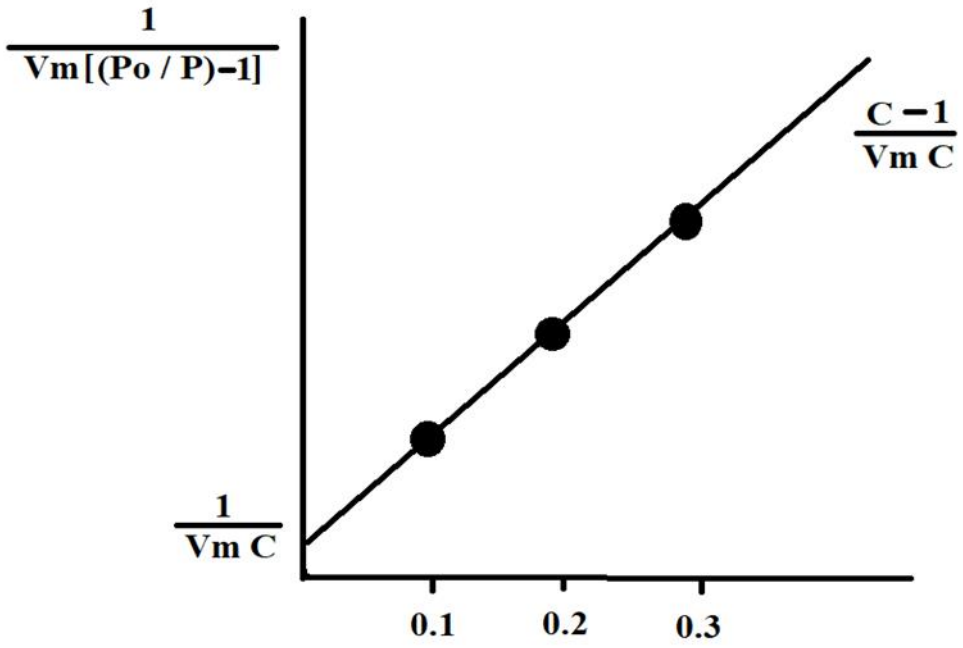

Figure II.7: Linear and real representations of the BET isotherm

$$C = exp\frac{(E_1 - E_L)}{R \times T}$$

The value E1 represents the heat released during the adsorption of the initial layer, while EL signifies the heat of liquefaction. Parameter C denotes the affinity between the adsorbed molecule and the solid surface: when this affinity is strong, E1 significantly surpasses EL, resulting in a high value for C (e.g., nearing 100). Conversely, in cases of weaker affinity, E1 approaches or equals EL, leading to lower values for C, potentially just a few units.

The S_{BET} surface area and C parameter can be deduced from the adsorption isotherms, by plotting where a straight line is obtained by

P/(Va(P0-P)) = f (P0 – P). The specific surface area and C parameter can then be deduced from the adsorption isotherms, and by extracting the slope value and y-intercept.

$$\frac{P}{V(P_0 - P)} = f(\frac{P}{P_0})$$

The BET surface area is calculated from Vm using the equation

$$S_{BET} = \frac{Vm \times Na \times a_m}{m \times Vm}$$

S_{BET}: Specific surface area in (m2/g).

Na: Constant (Avogadro number = 6.023 1023).

a_m: Surface area occupied by the N2 molecule (0.1627 nm2/nitrogen molecule).

m : Sample mass (g) and VM : The molar volume of N2 at TPN (22414cm3/mol).

- **Measuring the specific surface area of adsorbents**

The specific surface area of an adsorbent is defined as its surface area per unit mass. This metric serves to assess surface chemical characteristics such as the adsorption of chemical elements, metals, and phosphates in various substrates like soils and finely divided solids, as well as water retention capacity. Typically, it is quantified in units of square meters per gram (m2/g)[114].

The specific surface area offers insights into two key aspects:

- Adsorption capacity of solids: A higher specific surface area indicates a more effective adsorbent, as it provides more sites for adsorption to occur.

- Surface irregularities, including pores and other imperfections

These irregularities result in an actual surface that is always greater than the ideal surface without imperfections.

These features are reflected in the specific surface area measurement, offering information about the surface morphology and the availability of active sites for adsorption processes.

The utilization of the BET model forms the cornerstone of the most traditional approach to determining specific surface area.

Another technique for assessing specific surface area is known as the B-point method, which relies on analyzing the Type II isotherm graph. According to convention, this method identifies a pivotal inflection point labeled as "B."

At this juncture, the curve transitions from its Langmuir-like shape, exhibiting a reversal in curvature.

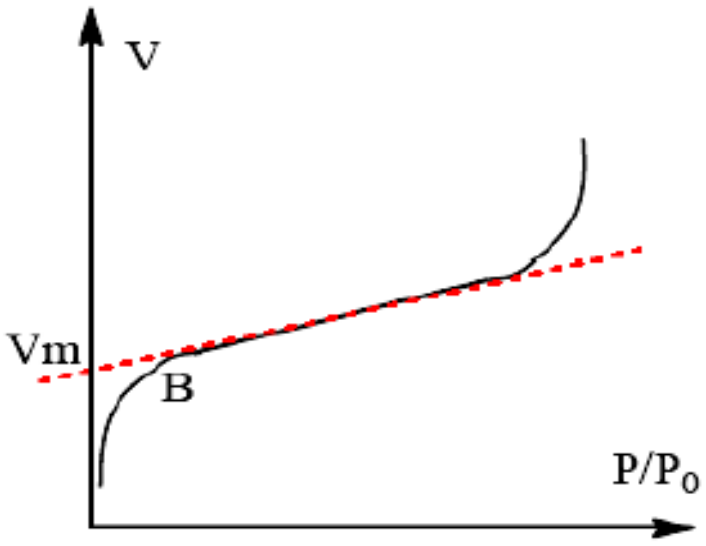

Figure II.8: Application of the B-point method to a type II isotherm

This method operates under the assumption that at this stage, the layer is monomolecular, whereas beyond this stage, multiple layers are present.

With the knowledge of Vm, corresponding to point B, and the specific area a_m, determining the catalyst's surface area becomes straightforward.

II.4.5 X-ray photoelectron spectroscopy

X-ray Photoelectron Spectroscopy (XPS) relies on the photoelectric effect first observed by H. Hertz in 1887[115], offering a non-invasive method to analyze surface properties. then explained by A. Einstein in 1905[116]. K. Siegbahn[117], who was awarded the Nobel Prize in Physics in 1981, pioneered the development of XPS technology in the 1950s, shaping its advancements to date.

XPS analysis involves examining the kinetic energy distribution of photoelectrons emitted from a sample when subjected to X-rays with a known energy (hν). The primary focus of this technique lies in observing how the binding energy of photoelectrons changes based on the chemical environment of the atoms they come from.

Utilizing this metrology, we can ascertain the electronic structure and chemical context of the atoms within the sample, quantify elemental composition across different layers, gauge the thickness of nanoscale surface layers, and potentially reconstruct chemical profiles by accessing angular information through the instrument. Due to the short mean free path of emitted photoelectrons within the material, typically on the scale of a nanometer, this characterization technique is particularly effective for surface investigations of the sample. Consequently, the depth of analysis is limited to around 10 nm[118].

X-ray photoelectron spectroscopy is based on the principle of conservation of incident photon energy.

The energy equation is outlined as follows: $\mathbf{h\nu = E_B + E_c + \varphi_{ech}}$, where **hν** represents the energy of the incident X-ray photon **(h étant la constante de Planck et ν la fréquence du photon incident), EB** denotes the binding energy of the electron to the nucleus, **Ec** indicates the kinetic energy of the ejected electron measured in vacuum, and $\boldsymbol{\varphi_{ech}}$ accounts for the energy necessary for the electron to traverse the material/vacuum boundary (exit work).

Figure 2.9 illustrates this principle of energy conservation:

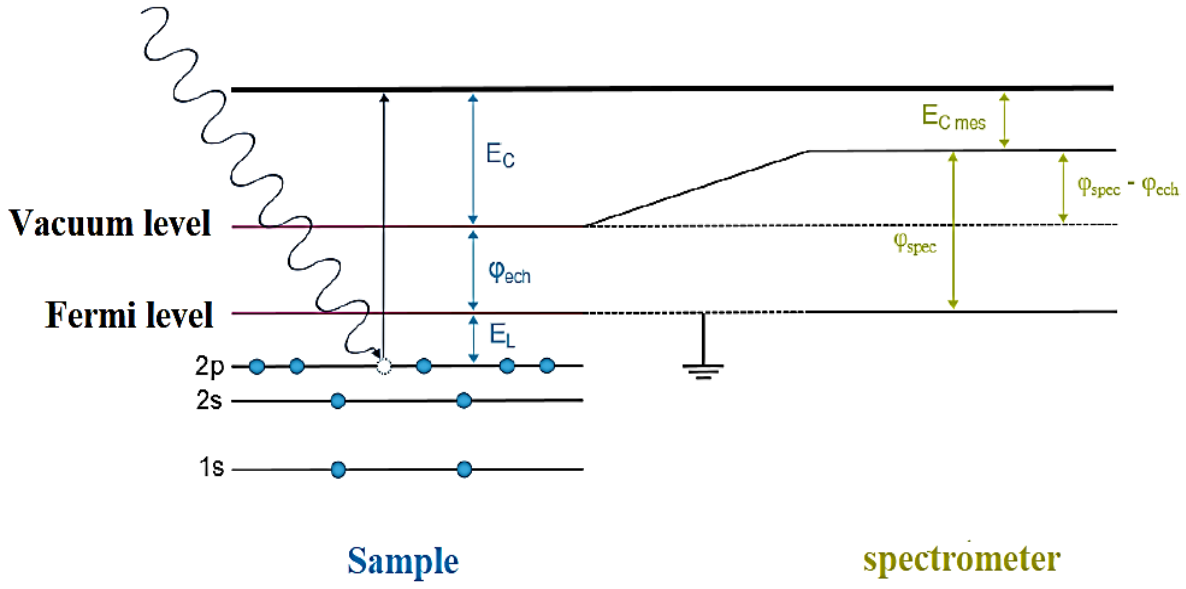

Figure II.9: Conservation of total energy during photoelectron phenomena, and when measured by a spectrometer.

In X-ray photoelectron spectroscopy (XPS), emitted photoelectrons are captured and analyzed based on their kinetic energies. By utilizing the energy balance equation, which involves constants W and hv, the bond energies (EB) can be calculated. This method relies on the atom-specific spectrum of core electron binding energies, allowing for the identification and quantification of elements within a compound. Essentially, XPS serves as an elemental analysis technique. **Figure II.10** exhibits distinct peaks corresponding to the S2p and S2s sulfur photoelectron , indicating the incorporation of the polymer into the carbon nanotubes.

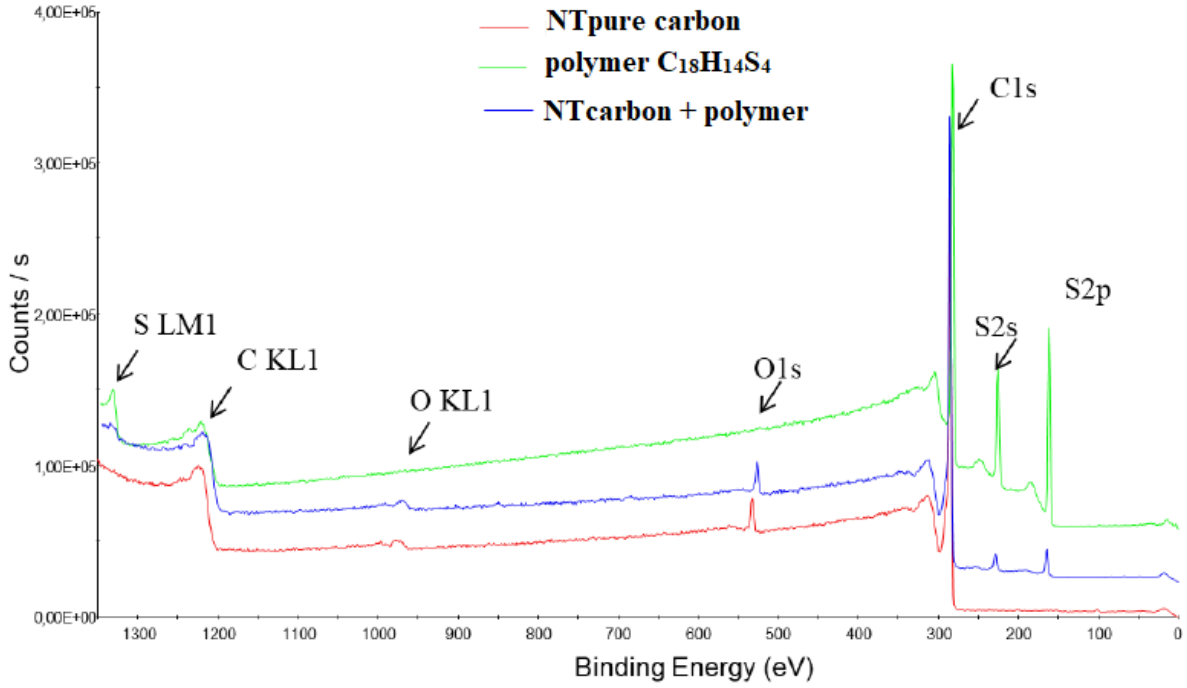

Figure II.10:shows an example of an XPS spectrum measured on a sample showing the presence of polymer in carbon nanotubes.

- **Experimental device**

An X-ray photoelectron spectrometer is comprised of several components: an X-ray source equipped with a monochromator, a sample manipulator, a series of collection lenses, an electron analyzer, an electron detection system, a computer for data processing, and an ultra-high vacuum pump essential for achieving a vacuum level on the order of $10^{-9} mbar$.

In this section, our attention is directed towards the X-ray source, the monochromator, and the photoelectron analyzer.

- **Source de rayonnement X**

X-ray radiation is generated when high-energy electrons collide with a metal anode, causing them to decelerate and release photons that exhibit the distinctive characteristics of the metal composing the anode. **Figure II.11** shows a schematic diagram of an X-ray source:

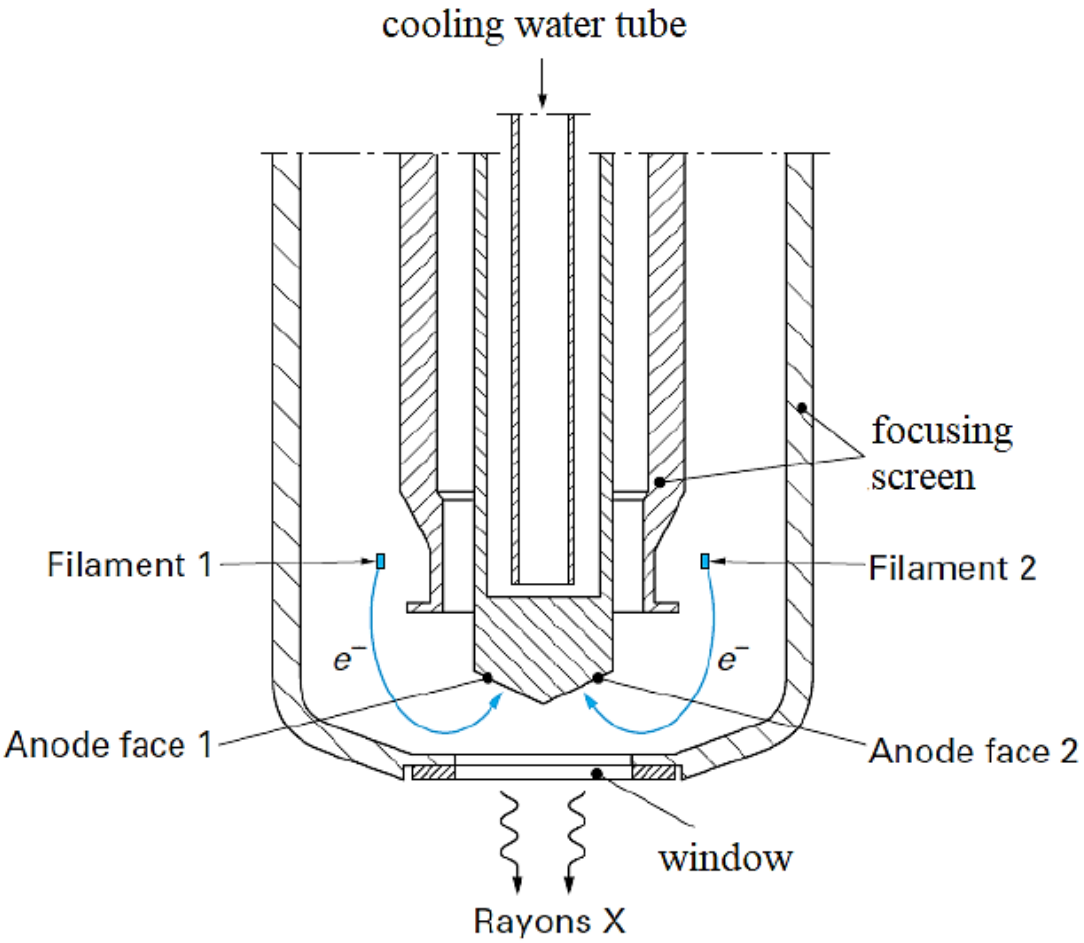

Figure II.12: Schematic diagram of an X-ray source [119].

A few amperes of current pass through the tungsten filament encircling the anode, inducing heating through the Joule effect. This temperature rise triggers the thermionic emission of electrons from the filament. Subsequently, these electrons are accelerated by a high voltage, reaching up to 20 kV, before colliding with the metal anode, thereby initiating the production of X-ray emissions. To safeguard against anode overheating from repeated impacts, a cooling circuit is employed to reduce its temperature. These operations occur within an environment of extremely high vacuum to preserve the integrity of the filament and other components of the high-voltage source. Additionally, this vacuum environment prevents any undesirable interactions between electrons, photons, and impurities.

- **Monochromator**

The monochromator offers the benefit of isolating a solitary line from the unresolved Kα1,2 doublet of X-radiation, effectively removing satellite peaks and suppressing the presence of the continuous white spectrum.

The method employed for constructing a monochromator relies on the dispersion of X-rays through diffraction on a crystal, following Bragg's law:

$$n\lambda=2d\sin\theta$$

With **n** the diffraction order

λ the X-ray wavelength

d the crystal's inter-reticular distance

θ Bragg angle

Figure II.12 illustrates a schematic representation of the monochromator, serving the dual function of wavelength selection and beam focusing onto the sample.

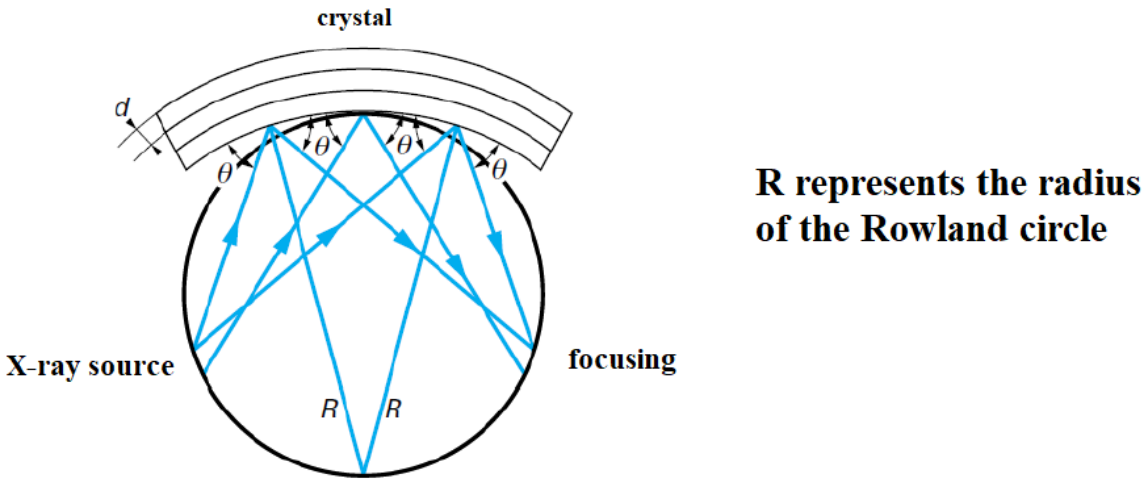

Figure II.13: Monochromator schematic diagram[119].

Quartz crystal proves to be an appropriate choice for such applications due to its slight flexibility when not excessively thick. Furthermore, it diffracts the Kα line of aluminum to first order at a Bragg angle of 78.5°.

- **Photoelectron analyzer**

During XPS measurements, photoelectrons emitted from the sample are gathered, sorted based on their kinetic energy, and subsequently detected by a specialized analysis system. This system is segmented into three distinct components: The input optics include electrostatic lenses designed to gather photoelectrons emitted by the sample and concentrate them onto the input slit of the analyzer. The analyzer then sorts the photoelectrons based on their kinetic energy, while the detector tallies the quantity of photoelectrons[119].

Among contemporary spectrometers, the 180° hemispherical concentric analyzer is commonly employed as the primary analyzer. **Figure II.13** illustrates its operational principle.

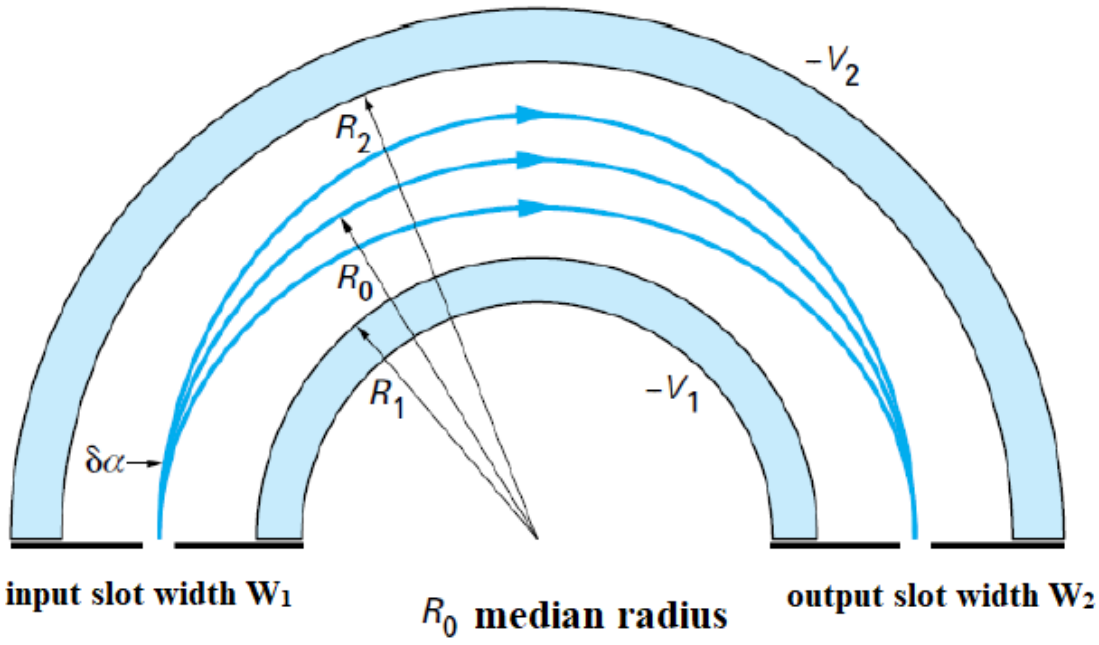

Figure II.14: Operation of the 180° hemispherical concentric analyzer [119].

The analyzer comprises two half-spheres positioned concentrically, where one has a radius denoted as R1 and the other as R2. The median radius is represented by R0. By applying

potentials of -V1 and -V2 to the inner and outer spheres respectively, an electric field perpendicular to the spheres' surfaces is established. The electric field causes the photoelectron trajectory to disperse based on their kinetic energy concerning a characteristic energy, Ea, dependent on the analyzer's geometry and the potential difference, V2-V1.

$$E_a = \frac{e(V_2 - V_1)}{(\frac{R_2}{R_1} - \frac{R_1}{R_1})}$$

Where **e** is the electron's charge.

Electrons entering the analyzer with energies lower than Ea experience significant deflection by the electric field, directing them towards the inner sphere upon impact. Conversely, electrons possessing energies surpassing Ea encounter minor deflection, leading them to strike the outer sphere. Consequently, only electrons with energy Ea are permitted to traverse the analyzer along the median circular trajectory, as depicted in **Figure II.14.**

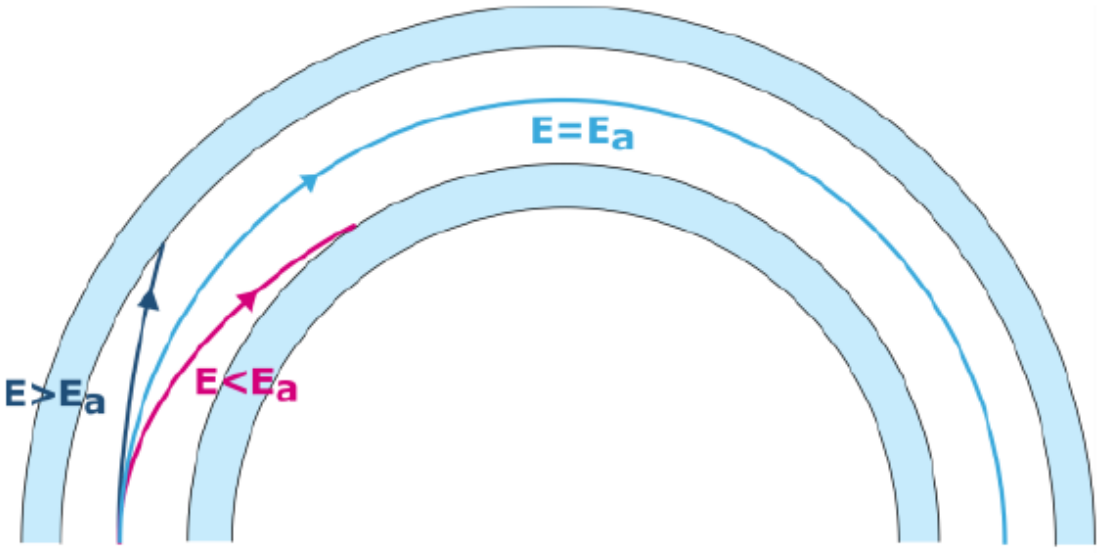

Figure II.15: Electron path through the analyzer as a function of input energy.

Energy resolution, denoted as ΔE, plays a critical role in XPS analysis. When the energy disparity between two XPS peaks, each representing distinct chemical environments, falls

below the ΔE resolution, differentiation between them becomes unfeasible, leading to a loss of information regarding these environments.

Energy resolution relies on the analysis energy Ea, the largest widths of the entrance and exit slits denoted as W, and the acceptance angle δα for photoelectrons.

$$\Delta E = E_a\left(\frac{W}{R_0} + (\delta\alpha)^2\right)$$

As the analysis energy Ea and slit width decrease, energy resolution also decreases. However, sensitivity improves with increasing Ea, and slits that are too closed decrease the number of photoelectrons detected, consequently elevating the signal-to-noise ratio. Therefore, finding a balance is essential.

In order to detect electrons with varying kinetic energies, they are subjected to a potential delay of **R** at the input of the detector, reaching up to the analysis energy **Ea.**

$$E_a = E_{cin} - eR$$

With $\boldsymbol{E_{cin}}$ the kinetic energy of the photoelectrons

Hence, by adjusting R, it becomes feasible to sweep across the energy spectrum. Alternatively, another approach involves modifying the voltages applied to the half-spheres to manipulate Ea, all the while maintaining the voltage R constant[119].

II.4.6 Photoluminescence Spectroscopy

The advent of lasers has significantly accelerated the advancement of spectroscopic detection methods. This is due to the valuable contributions of non-linear frequency mixing techniques in detecting luminescence from photoexcited materials, alongside the emergence of ultrafast laser sources driving the development of rapid detection electronics. Consequently, the field of spectroscopy has thrived, establishing itself as a formidable tool for characterizing materials and semiconductor devices. Moreover, the continual pursuit of novel light-emitting

devices and the demand for innovative materials further motivate the swift evolution of optical spectroscopy[120].

Photoluminescence (PL) spectroscopy serves as a valuable method for investigating and characterizing materials, shedding light on dynamic processes within them. This non-invasive technique provides insights into the electronic structure of materials without causing damage[121].

- **Basic Principle**

Photoluminescence (PL) involves the absorption of photons by a substance, followed by the re-emission of photons. From a quantum perspective, this process entails the excitation of electrons to higher energy states and their subsequent return to lower energy states, releasing photons in the process. When a photon with sufficient energy surpasses the material's band gap, it can elevate an electron from the valence band to the conduction band, bridging the forbidden energy gap through absorption. During photoexcitation, electrons typically acquire surplus energy, which they gradually dissipate before reaching the lowest energy level within the conduction band. Eventually, these electrons return to the valence band as their energy levels decrease. During this transition, the excess energy shed by the electron is transformed into a luminescent photon, which is then emitted from the material. Consequently, the energy exhibited by the emitted photon serves as a precise indicator of the material's band gap energy, denoted as Eg. This sequence of events, wherein photon excitation is succeeded by photon emission, is termed photoluminescence[122].

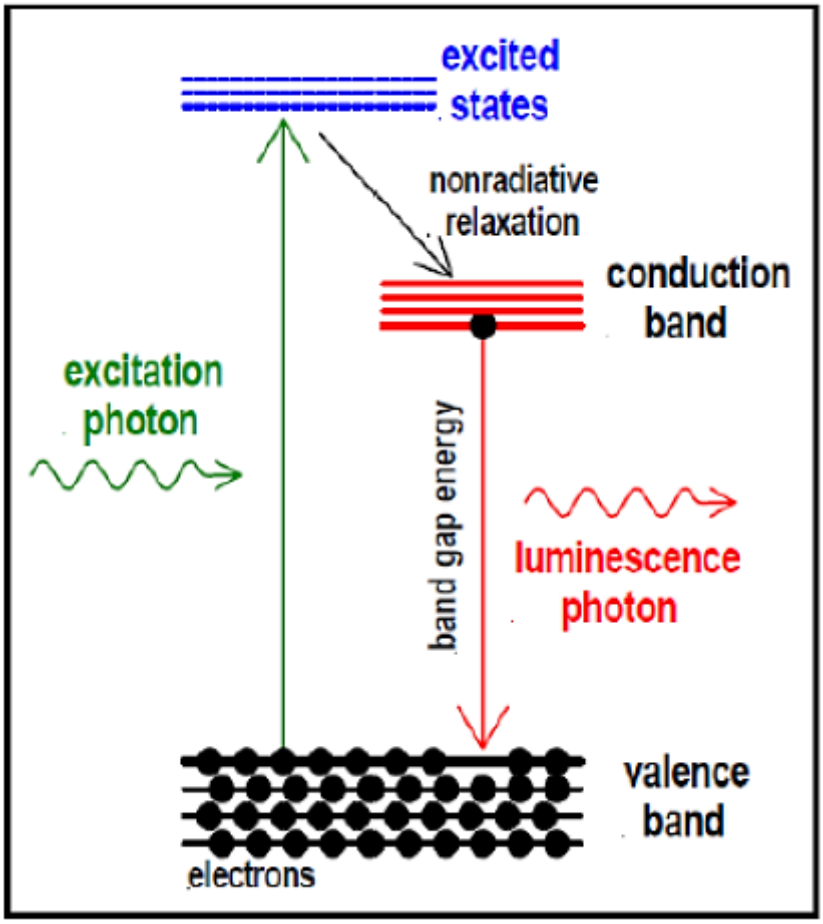

Figure II.16:illustrates the fundamental concept of photoluminescence spectroscopy (PL).

II.4.6.1 Photoluminescence exhibits various modes.

- **Resonant radiation:** When a photon with a specific wavelength is absorbed, it triggers an immediate emission of an equivalent photon. This process occurs rapidly, typically within about 10 nanoseconds, with minimal change in the internal energy of the chemical substrate between absorption and emission phases.
- **Fluorescence:** In instances where the chemical substrate experiences internal energy transitions prior to reemitting absorbed energy, the process remains swift. However, some of the initial energy dissipates, resulting in emitted photons with lower energy compared to those absorbed.
- **Phosphorescence:** Phosphorescence involves the absorbed photon energy transitioning through intersystem crossing to a state with higher spin multiplicity, typically a triplet state. Once trapped in this triplet state, quantum mechanics dictates that the transition back to lower singlet energy states is forbidden. As a consequence, there is a gradual

radiative transition back to a singlet state in phosphorescence, lasting from minutes to hours. The typical lifetime of phosphorescence ranges from 10^-4 to 10^-2 seconds, considerably longer than that of fluorescence. Consequently, phosphorescence is less common than fluorescence because molecules in the triplet state often undergo intersystem crossing to the ground state before phosphorescence can occur[121].

- **Instrumentation of photoluminescence**

An analytical instrument called a spectrofluorometer is employed to record and measure the fluorescence emitted by a sample. This device conducts scans of excitation, emission, or both wavelengths to capture the fluorescence data. Additional attachments enable the examination of signal variations concerning time, temperature, concentration, polarization, or other factors. **Figure II.16** depicts the block diagram of the fluorescence spectrometer. These spectrometers utilize laser sources, incorporating monochromators (wavelength selectors), laser sources for sample illumination, detectors, and corrected spectra[123].

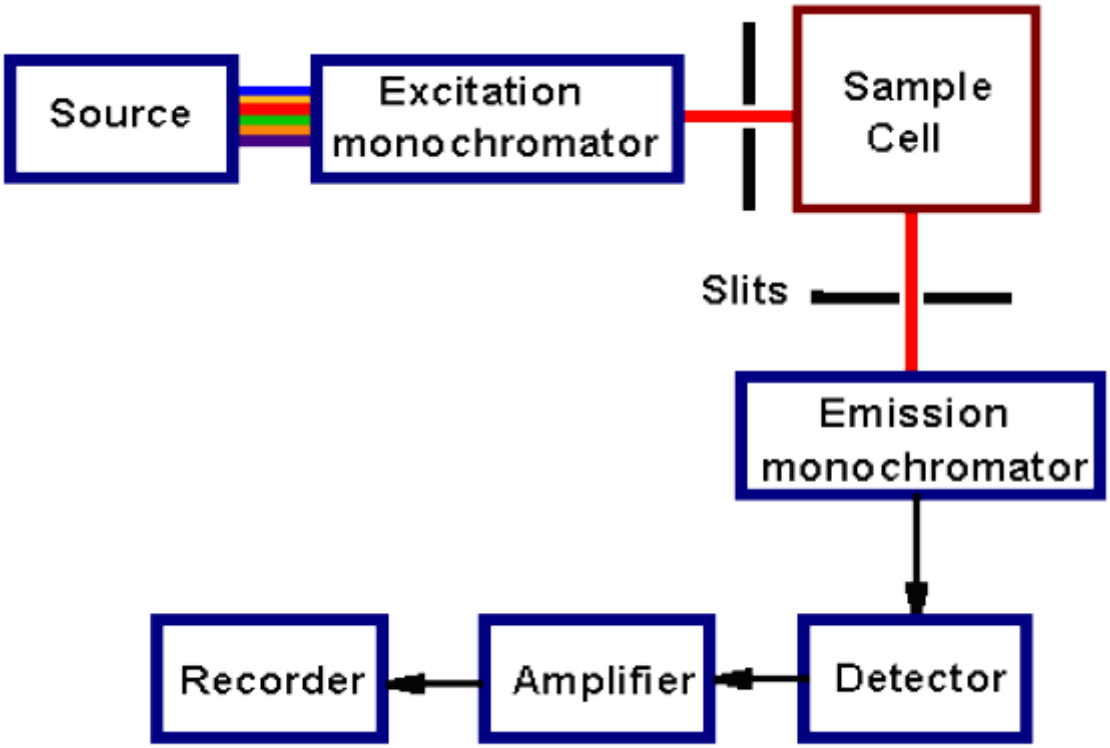

Figure II.17: Photoluminescence Instrumentation.

II.4.7 UV-visible spectroscopy

- **Definition**

UV-visible spectrophotometry is an analytical method that involves examining alterations in the light intensity transmitted through a colored solution within the wavelength range of 200 to 800 nm. This technique is widely utilized to ascertain the concentrations of absorbing substances across various applications[124]. The outcomes typically yield emission or absorption spectra, resembling curves that depict how absorption changes in relation to wavelength.

In molecular absorption spectrophotometry, we choose photons with a frequency ν_0 that the molecule being analyzed can absorb. Consequently, when a beam of intensity I_0 traverses through a solution containing the absorbing molecule, the intensity of the transmitted beam, denoted as I, decreases compared to I_0[125].

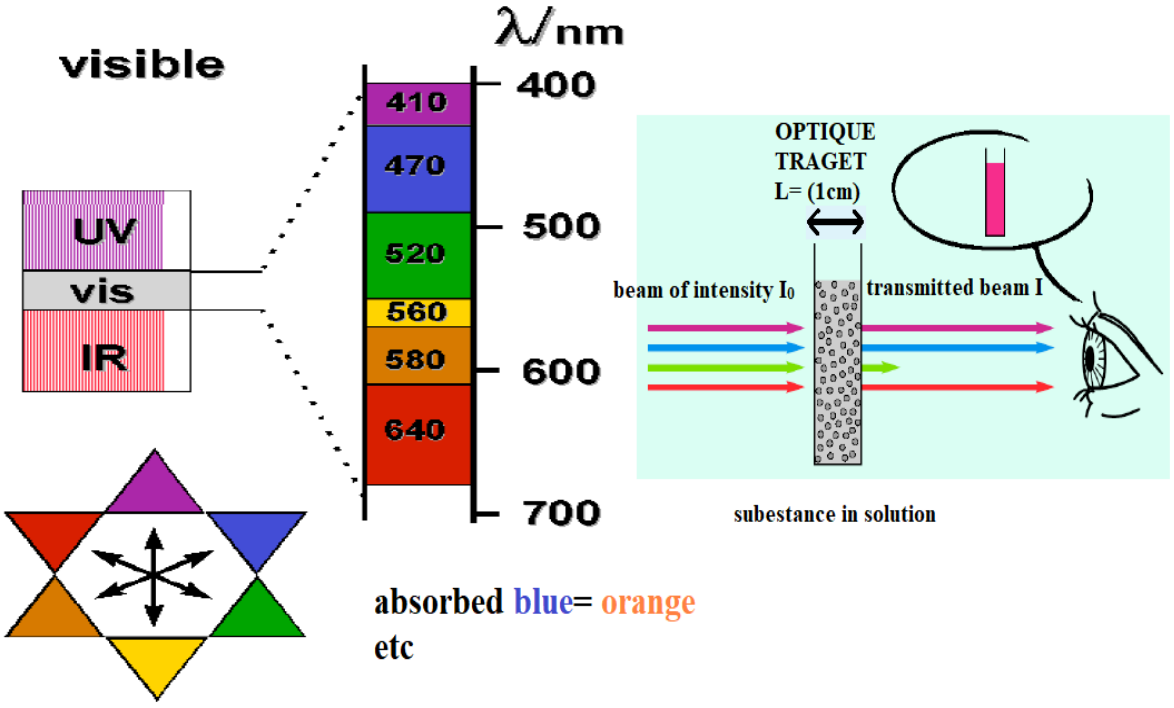

Figure II.18: Principle of molecular absorption spectrophotometry

UV-visible molecular absorption spectrophotometry finds applications in analyzing molecules dissolved in solution, serving both qualitative and quantitative purposes. In both scenarios, it relies on Beer-Lambert's law, which defines the correlation between transmitted intensity (I) and incident intensity (I_0). UV-visible spectroscopy enables the determination of concentration. Typically, this involves employing a calibration curve that correlates absorbance with concentration or utilizing the known molar extinction coefficient. This analytical method is frequently employed in a quantitative capacity to ascertain the concentration of a chemical species in solution, relying on Beer-Lambert's Law.

It has been demonstrated that:

$$\mathbf{A = -log_{10}\,(I/\,I_0) = \varepsilon Cl}$$

I/I_0: is the transmittance of the solution (unitless).

A : is the absorbance or optical density at a wavelength λ.

ε : is the molar extinction coefficient (in $l.mol^{-1}\text{-}cm^{-1}$). It depends on wavelength wavelength, the chemical nature of the entity and the temperature.

ℓ:is the length of the optical path in the solution through which it passes. the thickness of the cuvette used (in cm).

C: is the molar concentration of the solution (in $mol.l^{-1}$). In the case of a gas, C can be expressed as an inverse volume (units of length reciprocal to the cube, cm^{-3}).

This equation holds significant value in analytical chemistry. Specifically, with knowledge of **ℓ** and **ε**, the concentration of a substance can be inferred from a straightforward absorbance measurement at the given wavelength. Absorbance and extinction coefficient **ε** are sometimes defined using natural logarithms instead of decimal logarithms. While the Beer-Lambert law proves valuable in characterizing numerous compounds, it should not be regarded as universally applicable for determining the concentration and absorption of all substances. For highly intricate molecules, such as organic dyes like xylenol orange or neutral red, a quadratic relationship between the extinction coefficient and concentration is occasionally contemplated[126].

- **Principle of UV-visible spectrophotometry**

The spectrophotometer serves as a tool for determining the absorbance of a solution across various wavelengths. It achieves this by directing a beam of a selected wavelength through a cuvette containing the solution under examination (refer to **Figure II.18**). The molecules in the solution absorb the light beam to a greater or lesser extent, and the absorbance for that particular wavelength is defined accordingly.

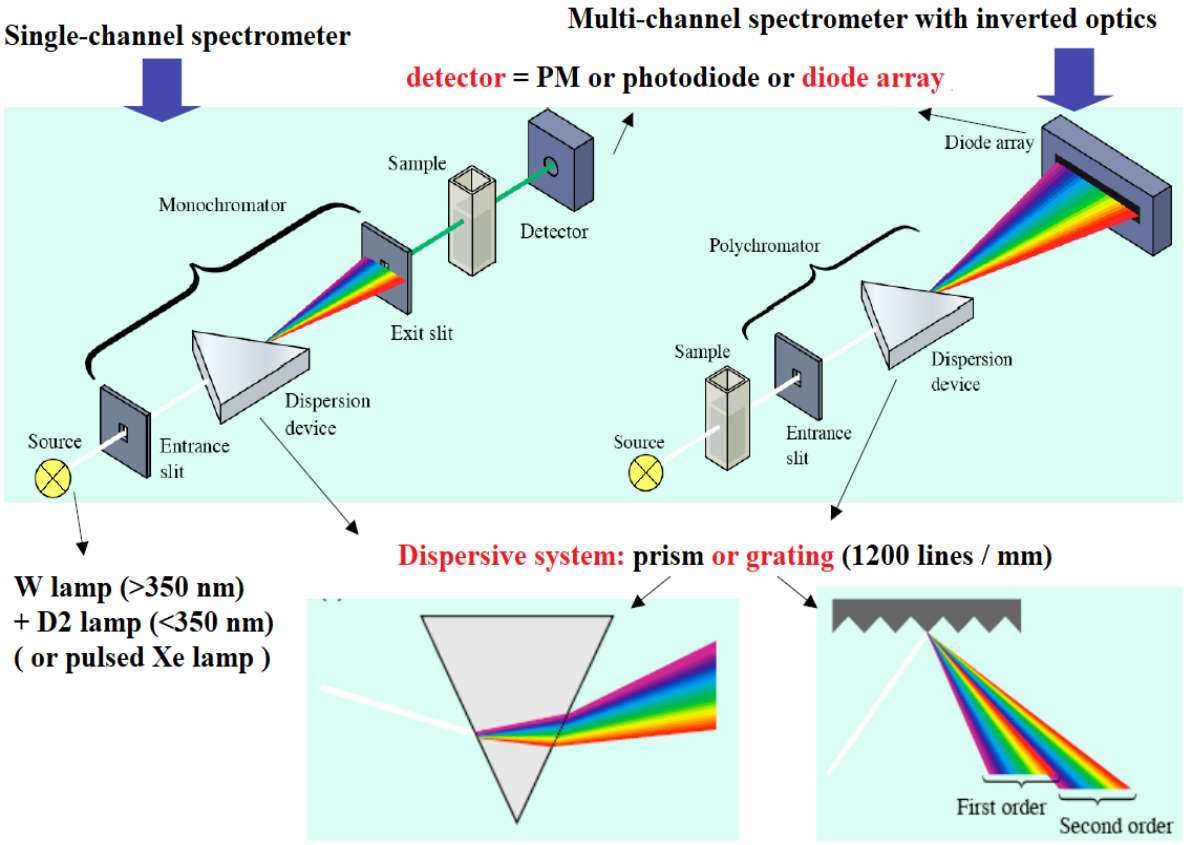

Figure II.19: Schematic diagram of a spectrophotometer ,Single- and multichannel single-beam spectrometer (with diode array)

Molecules exhibiting a UV-visible absorption spectrum absorb photons within the range of 190 nm to 800 nm, corresponding to their energy levels. Upon absorbing UV-visible photons, the energy of their valence electrons escalates, a phenomenon directly tied to changes in the molecular energy of electronic transitions[127].

III. Chapter 03: Solids characterization

III.1 Inroduction

The synthesis of silica nanoparticles (SiNPs) involves meticulous monitoring across varying synthesis temperatures, concentrations of products like templates, pH levels, and media of preparation. This comprehensive approach ensures precise control over the synthesis process and facilitates the production of high-quality SiNPs.

III.2 Characterization of Surfactants (CTAB and TX-100)

III.2.1 Surface tension measurements

Surface tension (γ) was measured using a Krüss K6 tensiometer with the platinum ring detachment technique. The concentration of surfactant was incrementally adjusted by adding small amounts of a concentrated surfactant solution. Readings were taken after each addition following thorough mixing, maintaining a temperature of 25 ± 0.5 °C. The γ values were calculated as the mean of three readings, with an accuracy of ± 0.5 mN/m. The critical micelle concentration (CMC) values were determined by extrapolating the linear portions of the γ versus surfactant concentration plots from both the pre-micellar and post-micellar regions, and identifying the concentration at the intersection point.

In an aqueous medium, surfactant solutions at low concentrations behave like simple electrolyte solutions, with most surfactant molecules existing as free monomers. However, when the concentration reaches a specific point called the critical micelle concentration (CMC), micelles begin to form. Within a homologous series, the CMC of surfactants is influenced by the number of carbon atoms in the hydrophobic chain. The length of the surfactant chain is a key factor in micellization [128], with hydrophobic interactions being the primary driving force. During micelle formation, entropy increases as water molecules in the hydration shell around the hydrophobic parts of monomeric amphiphiles are released. With longer hydrophobic chains, more water molecules are freed, resulting in a greater increase in entropy. Consequently, micellization occurs at lower concentrations, reducing the CMC value. Adding a single methylene group (-CH2) to the hydrophobic chain typically halves the CMC value. However, the influence of the head group and counter ion on the CMC is relatively minor. It has been reported that replacing the methyl group in dodecyl trimethyl ammonium bromide with an ethyl

group decreases the CMC from 15.13 to 13.97 mM. Since surface tension measurements are highly accurate and capable of detecting small micellar aggregates

Figure 3.1 illustrates the variation of surface tension versus the logarithm of concentration (log C) for the different surfactants used at 25 °C. It is evident that the CTAB surfactant exhibits a CMC at 1 mM. The number of carbon atoms in the alkyl chain and the head group of surfactants significantly influence their CMC values. For instance, nonionic surfactants like Triton X-100 (CMC = 0.21 mmol·L−1) have much lower CMC values compared to cationic surfactants like CTAB (CMC = 1mmol·L−1). Nonionic surfactants form a higher number of micelles at the same total surfactant concentration than ionic surfactants.

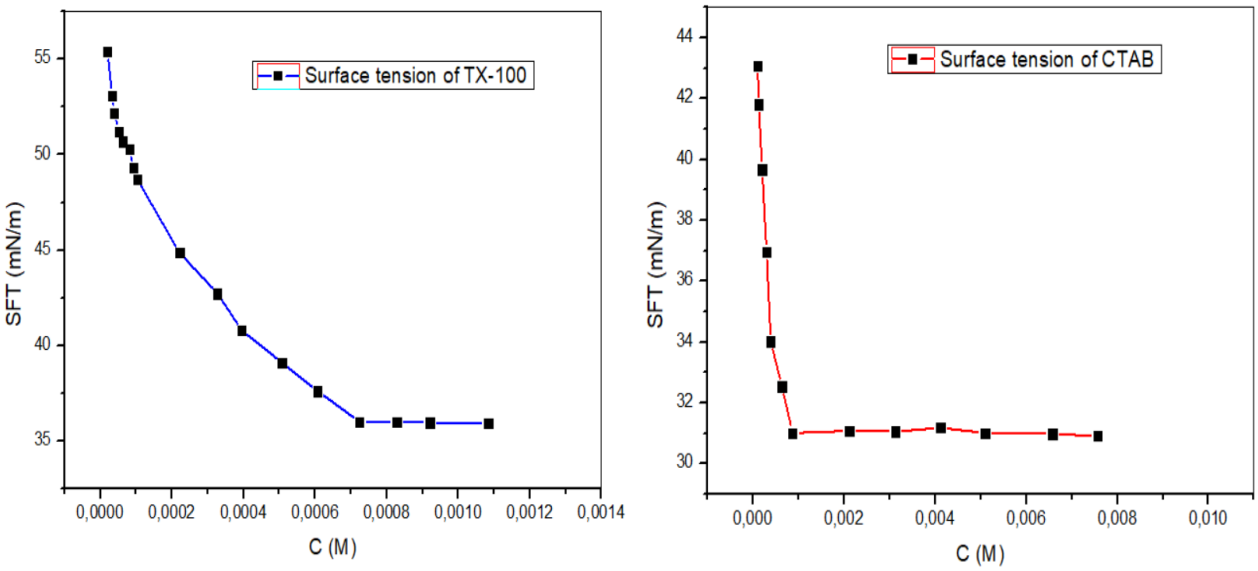

Figure III.1: Surface tension as a function of the of concentration of CTAB and TX-100

III.2.2 study of conductivity of CTAB as a function of temperature and concentration

Temperature also has an effect on the solubilization of ionic surfactants in solution. As the temperature rises, the solubility of ionic surfactants tends to increase slowly. **Figure III.2**. Above a certain temperature, known as the Krafft temperature, solubility increases very rapidly. This indicates that the surfactant's solubilization mode changes at the Krafft temperature. from monomolecular to micellar solubilization. micellar solubilization. The Krafft temperature corresponds to the point at which surfactant solubility reaches CMC. Below the Krafft temperature, the surfactant is not soluble enough for it to be in sufficient concentration to form micelles. The Krafft temperature depends on all the effects that can affect the CMC of a surfactant (chain length, polarity, etc.). The effect of electrolytes on Krafft temperature is more difficult to interpret, as they have a dual effect on CMC and solubility [129]

Temperature has two opposing effects on the hydrophilic character of hydrophilic character of non-ionic surfactants. A first increase in temperature to around 50°C produces a reduction in the hydration of the hydrophilic group. Hydrogen bonds depend on the agitation of water molecules. As temperature rises, this agitation increases, making it increasingly difficult to establish hydrogen bonds. This is the effect that produces the cloud point of non-ionic surfactants, which therefore tends to favor micellization: CMC decreases. On the other hand,

as the temperature rises, water molecules near the hydrophobic part become increasingly disorganized, so antagonism decreases and micelle formation suffers: CMC increases.

The Critical Micelle Concentration (CMC) is the concentration at which surfactant micelles start to form. The figure shows the conductivity of a CTAB solution at various surfactant concentrations. A noticeable change in the rate of conductivity increase indicates the CMC of the surfactant. The CMC for CTAB is 0.001 M. At surfactant concentrations below the CMC, the conductivity increases steeply due to the high ionization degree of surfactant molecules, as the monomers act as strong electrolytes. Beyond the CMC, the rate of conductivity increase slows down because of micelle formation. The electrostatic repulsion between individual micelles and the encapsulation of surfactant molecules' hydrophobic tails within the micelles lead to fewer binding sites for electron movement. This reduction in available binding sites decreases the net electrostatic charge and lowers the ionization degree. Additionally, the neutralization of micellar charge resulting from the electrostatic interaction between the hydrophilic head and hydrophobic tail within a surfactant micelle also contributes to the lower ionization degree. [17].

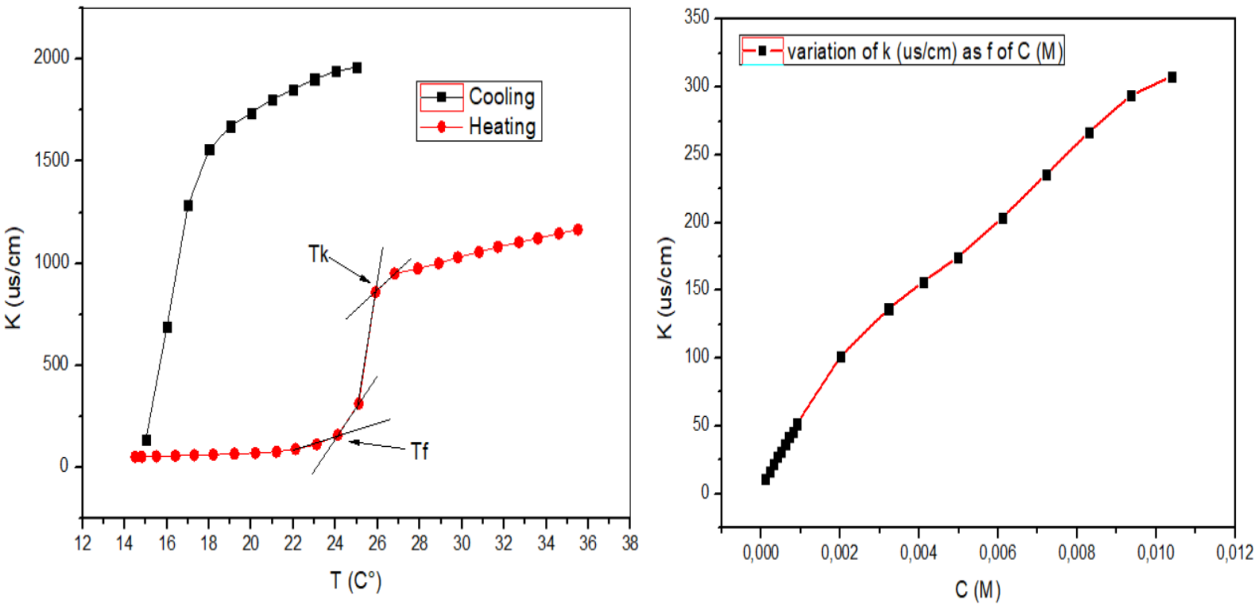

Figure III.2:conductivity of CTAB as a function of temperature and concentration

III.2.3 viscosity test of CTAB and TX-100 surfactants

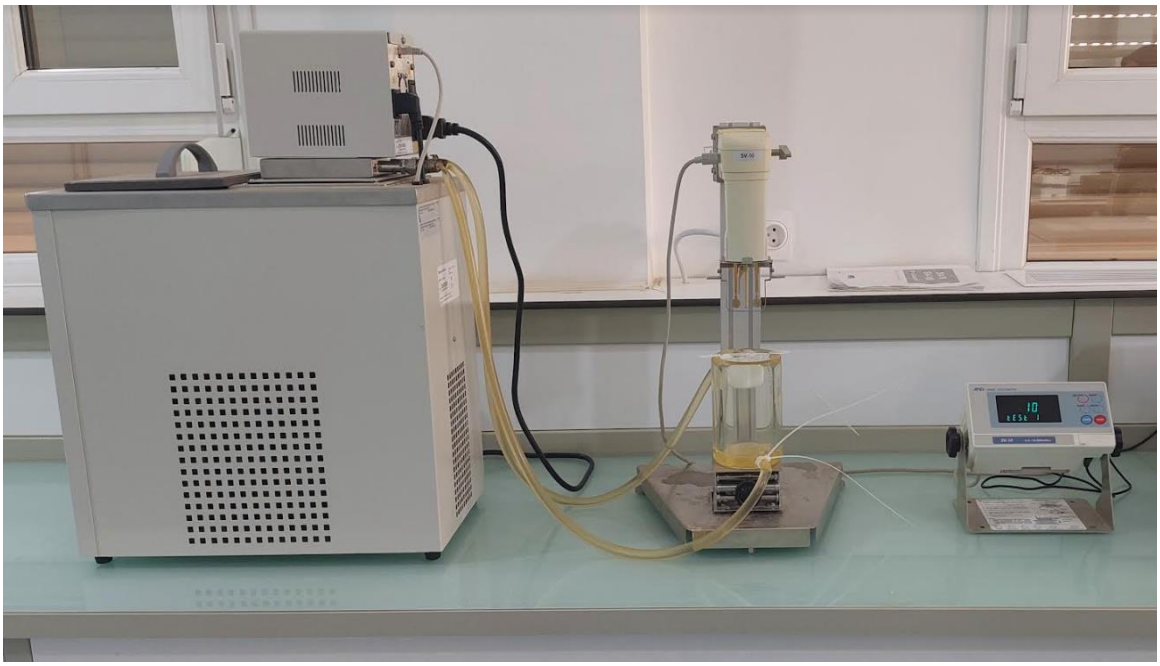

the study of the viscosity of the CTAB (cetyltrimethylammonium bromide) surfactant as a function of temperature reveals several key observations that suggest interesting physical transitions of the surfactant **Figure III.3**.

At 15 °C, CTAB is in a crystalline form with a viscosity of 15 centipoise (cp). This indicates that the surfactant molecules are in a highly ordered, solid-like state, resulting in relatively high viscosity. As the temperature increases from 15 °C to 17 °C, the viscosity increases to 20 cp. This increase could be due to the partial melting of the crystalline structure, leading to a more disordered liquid-crystalline phase. In this phase, the surfactant molecules are still somewhat ordered but can move more freely than in a solid state, resulting in higher resistance to flow (higher viscosity).

Beyond 17 °C, the viscosity begins to decrease significantly, reaching 2 cp at 27 °C. This suggests a phase transition from the liquid-crystalline state to a more disordered liquid state. As the surfactant transitions to a fully liquid phase, the molecular mobility increases, leading to a dramatic reduction in viscosity. The surfactant molecules are now able to move more freely, resulting in lower resistance to flow.

The viscosity remains constant at 2 cp from 27 °C to 36 °C. This indicates that the surfactant is now in a stable liquid phase where further increases in temperature do not significantly affect the molecular interactions and, consequently, the viscosity. The molecules are sufficiently disordered and mobile, maintaining a consistent low viscosity.

the viscosity of TX-100 (Triton X-100) surfactant as a function of temperature indicates another interesting set of phase transitions and behavior.

At 25 °C, the viscosity of TX-100 is very high, at 850 centipoise (cp). This suggests that at this temperature, TX-100 forms a highly structured and possibly gel-like phase, where the surfactant molecules are tightly packed or form large aggregates/micelles that significantly hinder flow, resulting in high viscosity.

As the temperature increases from 25 °C to 60 °C, the viscosity drops dramatically to 20 cp. This decrease suggests a phase transition from a structured or gel-like state to a more fluid, less ordered liquid phase. With increasing temperature, the thermal energy disrupts the structured arrangement of the surfactant molecules, leading to the breakdown of large aggregates or the melting of the gel phase into smaller micelles or individual molecules, thus reducing viscosity.

The viscosity remains constant at 20 cp from 60 °C onwards. This indicates that the surfactant has reached a stable liquid phase where the molecular interactions are no longer significantly affected by further increases in temperature. In this phase, the surfactant molecules are likely in a well-dispersed state, possibly as individual molecules or small micelles, resulting in low and stable viscosity.

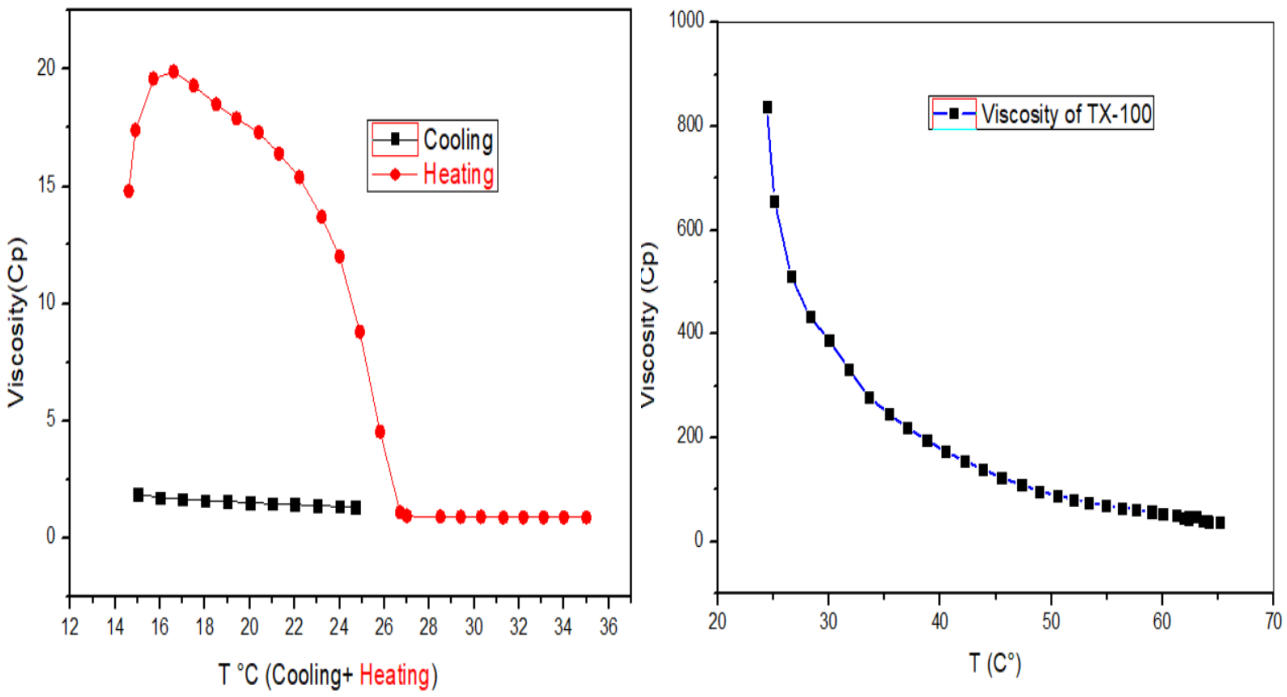

Figure III.3: Study of viscosity test of CTAB and TX-100 surfactants

III.2.4 Study of size of surfactants (CTAB , TX-100) using DLS

Dynamic Light Scattering (DLS) is a powerful technique for analyzing the size distribution of particles in a solution, particularly for studying micelles and other surfactant aggregates.

- **For CTAB (Cetyltrimethylammonium Bromide)**

First Peak at 2.4 nm:

This peak likely represents the individual micelles formed by CTAB. The size of micelles for CTAB in an aqueous solution is generally in the range of 2-5 nm, so 2.4 nm is a reasonable size for micelles.

Second Peak at 690 nm:

his larger peak suggests the presence of larger aggregates or possibly vesicles. In some cases, surfactant molecules can form larger structures due to interactions beyond simple micellization, leading to the formation of larger aggregates. The size of 690 nm indicates significant aggregation.

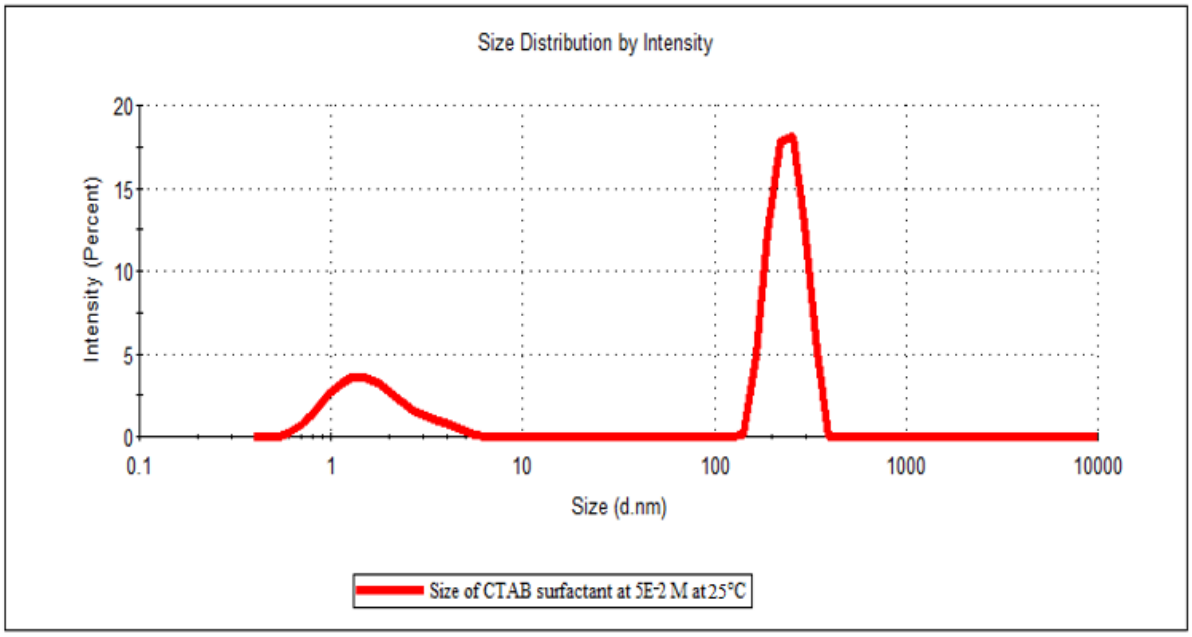

Figure III.4:size of surfactants CTAB surfactant at at 25°C and 5×10^(-2) M using DLS

- **For TX-100 (Triton X-100)**

First Peak at 11 nm:

his peak represents the micelles formed by TX-100. The typical size of TX-100 micelles is around 8-12 nm, so 11 nm is consistent with the expected size of TX-100 micelles.

Second Peak at 500 nm:

This intermediate peak suggests the presence of larger aggregates similar to the second peak observed for CTAB. These aggregates might form due to interactions between micelles

Third Peak at 5000 nm:

This very large peak indicates the presence of much larger structures, possibly larger aggregates of micelles. The formation of such large structures can occur due to a variety of factors including high surfactant concentration, temperature, and the specific nature of the nonionic surfactant TX-100, which can promote extensive aggregation under certain conditions.

The presence of multiple peaks in DLS data indicates a distribution of particle sizes rather than a single uniform population.

For both surfactants, the presence of larger peaks suggests that in addition to forming micelles, there are significant interactions leading to the formation of larger aggregates.

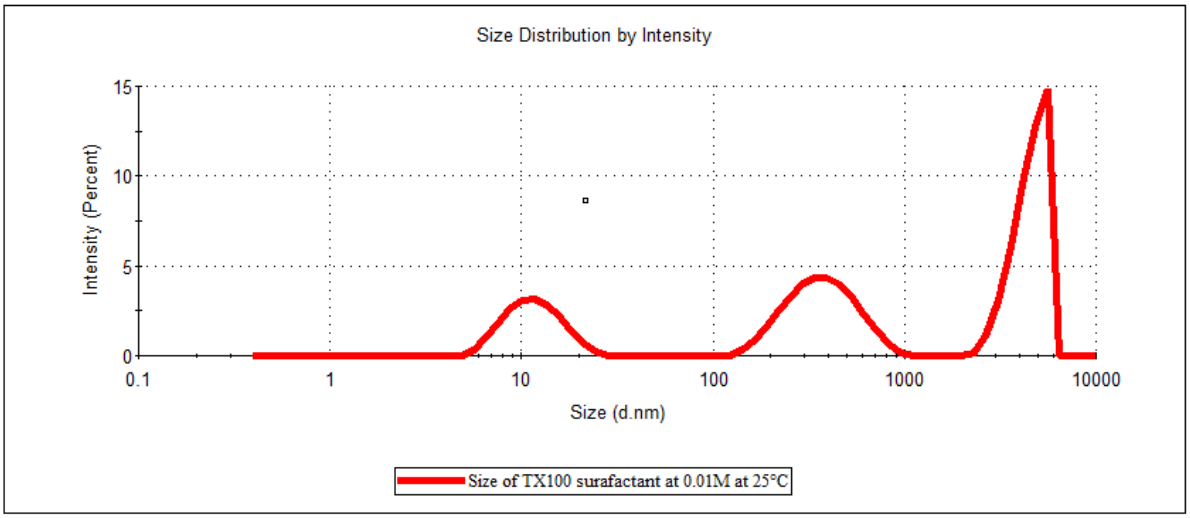

Figure III.5:size of surfactants TX-100 surfactant at 25°C and 1×10^(-2) M using DLS

Using Dynamic Light Scattering (DLS) to determine the size of CTAB and TX-100 surfactants in an organic solution (n-hexane and butane-1-ol).

- **For CTAB (Cetyltrimethylammonium Bromide)**

First Peak at 0.8 nm:

This very small peak likely represents the presence of individual CTAB molecules. In non-polar solvents like n-hexane, the CTAB molecules might not form typical micelles but instead exist as small clusters or monomers.

Second Peak at 250 nm:

This intermediate-sized peak suggests the formation of larger aggregates or possibly reverse micelles. In an organic solvent like n-hexane, CTAB can form reverse micelles where the hydrophilic headgroups are inside and the hydrophobic tails are interacting with the solvent. The size of 250 nm indicates these reverse micelles or small aggregates are relatively large.

Third Peak at 1700 nm:

This very large peak indicates the presence of even larger aggregates or possibly vesicle-like structures. In some cases, surfactants can form large, complex structures in non-polar solvents due to the tendency of the hydrophilic heads to cluster together more tightly, resulting in large aggregates.

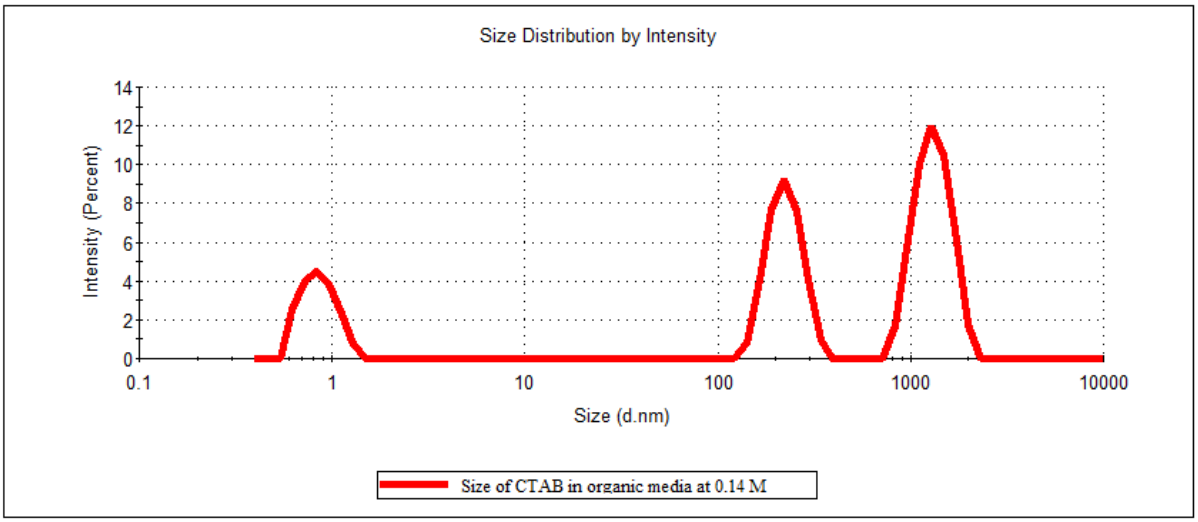

Figure III.6:size of surfactants CTAB surfactant in an organic solution (n-hexane and butane-1-ol) at 25°C and 1×(10)^(-1) M using DLS

Figure III 6: size of surfactants CTAB surfactant in an organic solution (n-hexane and butane-1-ol) at 25°C and 1×10^{-1} M using DLS

- **For TX-100 (Triton X-100)**

Single Peak at 95 nm:

The presence of a single peak at 95 nm suggests that TX-100 forms relatively uniform aggregates in the organic solvent mixture. This size indicates that TX-100 likely forms reverse micelles or small aggregates in the non-polar solvent environment. The relatively larger size compared to typical micelles in water (8-12 nm) is due to the different solvent environment promoting larger aggregate formation.

Reverse Micelles: Both CTAB and TX-100 can form reverse micelles in non-polar solvents like n-hexane. Reverse micelles have the hydrophilic headgroups inside and the hydrophobic tails interacting with the solvent, leading to different sizes and structures compared to aqueous solutions.

Solvent Influence: The combination of n-hexane and butane-1-ol affects the micelle formation, as butane-1-ol can act as a co-surfactant or cosolvent, influencing the micelle size and stability.

Aggregation: Larger peaks indicate significant aggregation, which can result from increased surfactant concentration and the nature of the organic solvent.

CTAB in Organic Solvent: Shows a wide range of aggregation states from small clusters or monomers (0.8 nm) to large aggregates or vesicles (1700 nm).

TX-100 in Organic Solvent: Forms relatively uniform aggregates (95 nm), likely reverse micelles, influenced by the solvent environment.

These interpretations provide insights into how surfactants behave differently in organic solvents compared to aqueous solutions, highlighting the role of solvent properties in determining micelle and aggregate structures.

- **Size of TX-100 surfactant $0.25\ M$ at 25°C**

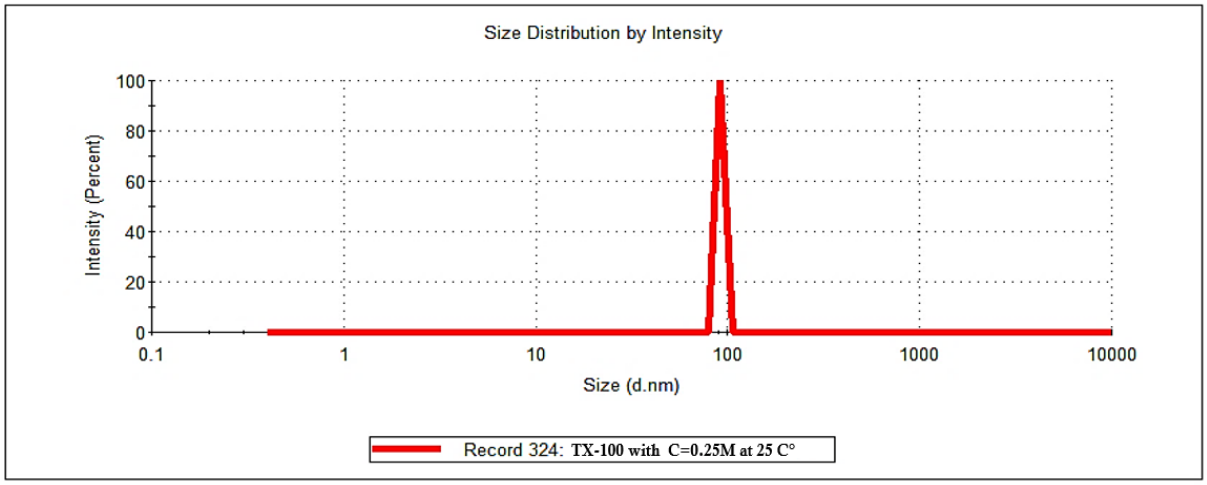

Figure III.7:size of surfactants TX-100 surfactant in an organic solution (n-hexane and butane-1-ol) at 25°C and 0.25 M using DLS

III.3 Preparation of monodispersed silica nanoparticles (SiNPs):

This study presents our investigation into the synthesis of silica nanoparticles employing two distinct methods: one utilizing an aqueous medium and the other employing the reverse microemulsion method in conjunction with the sol-gel process and cooperative self-assembly templating. Our primary focus is on understanding the impact of surfactant charge within the system, we conducted the synthesis through two different approaches, one in a microemulsion (W/O) based medium and the other in a water-based medium. In both methods, we employed a two surfactants: the cationic surfactant CTAB and the non-ionic surfactant TX-100 separately in both techniques, while keeping all other parameters fixed. This systematic approach enables us to exercise precise control over the size and ensure reproducible preparation of SiNPs, with a notable aim of achieving a size of 110 nm.

III.3.1 In aqueous medium

Synthesis of monodisperse SiNPs was carried out according to the method proposed by T. Ribeiro et al. [130] With little modifications. Briefly, a known amount of the surfactant (CTAB or TX-100) was dissolved in water (22 mL) at 25 °C under vigorous stirring. After 35 min, 1.75 mL of sodium hydroxide solution with a concentration of 2M, followed by a dropwise addition of 2.5 mL of TEOS within 5 min. Immediately, the reaction temperature was raised up to 40 C° and left under vigorous stirring for 2 h. After cooling, the obtained dispersion was centrifuged at 12000xg for 30 minutes and washed three times with a 1:1 water/ethanol mixture and one time with absolute ethanol. Afterward, the supernatant was removed and the precipitated gel phase was further dried at 60°C in a ventilated oven for 24 hours. The obtained powder was calcined at 500°C for 2 hours to retrieve pure SiNPs. The same experiment parameters were conducted at a low concentration of NaOH 0.2M.

III.3.2 In organic medium

- **SiNPs from Ionic surfactant CTAB**

Large Solide Silica spheres (LSiNPs) were prepared by firstly mixing (0.09 g) of cationic surfactant CTAB with deionized water (1.7 ml) at ambient temperature. After 10 minutes under vigorous stirring, (2 ml) of Butan-1-ol and (8 ml) of n-Hexane were added to the aforementioned aqueous solution. Secondly, after 10 minutes under stirring (800 rpm), a

dropwise addition of (0.3mL) TEOS is carried out followed by (0.06ml) of ammonia and the whole mixture is left 24h under stirring. An equivalent volume of ethanol is then added to the mixture to break the formed emulsion. The large LSiNPs were isolated by centrifuging the obtained solution at 14000 rpm for 30 min. The product obtained was further washed several times successively with ethanol and D.I. water to remove the unreacted chemicals. The final product was retrieved after a drying process at 60°C during 24 hours.

- **SiNPs from Nonionic surfactant TX-100**

For TX-100, 0.25 M of the nonionic surfactant was mixed directly with (2 ml) of Butan-1-ol and (8 ml) of n-Hexane at ambient temperature. The same protocol applied to CTAB preparation from the second step was adopted until the final stage and the purification of the nanoparticles by drying.

III.3.3 Results and discussion

In this study, we explore the synthesis of silica nanoparticles via two distinct methods: the conventional sol-gel process in water and the innovative water-oil process. By comparing the properties and characteristics of the nanoparticles produced through these two approaches, we aim to shed light on their respective advantages and limitations, offering valuable insights for the development of tailored nanoparticle designs.

III.4 Characterization of SINPs in Aqueous Medium

III.4.1 DLS of SiNPs in Water Mediated by (CTAB, TX-100)

The impact of varying the concentration of sodium hydroxide (NaOH) became evident when comparing the average diameters determined through dynamic light scattering (DLS) for synthesis of SiNPs from CTAB template. **Figure III.8** As the concentration of NaOH decreases, the average diameter also decreases, starting at 711 nm for silica nanoparticles with 2M NaOH and reducing to 271 nm (SiNPs) at 0.2M NaOH, all while maintaining a remarkably narrow size distribution. This observation aligns with findings from prior studies and can be attributed to the direct correlation between the hydrolysis rate of the silicate source and pH (for pH values greater than7)[85]. This impacts the equilibrium of charges at the outer layer of the micelles, consequently affecting the formation of micelle clusters that give rise to the particles. The pH's impact on the rate of hydrolysis introduces a time-dependent alteration in the repulsion forces between micelles. This becomes evident when we examine the reduction in the measured pH

following TEOS hydrolysis [131]The synthesis begins with an initial pH (pH_i) of 11-12, and the final pH (pH) varies from 10 (in the case of the highest NaOH concentration) to 5 (with the lowest NaOH concentration). This implies that, irrespective of the NaOH concentration used, the majority of the hydroxyl functional groups are consumed during the TEOS hydrolysis. However, the remaining quantity of hydroxyl ions undergoes a significant alteration in magnitude. This has a substantial impact on the charge equilibrium within the micelles[132], leading to enhanced repulsion (stability) at lower NaOH concentrations, resulting in smaller micelle clusters and, consequently, smaller nanoparticles.

To determine the effect of NaOH concentration on silica nanoparticle size with TX-100 as a template, we conduct experiments under varying NaOH (0.2M-2M) concentrations and on the same overall reaction conditions (SiNPs from CTAB template), including the concentration of silica precursors, reaction time, and temperature. and analyze the resulting particle size and morphology. At the end The base concentration of NaOH can affect the size of silica nanoparticles synthesized using different surfactants, including nonionic surfactants like TX-100. While the specific effect of NaOH concentration on silica nanoparticle size may vary depending on the synthesis conditions, it generally plays a role in controlling the reaction kinetics, pH, and growth of the nanoparticles. similar results are obtained with the nonionic TX-100 compared to the CTAB template even though the surfactants differ in the micelle size due to hydrophilic-hydrophobic interactions, CMC and concentration[133],The hydrodynamic diameter (Dh) obtained by dynamic light scattering SiNPs from (theTX-100 template and 0.2M NaOH) and SiNPs from (the CTAB template and 0.2M NaOH) in **(Figure III.8).**

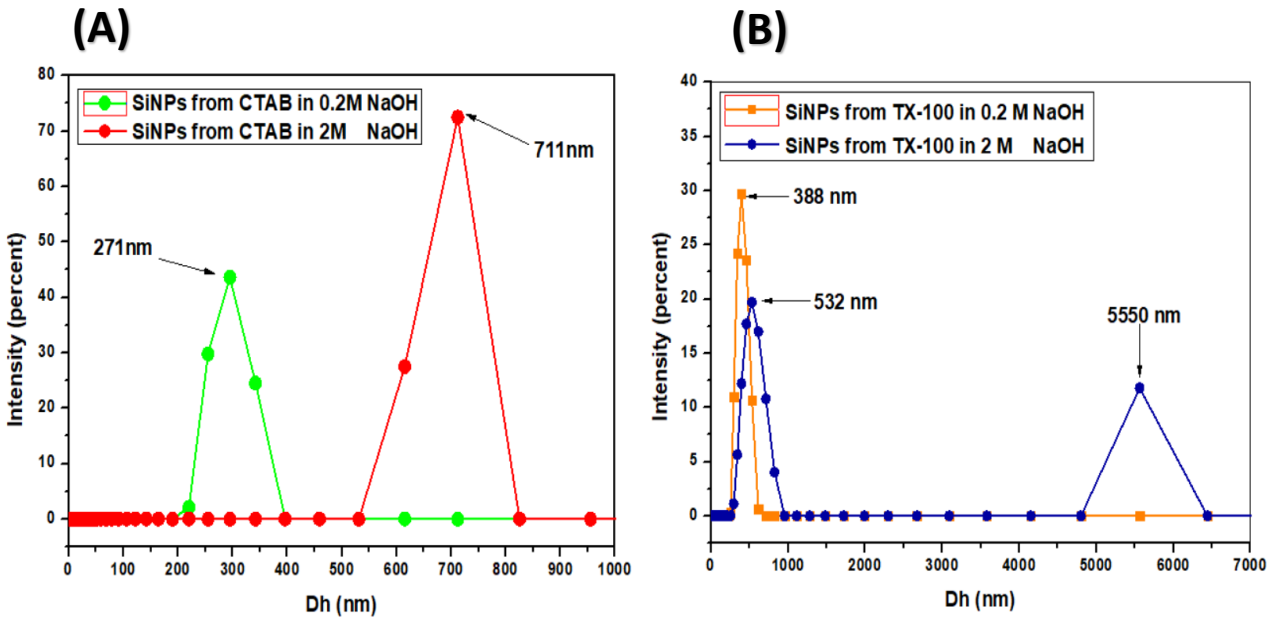

Figure III.8: The hydrodynamic diameter (Dh) obtained by DLS on SiNPs prepared via the aqueous process: **(A)** particle size distribution of SiNPs (CTAB template NaOH= 2 M); and particle size distribution of SiNPs (CTAB template NaOH= 0.2 M); **(B)** particle size distribution of SiNPs (TX-100 template at 2 M NaOH); and particle size distribution of SiNPs (TX-100 template at 0.2 M NaOH)

III.4.2 Scanning Electron Microscopy (SEM) of SiNPs mediated by (CTAB) in water preparation

SEM has investigated and unveiled the morphological and intriguing characteristics of silica nanoparticles, The SEM analysis of SiNPs **Figure III.9** reveals an average particle size of approximately 700 nanometers, this suggests that the primary dimension of the nanoparticles falls within this range. The well-defined size distribution further underscores the consistency in the size of these silica nanoparticles. The SEM analysis of SiNPs reveals a distinctive and intriguing morphology. Predominantly, the nanoparticles our sample exhibit a rod-shaped structure, and they maintain a high degree of uniformity in their shape. The prevalence of rod-shaped silica nanoparticles suggests a controlled and effective synthesis process. These rod-shaped nanoparticles are of significant interest due to their inherent anisotropy, Additionally, spherical silica nanoparticles could be observed, each with a diameter of approximately 100 nanometers [134]. in the context of their agglomeration state The rod-shaped silica nanoparticles are characterized by a loose agglomeration state, meaning they are not tightly aggregated , These loosely agglomerated nanoparticles form small clusters, which suggests some degree of attraction or adhesion between them ,The clusters of rod-shaped nanoparticles

may be due to electrostatic interactions, or other intermolecular forces that promote their proximity, The agglomeration state of the rod-shaped nanoparticles is likely influenced by factors such as surface properties (the CTAB surfactant). The SEM images reveal that the silica nanoparticles are distributed quite evenly across the sample surface. This even dispersion is a notable feature, indicating a relatively consistent distribution of nanoparticles. However, there are minor signs of aggregation or clustering, though they are not prominent. This suggests that while most of the nanoparticles are well-dispersed, there may be localized areas where a small number of particles have come together. The presence of some aggregation might be due to various factors, such as electrostatic interactions[134][135].

The Dynamic Light Scattering (DLS) analysis **Figure III.9** reveals that the hydrodynamic size of our silica nanoparticles from (the CTAB template 2M NaOH) is primarily centered at 685 nm, as indicated by the prominent peak in the size distribution. The Zeta Potential analysis, as revealed by Dynamic Light Scattering (DLS), unveils a bimodal distribution with two distinct peaks: one at -36.8 mV and another at -11.6 mV, shedding light on the surface charge characteristics of our silica nanoparticles derived from the CTAB template. The presence of two distinct peaks in the zeta potential distribution suggests that our silica nanoparticles from the CTAB template may consist of two subpopulations with different surface properties or charges. The peak at -36.8 mV is associated with highly negatively charged nanoparticles, which are expected to be stable and well-dispersed in the solution. The peak at -11.6 mV indicates another subpopulation with a slightly less negative zeta potential, which may still contribute to stability but could have different surface properties or interactions. Overall, this zeta potential data suggests that the majority of our nanoparticles are characterized by a highly negative zeta potential which suggests strong electrostatic repulsion between the nanoparticles.

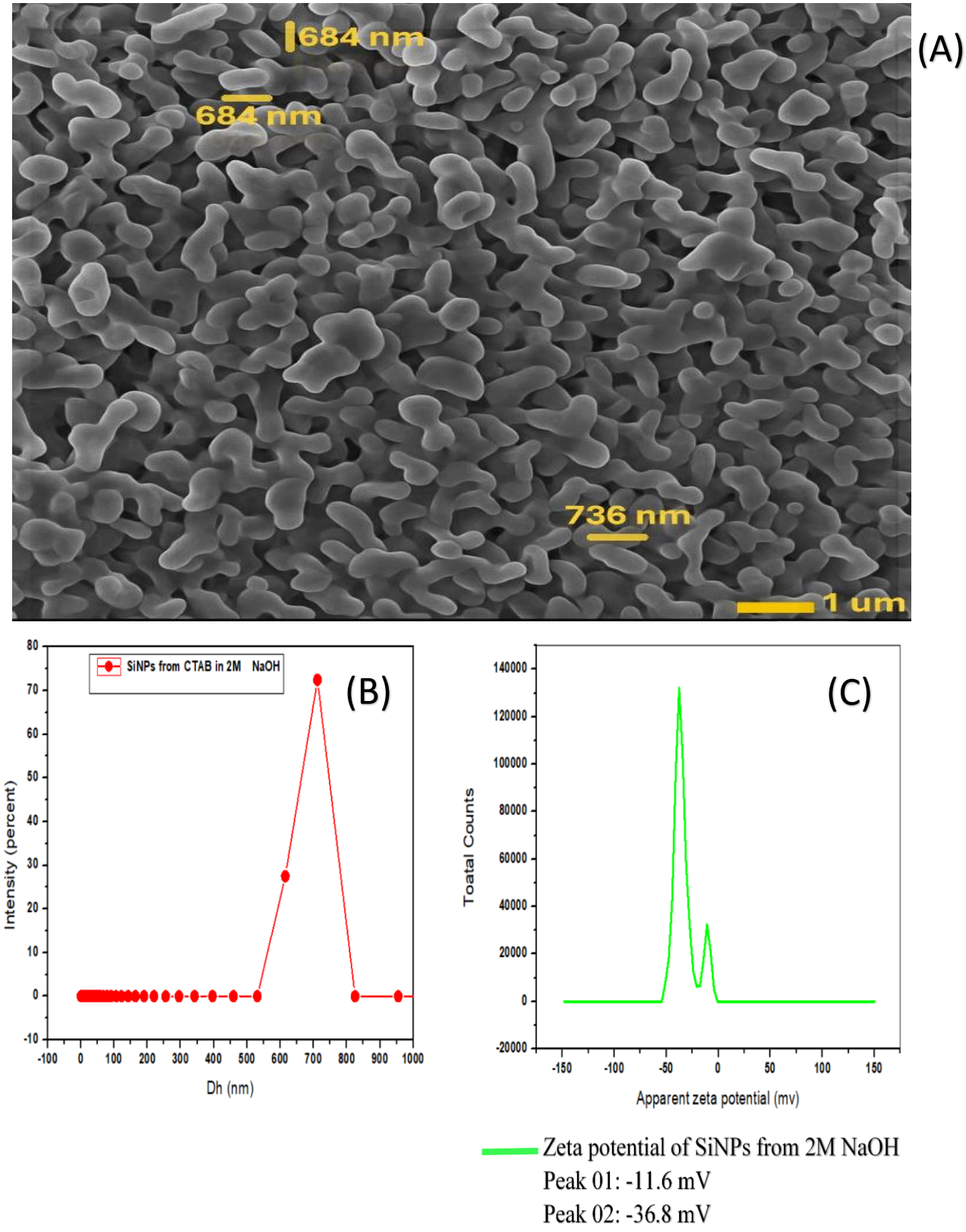

Figure III.9:(A) SEM image of SNPS (CTAB template (B) hydrodynamic diameter distribution SiNPS (CTAB template NaOH=2 M) (Polydispersity index = 0.5) ; (C) zeta potentials of SiNPS (CTAB template NaOH=2 M).

III.4.3 Scanning Electron Microscopy (SEM) of SiNPs mediated by (TX-100) in water preparation

The SEM images of SiNPs synthesized using the TX-100 surfactant as a template with a high NaOH(2M) base concentration in a sol-gel method **Figure III.10** reveal that the shapes characterized by the formation of Aggregates and Nanoclusters, These aggregates and nanoclusters appear to be composed of individual nanoparticles closely adhering to one another, giving rise to complex, multi-particle structures, Within these aggregates, there is a prominent feature: a "multilayer spherical aggregated structure and a more polyhedral shape appears[13]. This structure indicates that the individual nanoparticles within the aggregates are organized in a manner resembling spherical layers, It's important to note that while the individual nanoparticles may be roughly spherical in shape, the organization within the aggregates results in a distinctive multilayered configuration, The proposed mechanism of the formation of silica spheres. the SEM images show that the spherical nanoparticles are around 500 nm meanwhile the complete aggregate is bigger by around an order of magnitude.The behavior of nonionic surfactant (Triton X-100) after reaching the CMC (Critical Micelle Concentration) they start to aggregate into micelles. These micelles have a prolate shape with a monolayer or multilayer spherical aggregated structure with no obvious nonpolar-polar boundary[136] using TX-100 with high NaOH base concentration is an increased propensity for agglomeration of silica nanoparticles[13]. NaOH, can lead to rapid hydrolysis and condensation reactions in the sol-gel process, resulting in the formation of larger agglomerated structures.

III.4.4 DLS and the SEM analysis of SiNPs from TX-100 surfactant

The Dynamic Light Scattering (DLS) **Figure III.10**analysis reveals a bimodal size distribution of our silica nanoparticles from (TX-100 template and 2M NaOH) , presenting distinct peaks at 500 nm and 5000 nm, reflecting a complex structure of primary nanoparticles and multilayer spherical aggregates within the sample, The first peak at 500 nm represents the core size of individual spherical silica nanoparticles before aggregation. These primary nanoparticles are relatively uniform in size. The second peak at 5000 nm indicates the presence of much larger aggregates, characterized as multilayer spherical aggregated structures. These aggregates are formed when individual nanoparticles come together, leading to a significant increase in size. The Zeta Potential analysis, as revealed by Dynamic Light Scattering (DLS), demonstrates a highly negative zeta potential of -33.8 mV, indicating robust electrostatic repulsion and

excellent stability of the multilayer spherical aggregated structures within our silica nanoparticles from the TX-100 surfactant template.

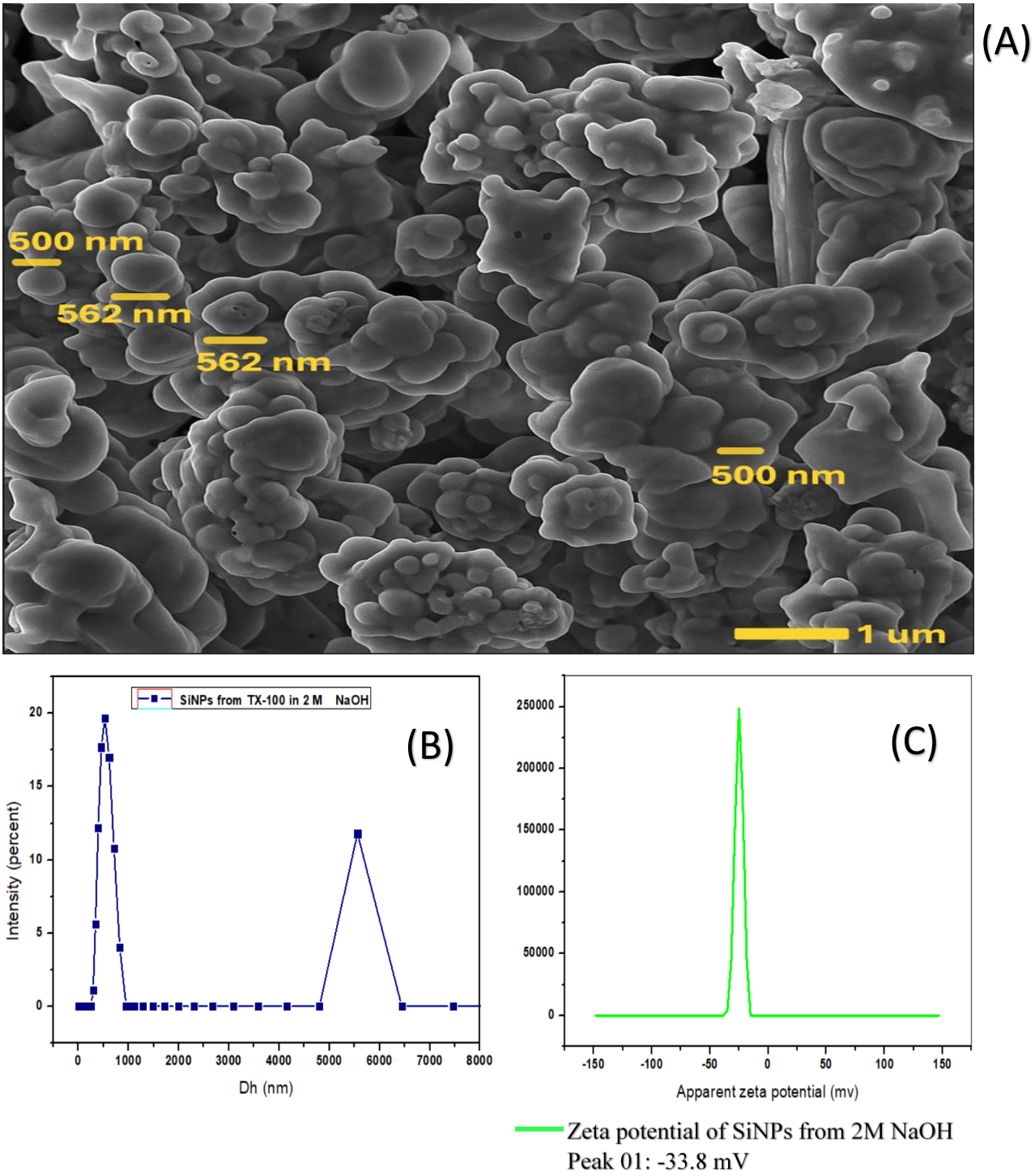

Figure III.10:(A) SEM image of SNPS (TX-100 template);**(B)** hydrodynamic diameter distribution SiNPS (TX-100 template NaOH= 2 M) (polydispersity index = 0.8); **(C)** zeta potentials=-33.8 mV of SNPS (TX-100 template NaOH=2 M).

III.4.5 Energy-Dispersive X-ray Spectroscopy (EDS)

The EDS analysis of silica nanoparticles (From CTAB Template) **table or Figure III.11**, reveals a composition dominated by oxygen and silicon. The high weight and atomic percentages of oxygen and silicon are consistent with the expected SiO2 structure. The presence of carbon is likely due to residual organic material, possibly from the CTAB surfactant. The weight and atomic percentages of carbon are relatively low, suggesting that the calcination process was effective in removing most of the organic contaminants. The presence of sodium in our sample due to the use of NaOH as a catalyst during the sol-gel process. The EDS analysis of silica nanoparticles synthesized using NaOH as a catalyst in the sol-gel process and calcined to remove the TX-100 surfactant yielded data similar to that of nanoparticles prepared from CTAB, indicating consistent elemental composition and successful removal of the templating agent .

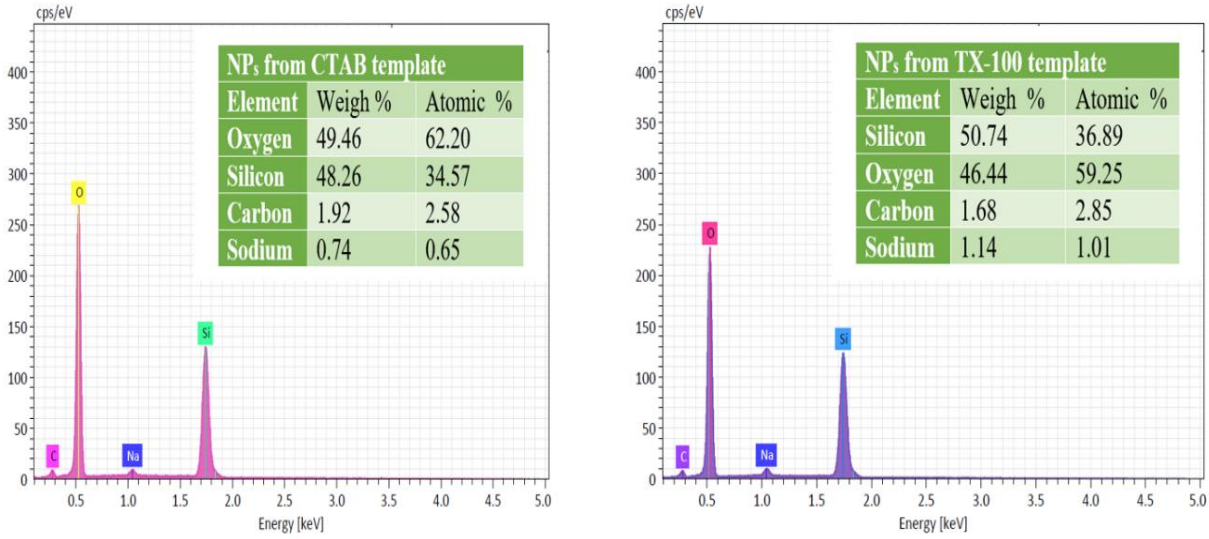

Figure III.11: The EDS analysis of SiNPs in water preparation and after calcination (From CTAB and TX-100 Templates and 2M NaOH) using Sol-Gel method in water environment

III.5 Characterization of SiNPs mediated by (CTAB, TX-100) in microemulsion

III.5.1 Scanning Electron Microscopy (SEM) of SiNPs mediated by (CTAB)

the SEM analysis of solid silica nanospheres formed from microemulsions(SiNPs from CTAB Water in Oil microemulsion) , (**Figure III.12)**The spherical solid shape of the majority of the silica nanospheres, with diameters around 285 nm, The presence of some silica

nanospheres with diameters above 1 μm indicates a degree of size variation in our sample.Consequently, with the addition of 0.14M CTAB, the hydrolysis reaction occurred so rapidly that TEOS droplets could not form. As a result, the silica spheres obtained under these conditions at 0.14M CTAB and NPs were in a solid state[137]. 1-butanol -water mixture was considered based on the trend showing that increasing the chain length effects the TEOS hydrolysis [138]. To stabilize TEOS water droplets, a1-butanol -water mixture and a specific quantity of CTAB are utilized. CTAB micelles envelop the water droplets, acting as templates for the creation of hollow silica spheres. Upon introducing an ammonia aqueous solution into these systems, hydrolysis of TEOS at the interface occurs, leading to the deposition of silica. The decrease in TEOS concentration at the interface prompts TEOS within the water droplets to diffuse from the interior to the interface due to concentration differences. Consequently, achieving silica spheres can be realized through calcination or washing. If not all of the TEOS inside diffuses to the interface, the spheres will exhibit partial hollowness or solidity, leading to a distinct morphology[137].The proposed mechanism of the formation of silica spheres is shown in **Figure II.2**. **Figure III.12**, similar to our synthesis of SiNPs

CTAB may promote the aggregation of silica nanospheres in certain conditions. This can lead to non-uniform particle size distributions and hinder the desired properties of the nanospheres. While CTAB can be effective in controlling the size and shape of nanoparticles, it may not be as precise or versatile as other surfactants . CTAB imparts a cationic charge to the nanosphere, This charge can affect the electrostatic properties, After nanoparticle synthesis Removing CTAB from the surface of silica nanospheres can be challenging. Its cationic nature can result in electrostatic interactions that keep it attached to the nanoparticle surface. In this emulsion system, the co-surfactant 1-butanol plays a crucial role in enhancing stability by facilitating the formation of smaller and more uniform water droplets. However, it's important to note that the cationic charge of CTAB surfactant can adversely affect the electrostatic properties of the nanoparticles, potentially hindering the beneficial effects of 1-butanol.

III.6 Aligning Dimension: Comparing SiNPs Size and Morphology via DLS and SEM

III.6.1 DLS and the SEM analytics of SiNPs from CTAB surfactant

The Dynamic Light Scattering (DLS) analysis **Figure III.12** reveals a complex interplay of particle size distribution, we have one peak at 283 nm with 10% intensity and another at 1700 nm with 24% intensity. This suggests that the larger nanospheres at 1700 nm are

contributing more to the overall scattering. **the Number Percent** This represents the contribution of each size particle to the number of particles present in the sample. the nanospheres at 283 nm have a higher number percent (30%), indicating that there are more nanospheres of this size. The discrepancy between intensity and number percent can occur due to the volume distribution of particles. If the larger nanospheres at 1700 nm are much larger in volume than the smaller ones at 283 nm, they will scatter more light (higher intensity percent) but are less numerous in the sample (lower number percent). The polydispersity index (PDI) of 0.8 suggests a relatively broad size distribution , It indicates that the particles vary in size, and some are significantly larger than others , and the tendency of these nanospheres to stick together. in the end the larger silica nanospheres contribute more to the scattered light intensity, while smaller ones dominate in terms of the number of particles present in the sample. using Dynamic Light Scattering (DLS), providing insights into their zeta potential **Figure III.12** The positive zeta potential of 31 mV for our silica nanospheres synthesized via a water-in-oil emulsion using a CTAB cationic surfactant as a template suggests electrostatic stabilization, which typically prevents particle aggregation in a colloidal suspension. However, the observed tendency of the nanospheres to stick together in SEM images despite this positive zeta potential can be explained by Surface Chemistry, The cationic surfactant CTAB used in the synthesis can provide a positive surface charge to the nanospheres, contributing to the positive zeta potential[32]. Even with a positive zeta potential, agglomeration can still occur due to weak physical forces or other factors. The size and shape of the nanoparticles can also influence their propensity to agglomerate. Smaller particles might experience stronger Brownian motion, which hinders agglomeration. **Figure III.12**

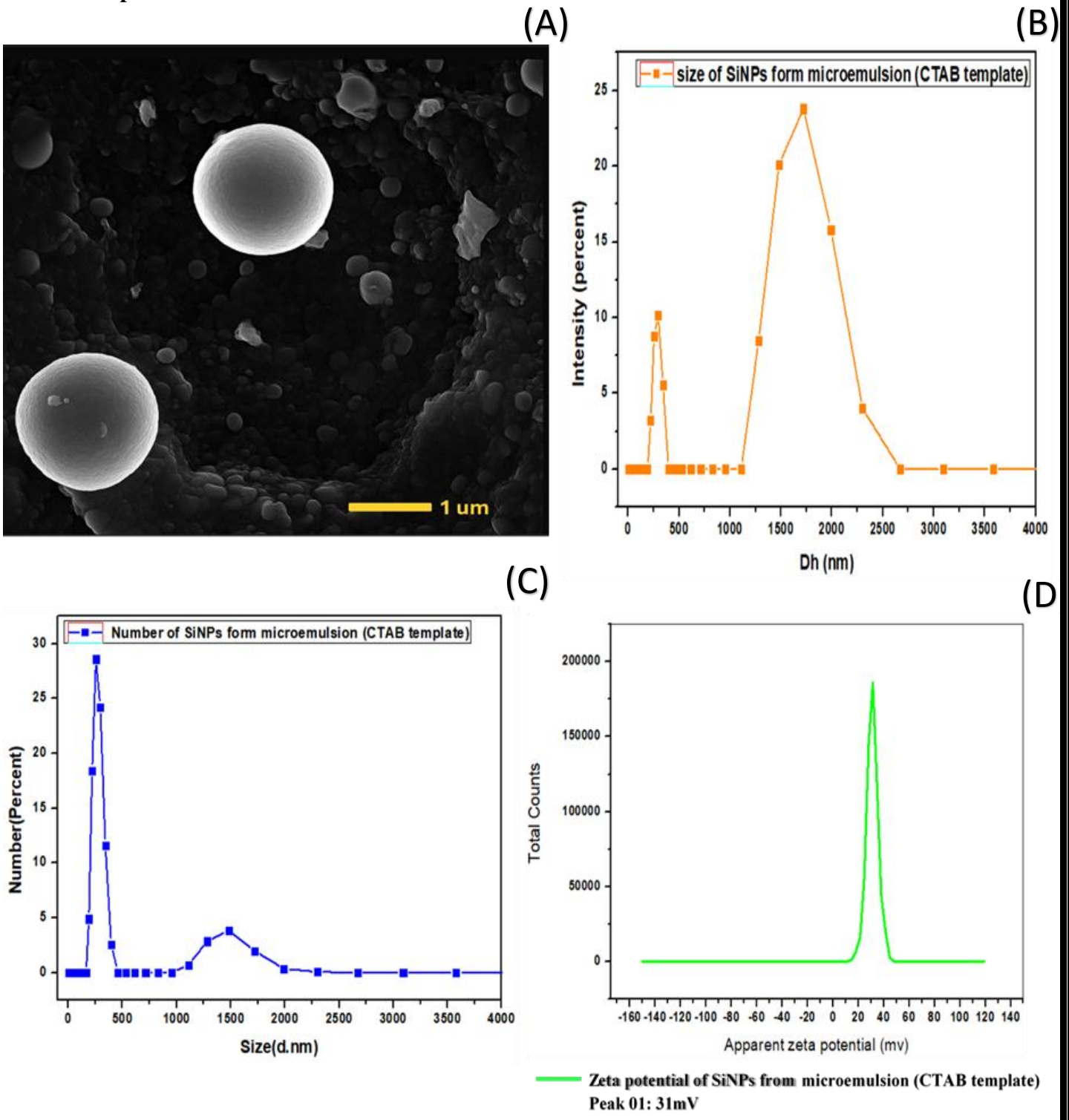

Figure III.12:(A) SEM image of SiNPS (CTAB template **(B)** hydrodynamic diameter distribution SiNPS (CTAB template) (polydispersity index = 0.8); **(C)** the number of hydrodynamic diameter distribution NPS (CTAB) (Polydispersity index = 0.8) ;**(D)** zeta potentials of SiNPS (CTAB template 31mV).

III.6.2 Scanning Electron Microscopy (SEM) of SiNPs mediated by (TX-100)

SEM analysis of silica nanospheres synthesized by emulsion via water in oil using TX-100 nonionic surfactant as the template **Figure III.13**. The silica precursor, initially soluble in the oil phase, hydrolyzes by diffusion on contact with aqueous micelles. The hydrolyzed silica monomers thus formed migrate into the aqueous phase, where they condense to form a nanoparticle. The hydrolysis step can be carried out either by acid or base catalysis. The condensation step, on the other hand, requires catalysis that can only be basic to obtain spherical nanoparticles. This stage therefore requires the addition of a base, generally ammonia [139]**.** The average size of the silica nanospheres is approximately 110 nm **Figure III.13,** This suggests that the synthesis process is producing relatively uniform-sized nanoparticles, the silica nanospheres exhibit a uniform spherical shape, The loose agglomeration and clean surface the absence of debris or contaminants on the surface of the nanoparticles is a positive sign.

III.6.3 Coherent Finding of SiNPs of Size and Morphology Harmony with DLS and SEM

The DLS hydrodynamic size of 107 nm **Figure III.13** and the SEM size of 110 nm are remarkably consistent. This suggests that the silica nanospheres are well-dispersed , The low polydispersity value of 0.2 in the DLS analysis indicates that the size distribution of the nanoparticles is very narrow and that most of the particles are very close in size to the measured 107 nm.

A zeta potential of -25.1 mV **Figure III.13** indicates that the silica nanospheres have a negatively charged surface ,The negative charge is typically attributed to the presence of surface groups, such as silanol (Si-OH) groups, which are common on the surface of silica nanoparticles. A zeta potential of -25.1 mV, while negative, is moderately strong and suggests good electrostatic stability. Nanoparticles with a relatively high absolute zeta potential value (positive or negative) tend to repel each other, which can prevent aggregation or agglomeration

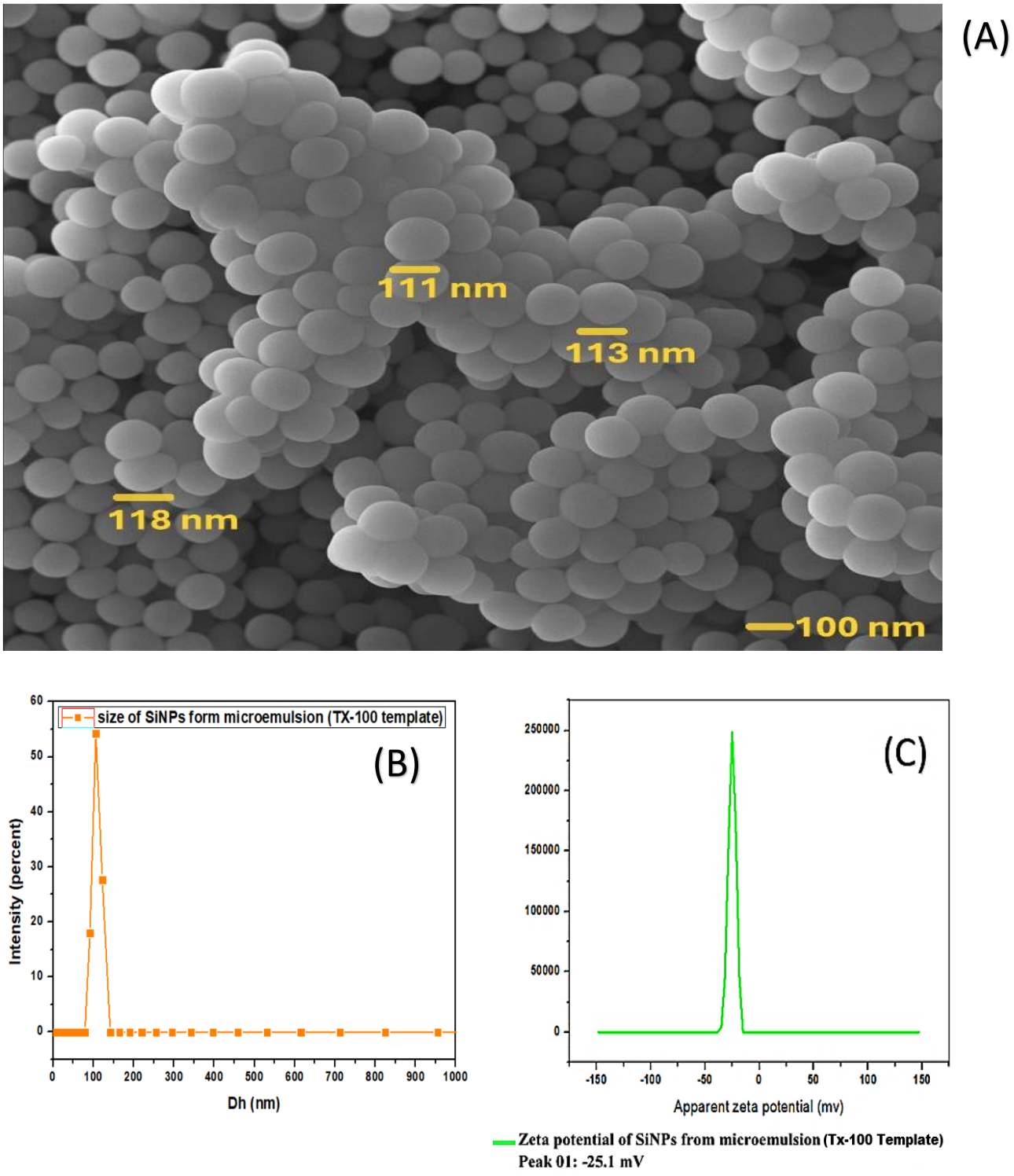

Figure III.13:(A) SEM image of SiNPS (TX-100 template); **(B)** hydrodynamic diameter distribution SiNPS (TX-100 template) (polydispersity index = 0.3); **(C)** zeta potentials of SiNPS (TX-100 template -25mV).

III.6.4 Energy-Dispersive X-ray Spectroscopy

Analysis of the EDS data **Figure III.14** of SiNPs via emulsion from CTAB surfactant reveals critical insights into the elemental composition and purity of the synthesized silica nanospheres. that the nanospheres have a significant presence of oxygen, While oxygen is an essential component of silica this high oxygen content suggest the presence of oxygen-rich species or potentially some surface oxidation . Silicon is also present but to a lesser extent, The presence of carbon suggests that there are significant carbon-based materials in our sample. This may be due to organic residues from the synthesis process or some form of surface contamination such as unreacted CTAB surfactant.

The EDS analysis of the synthesized silica nanospheres, produced via a emulsion method with TEOS as the precursor and TX-100 nonionic surfactant, has revealed their elemental composition. The data indicates a predominant presence of oxygen and silicon, consistent with the expected composition of silica. However, notably, a significant amount of carbon was detected in the nanospheres, despite rigorous washing procedures. This suggests the persistence of carbon-containing species, likely stemming from incomplete removal of organic contaminants or surfactant residues and possibly Some carbon species might have adsorbed strongly to the surface of the nanospheres during the synthesis process.

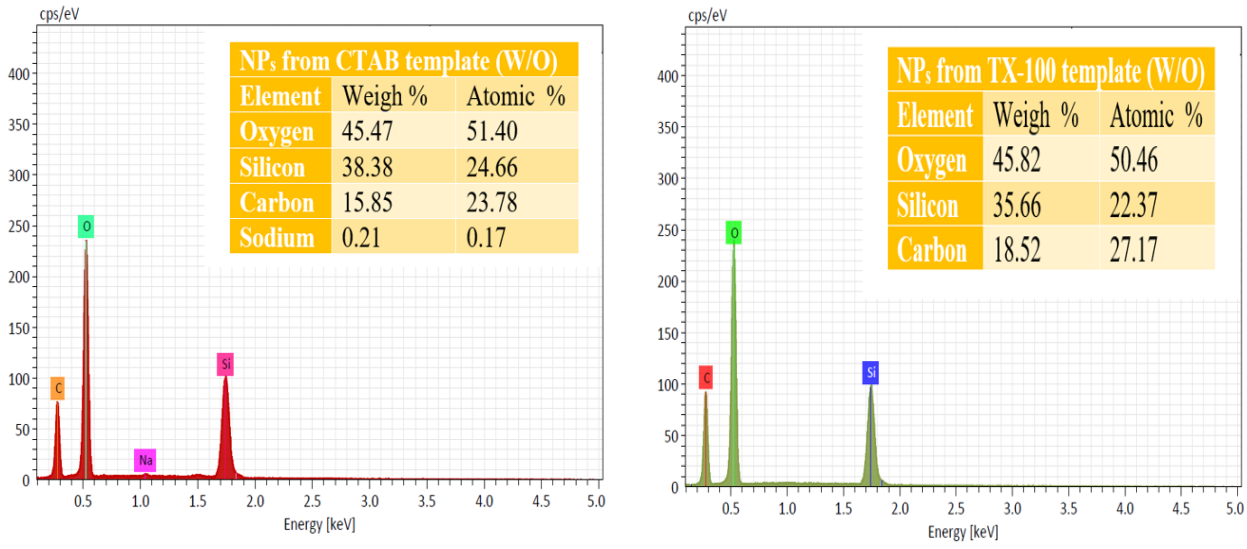

Figure III.14: The EDS analysis of SiNPs after calcination (From CTAB and TX-100 Templates) using Sol-Gel method in microemulsion .

- **ray diffraction (XRD)**

In the X-ray diffraction (XRD) analysis of silica nanoparticles synthesized through water-based and microemulsion methods using TX-100 and CTAB surfactants, distinctive patterns emerge, revealing insights into the crystalline structure and characteristics of the nanoparticles in each synthesis approach.

III.6.5 X-ray diffraction (XRD) SiNPs in water preparation

In the X-ray diffraction (XRD) analysis of silica nanoparticles synthesized via the sol-gel process using CTAB and TX-100 surfactants as templates in water preparation **Figure III.15 (A)** ,distinct crystalline patterns emerged, revealing noteworthy differences in crystallinity and morphology between the two templates. The sharp and intense peak at 2θ 21.70° (SiNPs from TX-100 template) indicates a well-crystallized silica phase, The sharpness suggests a high degree of crystallinity and Larger particles may result in sharper and more intense peaks ,Additional Peaks (19°, 28.22°, 31.17°, 35.87°) Small peaks at these angles may signify the presence of crystalline impurities could be from left over template or secondary phases introduced during synthesis or calcination like residual of NaOH base. Compared with (NPs from CTAB template) a peak at 21.70° also corresponds to a crystalline silica phase, but with lower intensity compared to the TX-100 template. The lower intensity suggests lower crystallinity or smaller crystallite size. SEM images **Figure III.15 (9,10)** further elucidated the structural variations, highlighting nanorod morphology in CTAB-synthesized nanoparticles and larger aggregate formations in those derived from TX-100, offering valuable insights into the templating effects on silica nanoparticle characteristics.

III.6.6 X-ray diffraction (XRD) SiNPs prepared by microemulsion process

The X-ray diffraction (XRD) analysis of silica nanoparticles prepared through the microemulsion process using TX-100 and CTAB surfactant **Figure III.15 (B)** reveals distinctive features in the presence and absence of procaine. Sample of SiNPs (TX-100) exhibit a SiO2 peak at 2θ of 21.70° and display a amorphous pattern with a broad hump at 21.70°. In contrast, The (XRD) analysis of silica nanoparticles prepared through the microemulsion process using CTAB surfactant **Figure III.15 (B)** reveals distinct patterns, the sample exhibit

a SiO2 peak at 2θ of 21.44°, indicating a crystalline phase. The silica nanoparticles SiNPs (CTAB) display another sharp peak at 21.61°, suggesting a different crystalline pattern.

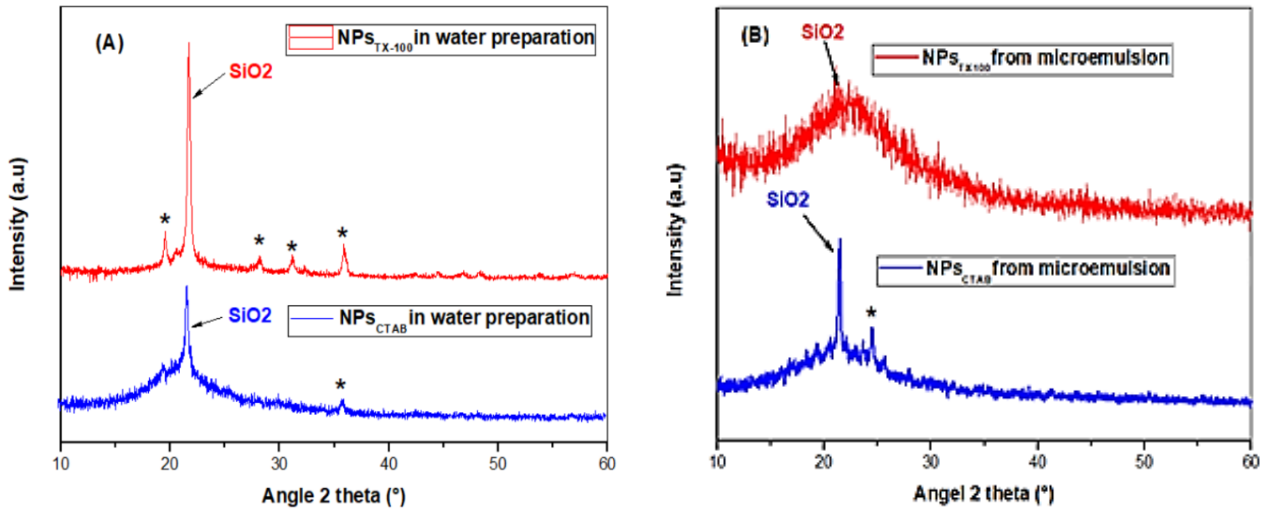

Figure III.15:XRD patterns of (A) silica nanoparticles synthesized through water-based using TX-100 and CTAB surfactants, (B) silica nanoparticles prepared through the microemulsion process using TX-100 and CTAB surfactants.

III.6.7 XPS Analysis

Comprehensive X-ray photoelectron spectroscopy (XPS) analysis facilitated the elucidation of the surface chemistry inherent to the synthesized silica nanoparticles (SiNPs). The survey spectra, as illustrated in **Figure III.16 a** and **17 a**, confirmed the elemental composition, predominantly showcasing peaks for silicon (Si), oxygen (O), and carbon (C). The high-resolution spectra for the silicon 2p orbital, detailed in Figures 09b and 10b, revealed binding energies at approximately 99.81 eV for CTAB-mediated SiNPs and 102 eV for TX-100-mediated SiNPs. These values are emblematic of the Si^{4+} oxidation state within the SiO_2 lattice, confirming the formation of the desired silica structure. [139][140]

In the O1s high-resolution spectra, shown in **Figure III.16 c** and **17 c**, the observed binding energies at 529.2 eV and 528.8 eV are characteristic of lattice oxygen in silicon dioxide, with additional spectral features potentially indicative of surface hydroxyl groups or physisorbed

water molecules. The latter are of particular relevance as they play a crucial role in the surface chemistry of SiNPs, influencing interactions with biomolecules and drugs for delivery applications.

The C1s spectra, presented in **Figure III.16 d** and **Figure III.17 d**, exhibit main peaks at 283 eV, with additional spectral features indicative of various hydrocarbon species. These are likely attributable to residual surfactants or adventitious carbon contamination, which are commonly observed in XPS analysis due to sample handling or preparation procedures. The presence of these carbon species suggests a heterogeneous surface composition, which could potentially affect the interaction dynamics of SiNPs with their cargo molecules.

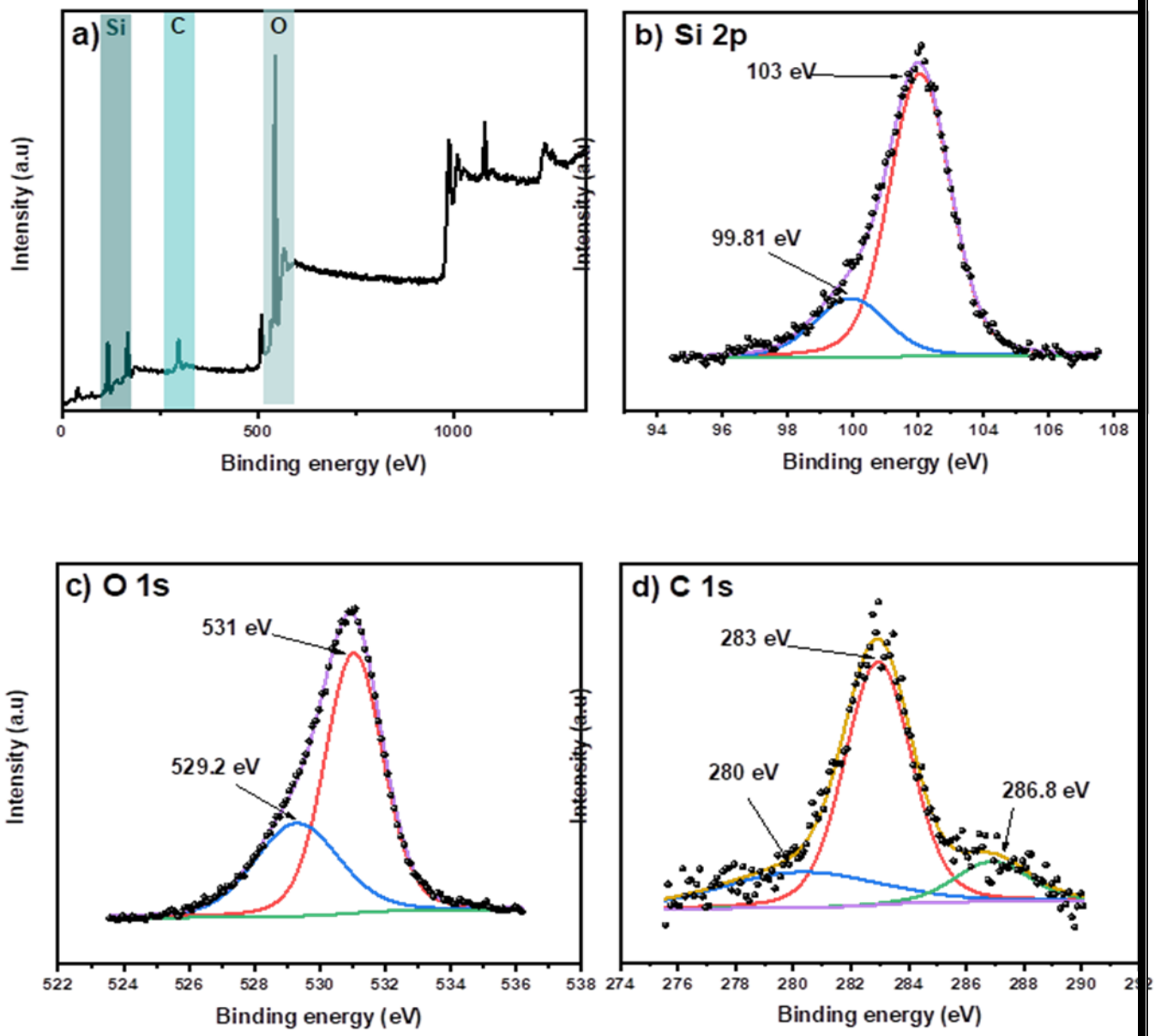

Figure III.16:XPS spectra of CTAB mediated silica nanoparticles in Water process. (a) survey (b) Si 2p, (c) O 1s, (d) C 1s,

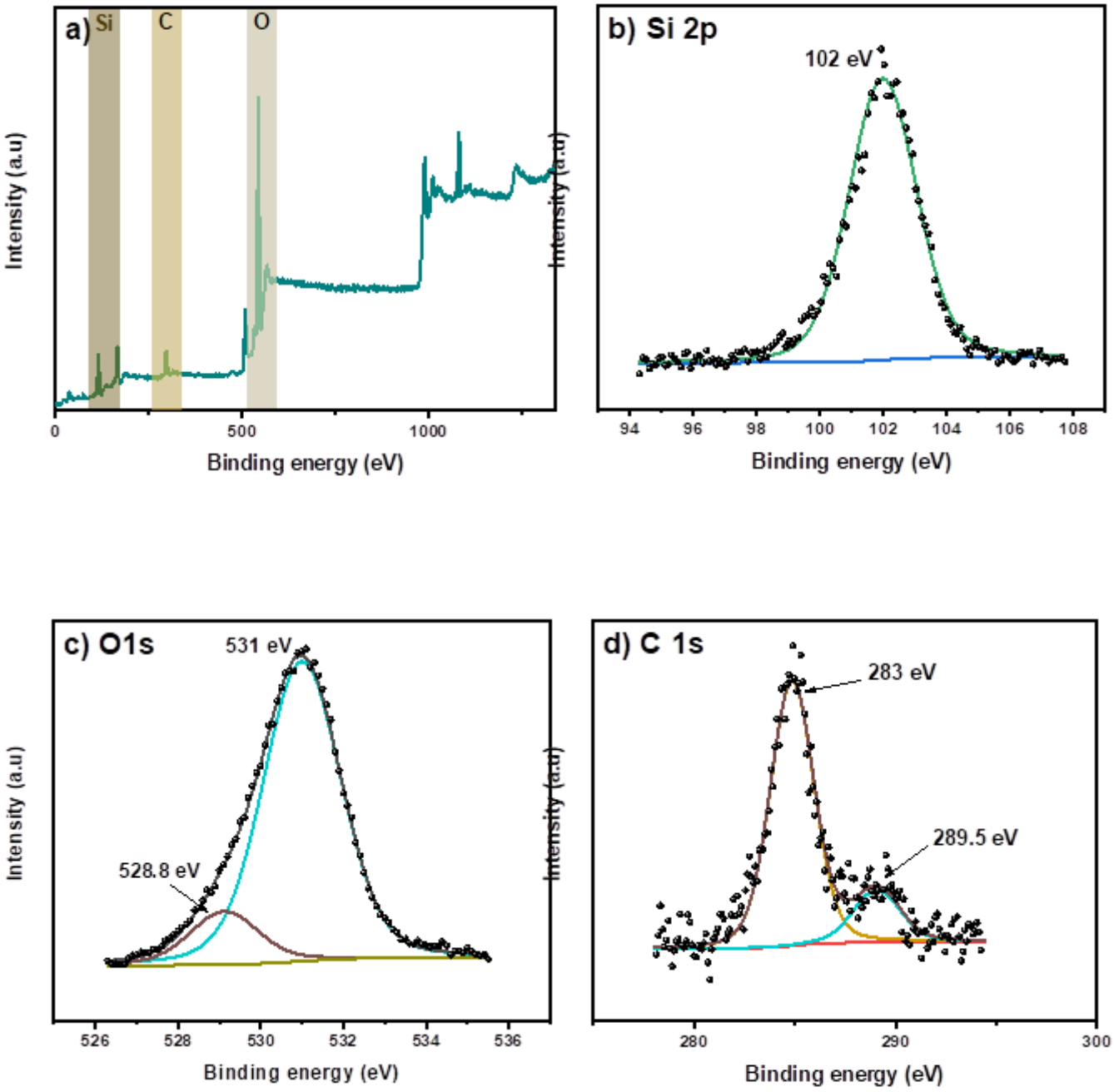

Figure III.17:XPS of TX-100 mediated silica nanoparticles in Water process. (a) survey (b) Si 2p, (c) O 1s, (d) C 1s.

IV. Chapter 04: Harnessing Silica Nanoparticles for Efficient Adsorption and Targeted Drug Delivery

IV.1 Introduction:

The dye industry causes very serious pollution for citizens and the environment, as they are chemicals that are harmful to health, such as certain carcinogenic dyes, which cause water pollution and require techniques to degrade them. Dyes are used in clothing, food, cosmetics, medicines, etc. In this context, the use of silica nanoparticles as adsorbents is of great interest due to their adsorption capacity and high specific surface area. The aim of our work is to monitor the removal of brilliant green and carmine by SiNPs. In the second stage of this chapter we will see the possibility of loading the PRC drug into these particles.

IV.2 Methods for removing dyes

Most colorants are very stable and cannot be easily biodegraded, which could lead to serious adverse environmental effects for human and aquatic organisms. Numerous studies have been carried out with the aim of limiting dye contamination. dye contamination. Various techniques (**Figure IV1**) have been used to remove soluble dyes from industrial or domestic effluents. They differ from one another and can be cited by way of illustration: adsorption, electrolysis, flotation, precipitation, ion exchange, liquid-liquid extraction, membrane filtration, etc....[141][142]

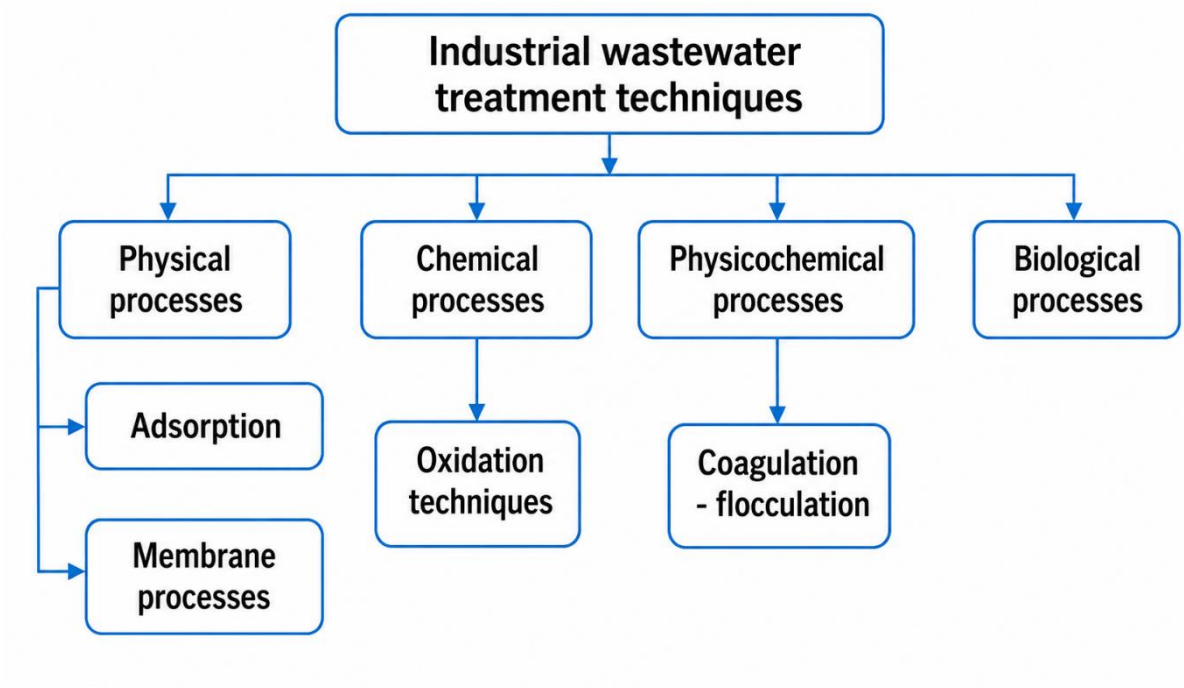

Figure IV.1: Wastewater treatment techniques.

Various studies have shown that adsorption is the most effective process for removing organic micropollutants. Adsorption is used in industrial processes for the separation and purification of gases and liquids, in a wide variety of fields such as petrochemicals, chemicals, pharmaceuticals and the environment. Industrial applications generally only use the physical adsorption properties of materials, as this phenomenon does not modify the molecular structure of the adsorbate. matériaux car ce phénomène ne modifie pas la structure moléculaire de l'adsorbat. De plus, il est réversible, ce qui permet de récupérer la molécule adsorbée et ainsi de régénérer l'adsorbant.

IV.2.1 Adsorption process

- **Definition**

L'adsorption est définie comme le passage d'espèces chimiques d'une phase liquide ou gazeuse vers une surface solide. Il s'agit donc du passage de l'état de dissous à celui d'adsorbé. Le processus inverse s'appelle la désorption. adsorbed. The reverse process is called desorption. This definition applies to all dissolved substances, whether ionized or not, and to all solid surfaces. Adsorption takes place in three main stages:

1. Diffusion of adsorbate from the outer liquid phase to the phase near the adsorbent surface.
2. Solute transfer through the liquid film to the grain surface.
3. Transfer of material in the porous structure from the outer surface of the grains to the active sites.

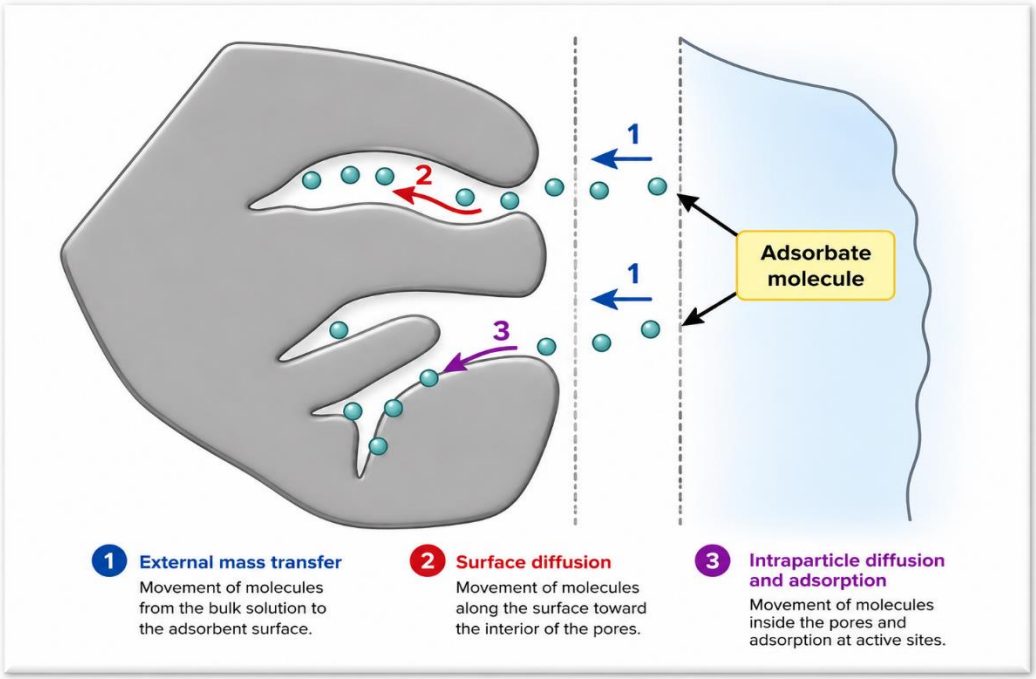

Figure IV.2: Domain of existence of a solute during adsorption on a microporous material [143]

IV.2.2 Different types of adsorption

Adsorption at the solute/solid interface is a physical or chemical phenomenon by which liquid or gaseous molecules attach themselves to the surface of a solid. This spontaneous phenomenon is due to the existence of adsorption sites on the solid surface. These sites generate forces. These forces lead to two types of adsorption:

- Chemical adsorption (Chimisorption)
- Physical adsorption (Physisorption)
- **Chemical adsorption (Chimisorption)**

Chemisorption is generally irreversible, producing a modification of the adsorbed molecules. These molecules cannot be accumulated on more than one monolayer. The only molecules concerned by this type of adsorption are those that are directly. Only molecules directly bound to a solid are concerned by this type of adsorption[144]**.** The heat of adsorption is relatively high, ranging between 40 and 200Kcal/mol[145], the distance between the surface and the adsorbed molecule is shorter than in the case of physisorption.

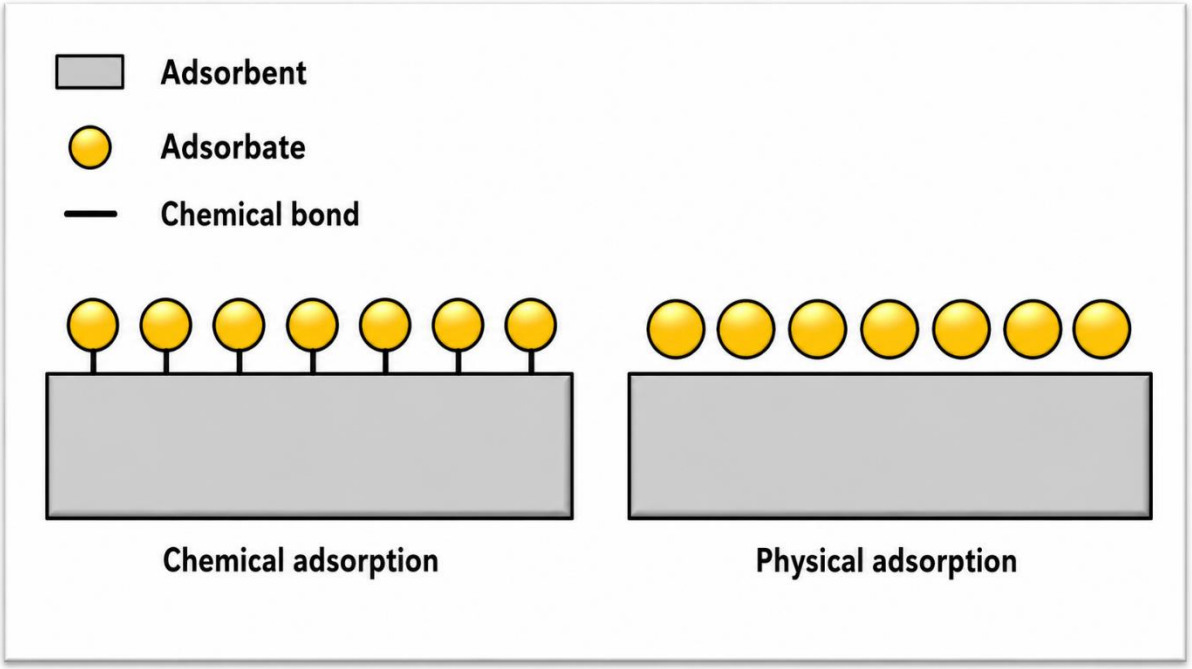

Figure IV.3: Schematic representation of physical and chemical adsorption

- **Physical adsorption (Physisorption)**

Physical adsorption (or physisorption) involves weak interactions such as Van Der Waals forces of attraction due to electrostatic depolarization interactions. Molecules adsorb onto several layers (multilayers) with heats of adsorption often below 40 Kcal/mol.[146] which is considered weak. These interactions are non-specific and reversible, and desorptioncan be total. Physical adsorption is rapid and generally limited by diffusion phenomena, and does not lead to modification of the adsorbed molecules. In fact, the energies involved in strong physisorptions are similar to those involved in weak chemisorptions.

IV.2.3 Criteria for distinguishing between physical and chemical adsorption

Experimentally, it is often possible to distinguish between the two types of adsorption; but, in some cases, it is necessary to examine several criteria simultaneously in order to reach a conclusion. The criteria for differentiating between these two adsorption modes are listed in **Tableau IV.1**

	Chemical adsorption	Physical adsorption
Nature of interactions	Strong bonds, high adsorbent/adsorbate affinity	Weak bonds (Van der Waals forces)
Quantity adsorbed	Determined by the number of surface sites (monolayer)	Possibility of superimposing several layers of adsorbed atoms (multilayers)
Heat adsorption	*> 50 kJ/mol*	*< 50 kJ/mol*
Adsorption speed	*slow*	fast
Reversibility of the phenomenon	Limited	Highly marked

Tableau IV.1: Differences between chemical and physical adsorption

IV.2.4 Parameters affecting adsorption

They can influence the adsorption process, and in particular retention capacity and kinetics. These include:

- **Porosity**

Porosity is linked to pore size distribution. It reflects the internal structure of microporous adsorbents. However, pore volume, specific surface area and pore size have a greater effect on adsorption.

- **Type of adsorbate**

Adsorption of a solute is strongly linked to the nature of the solute (molecule size, polarity, nature and position of its functional groups, presence of unsaturation, solubility). The size of the adsorbate molecules, which can greatly influence the adsorption process through their arrangement on the surface of the material.

- **Polarity**

A polar solute will have more affinity for a solvent or for the most polar adsorbent. Preferential adsorption of organic compounds with limited solubility in aqueous solutions (hydrocarbons, chlorine derivatives, phenol and other benzene derivatives) is important with hydrophobic adsorbents (activated carbons, porous polymers). On the other hand, it is insignificant with highly hydrophilic polar adsorbents (silica gel, alumina, etc.).

- **pH**

The pH of the solution has an effect on both the adsorbate and the adsorbent (functional groups). For compounds with a pKa close to the pH values studied, this parameter will have an effect on the adsorption capacity of these solutes.

- **Température**

Adsorption is an endothermic or exothermic phenomenon, depending on the adsorbent material and the nature of the adsorbed molecules. Numerous authors have noted the decrease in adsorption capacity of organic compounds as temperature rises. Higher temperatures lead to higher velocities (particularly for diffusion stages), but also to greater desorption, which in turn leads to a reduction in adsorption capacity.

IV.2.5 Some adsorbents used for pollutant removal

- **Activated carbon**

Activated carbon, also known as activated charcoal or activated carbon, is a material consisting essentially of carbonaceous material with a porous structure. Activated carbon is any carbon that has undergone special preparation and therefore possesses a high degree of ability to bind and retain certain molecules brought into contact with it. They are obtained by carbonizing a precursor at high temperature.

Figure IV.4: Activated carbon grain

- **The clays**

Clays, or argillaceous rocks, are a mixture of minerals and crystalline impurities. Clays are products of the decomposition of siliceous rocks, by physical and mechanical disintegration, followed by chemical alteration. Raw clay generally contains elementary particles with grain diameters of less than two micrometers (2μm), which represent the crystalline individuals (pure mineral phase) known as clay minerals, responsible for properties such as swelling, plasticity and adsorption properties.

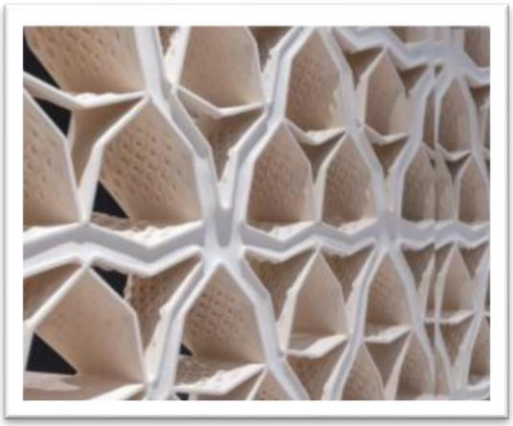

Figure IV.5:3D representation of clay

- **Zeolites**

They are hydrated silico aluminates in the crystalline state. These compounds have the property of slowly losing their water of crystallization on moderate heating, without changing their crystalline structure. They become spongy and highly adsorbent. Artificial zeolites exist, with very high adsorbing powers. They have the ability to bind heavy metal salts found in water.

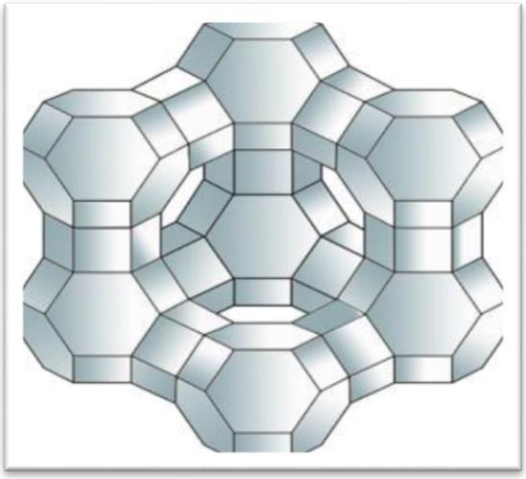

Figure IV.6: Schematic representation of a zeolite**[147]**

- **Silica-based nanoparticles**

Silica gels (SiO2, nH2O) are highly hydrophilic synthetic adsorbents with controllable porosity and a specific surface area of between 300 and 800 m2/g. Silicas are used to complex hydrocarbons, including halogens, and dyes. These characteristics show a highly porous texture and, consequently, a high adsorption capacity for this gel. Results show that adsorption can reach 80% of the total adsorption capacity.

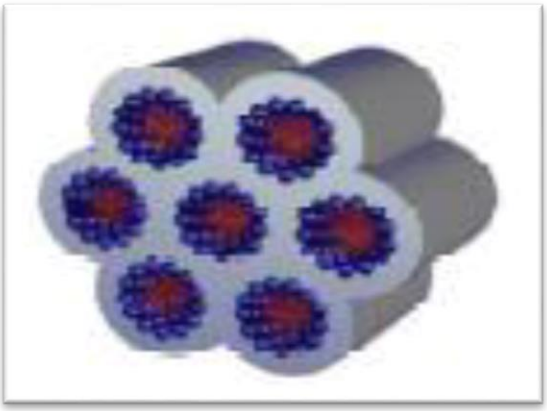

Figure IV.7: Schematic representation of a mesoporous silica-based nanoparticle

IV.3 Efficient Adsorption of Colorants Using Silica Nanoparticles

Silica nanoparticles (SiNPs) have garnered significant attention in various fields due to their high surface area, tunable pore size, and versatile surface chemistry. One common method

for synthesizing silica nanoparticles involves the use of surfactants as templating agents, which help control the particle size and morphology. In this study, cetyltrimethylammonium bromide (CTAB), a cationic surfactant, was employed as a template in the synthesis of silica nanoparticles. The resulting nanoparticles were further utilized as adsorbents for the removal of colorants, specifically bright green and carmine, from aqueous solutions.

The use of CTAB as a template is particularly advantageous due to its ability to form micelles in aqueous solutions, which act as nucleation sites for the formation of silica particles. This method enables the production of well-defined, monodisperse nanoparticles with a controlled pore structure, making them highly effective for adsorption applications.

Bright green and carmine are widely used synthetic colorants in various industries, including textiles, food, and cosmetics. However, their presence in wastewater poses environmental challenges due to their potential toxicity and persistence. Therefore, developing efficient adsorbents to remove these colorants from contaminated water is of great importance.

In this study, the adsorption capabilities of the synthesized silica nanoparticles were evaluated by testing their efficiency in removing bright green and carmine from aqueous solutions. The results offer insights into the potential application of these nanoparticles in water treatment processes, contributing to the broader efforts of developing sustainable and effective methods for pollutant removal. To achieve this objective, we used two characterization techniques: UV visible spectrophotometry and light scattering (DLS).

IV.3.1 Food colorants

- **Carmine (C.I. 75470)**

Water-insoluble natural colorant. It is obtained from dried female cochineal beetles. The main component is carminic acid. For microscopic staining, carmine is used in combination with an alum, usually aluminum-based. The result is a calcium-aluminum carminic acid lacquer with high coloring power.

Its chemical structure is shown in **Figure IV.8** and **Figure IV.9**, and its characteristics are listed in **Tableau IV.2**

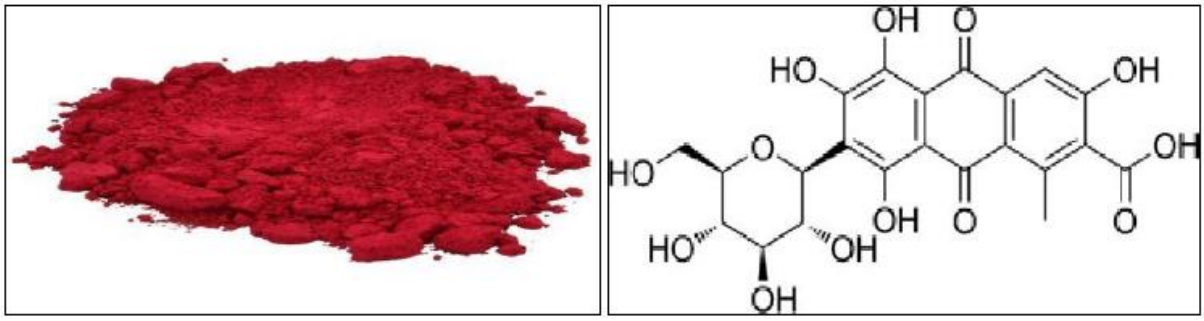

Figure IV.8: Chemical structure of carmine**[148]**

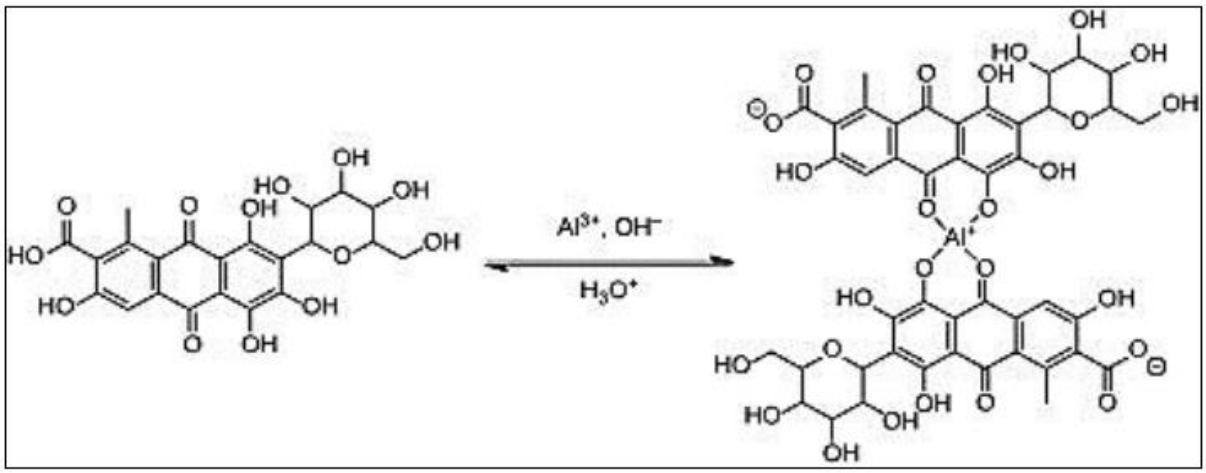

Figure IV.9: Reversible formation of aluminium carminic acid complexes**[149]**

Carminic acid and its derivatives are present in a wide range of foods such as ice creams, confectionery, culinary products, desserts, beverages, dairy products and others. Carmine is also widely used in cosmetics.[149]

Carmine	
common name	Carmine
chemical formula	$C_{22}H_{20}O_{13}$
molecular weight	492,4 g/mol
solubility in water	0,599 g/l
λmax (nm)	521
I.C.	C.I. 75470

Tableau IV.2: Physical and chemical properties of Carmine

- **Toxicity**

Although it is natural and poses no significant risk to human health or the environment, we are including it on this list for ethical reasons. Carmine is a natural red dye used in many consumer goods, including food, cosmetics and make-up.cosmetics and make-up because of its bright red hue. There is also evidence that carmine can cause allergic reactions.

- **Green shine**

Brilliant green (Figure IV9) is an odorless cationic dye. It is used in a number of fields, such as biological staining, dermatology and textiles, and for the confirmation of coliforms and thermotolerant coliforms in food products, feed water and waste water. for confirmation of coliforms and thermotolerant coliforms in food products, feed water and wastewater. It can also be used as a medium for coliform enumeration in ice cream[150]. Brilliant green has a number of effects on human beings, including gastrointestinal irritation, nausea, vomiting and skin irritation...etc. Its chemical structure is shown in **Figure IV.10**and its characteristics are listed in the **Tableau IV.3.**[151][152]

Figure IV.10: Chemical structure of brilliant green**[153]**

Green shine	
Nom Usuel	Green shine
Common name	C27H34N2O4S
Molecular mass	482.63 g.mol-1
Solubility in water	High
λmax (nm)	625
PKa	2.62 - 4.93
I.C.	42040

Tableau IV.3: Physical and chemical properties of Carmine

- **Toxicity**

Brilliant green causes several adverse effects in humans, including gastrointestinal irritation, nausea, vomiting and skin irritation. Several studies have been carried out on the elimination of brilliant green[154].

IV.4 Synthesis and characterization of NPS

IV.4.1 Preparation of nanoparticles

SiNPS silica nanoparticles were synthesized by the direct precipitation method in the following steps:

Synthesis is performed using a micellar solution of CTAB surfactant in water, to which the silica source (TEOS) is added dropwise.The resulting mixture is left to stir (300 rpm) for one hour at controlled temperature using an oil bath. After 30 min of stirring, the soda used as a catalyst for the TEOS hydrolysis condensation reaction is added to the mixture, which is left to stir overnight. The nanoparticles are separated from the reaction medium by adding an equal volume of ethanol and centrifuging. Once the supernatant has been removed, the NPS are washed with ethanol before being left to dry. A white powder is obtained after drying at T1=70°C for 24 hours. To liberate the pores, the samples are calcined in a muffle furnace to T2= 500°C, then held at this temperature for t= 4 h. After calcination, the samples are stored in closed vials until analysis.

IV.4.2 Characterization of nanoparticles (SiNPS) by DLS

Controlling the structure of SiNPS materials requires taking into account the structuring agent (surfactant) CTAB and its properties in water as parameters for predicting nanoparticle

characteristics. For the chosen concentration of CTAB, two types of structure were obtained by light scattering, as shown in **Figure IV.11a and 11b**. A spherical size of 2nm and a cylindrical size of 100nm are obtained. The size of the nanoparticles depends on the size of the micellar structures used as templates.

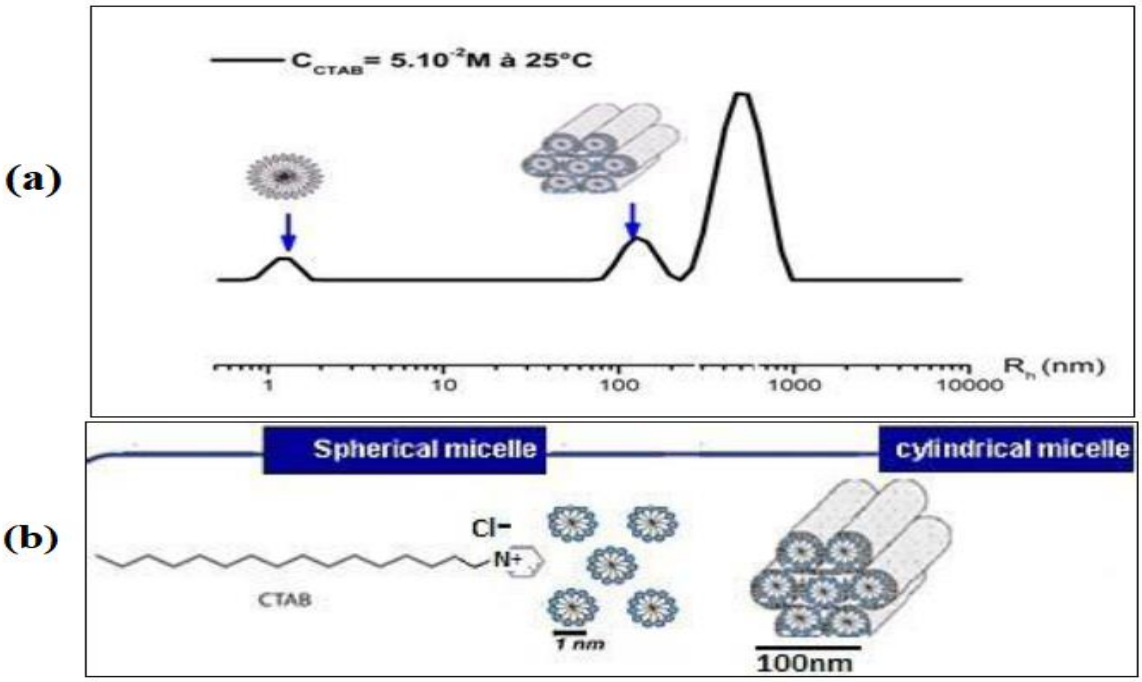

Figure IV.11:a) Size distribution and intensity for CTAB b): Molecular structures of the quaternary ammonium surfactant CTAB and its corresponding supramolecular assemblies (spherical and cylindrical micelles, respectively) formed in the presence of water

- **Effect of dilution**

Figure IV7 shows the curves obtained by DLS for solutions with different powder NPS concentrations at 25°C. According to the results obtained by DLS concerning the size distribution in intensity, all three curves show the presence of a single peak centered at around 100 nm hydrodynamic diameter. This indicates that our nanoparticle has a homogeneous monodisperse size, unaffected by dilution.

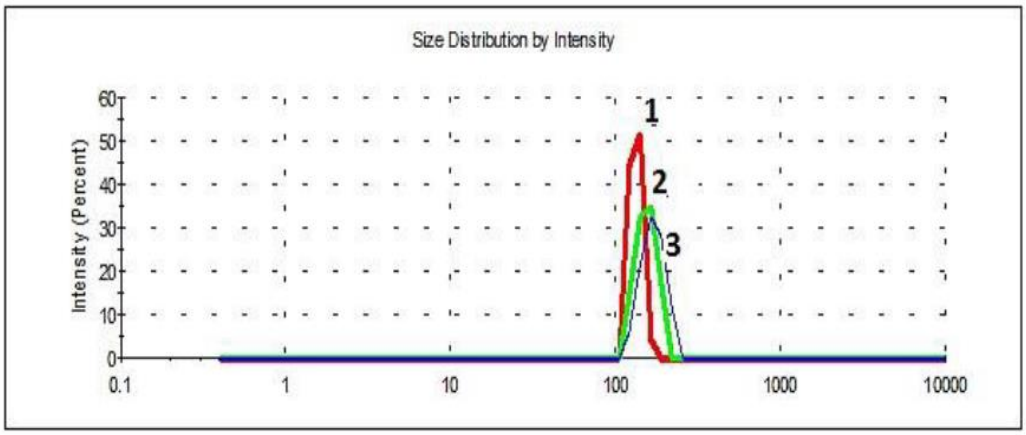

Figure IV.12: Intensity size distribution for the NPS nanoparticle powder for different concentration

- **Effect of calcination**

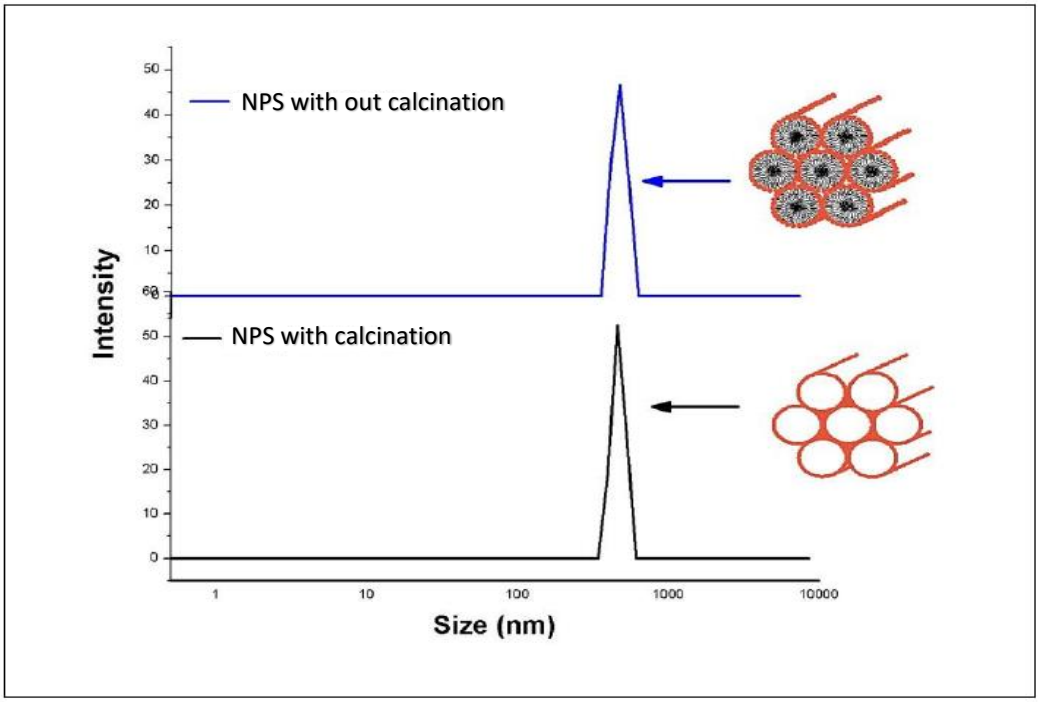

Figure IV.13: Size distribution in intensity for NPS without and with calcination.

In order to study nanoparticle size before and after calcination, DLS measurements were carried out. The results presented in **Figure IV.13** show that the nanoparticle retained its size after calcination.

IV.5 Colorants

IV.5.1 Absorbance measurement

Due to the chemical functions found in the chemical structure of the various dyes, they exhibit characteristic absorption spectra in the ultraviolet spectral range, between 400 and 800 nm, as shown in **Figure IV.14**. These spectra clearly show the wavelength of the Carmine absorption maximum at λmax=521nm and that of the bright green at λmax =625nm.

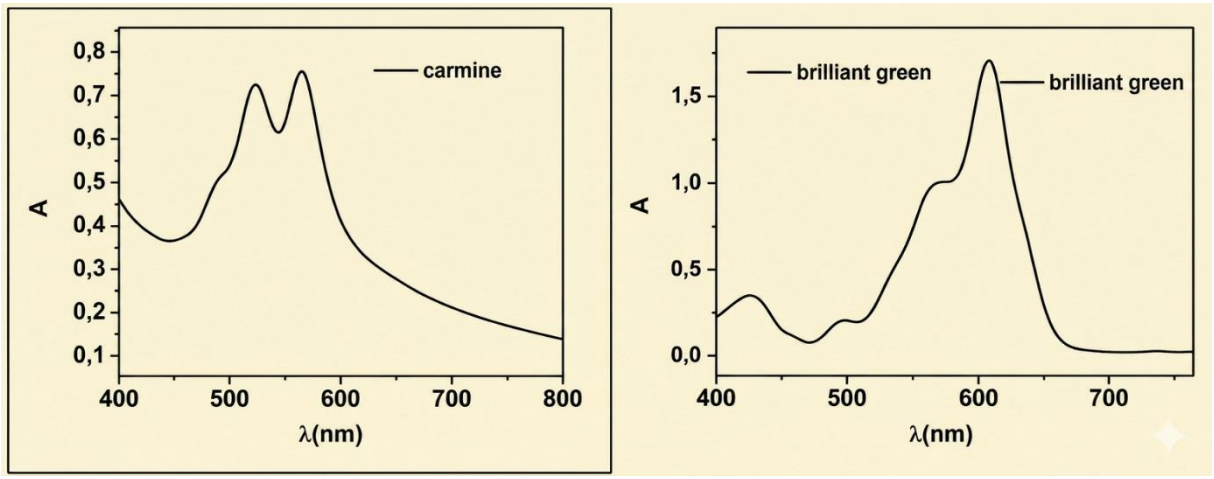

Figure IV.14: Variation in absorbance as a function of wavelength for the two dyes (Carmine and Brilliant Green)

- **Concentration effect and calibration curve**

Figure IV.15 shows the variation of absorbance A as a function of λ at different dye concentrations. In order to verify the application of Bert Lambert's law and its limits, the curve of variation of absorbance as a function of concentration was plotted for the maximum wavelength in **Figure IV.16.**

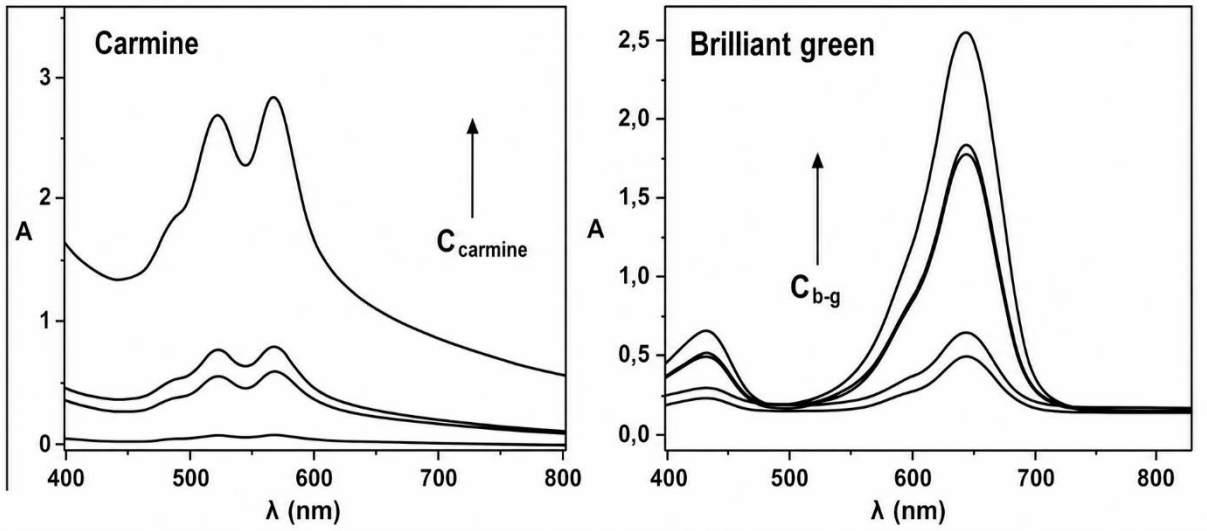

Figure IV.15: Carmine absorption spectra as a function of wavelength at different concentrations at 25°C for both dyes

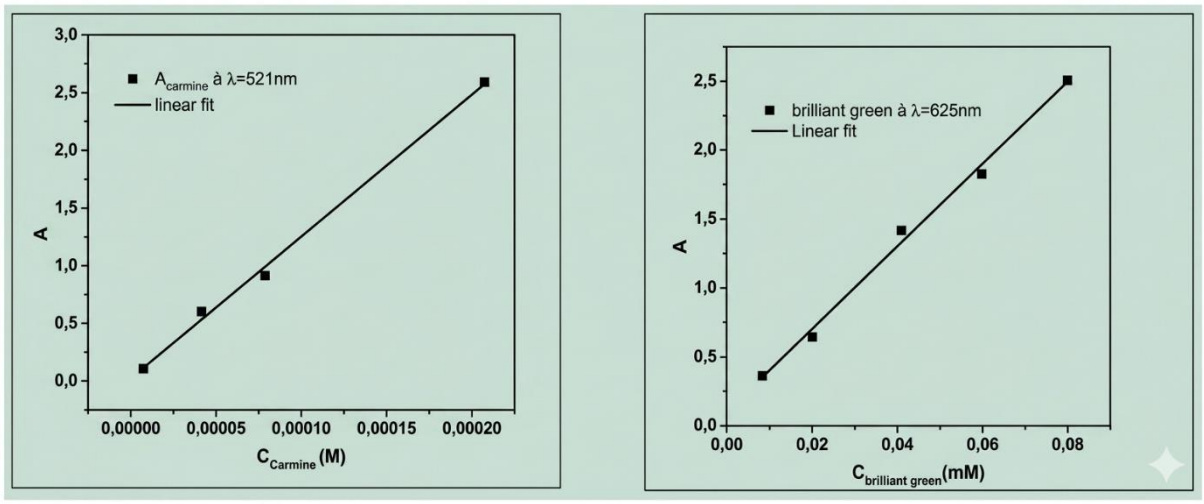

Figure IV.16: Calibration curve (Beer Lambert) for both dyes (Carmine and Brilliant Green)

In order to verify the application of Beer Lambert's law, curves of absorbance versus concentration were plotted for the maximum wavelengths recorded. The linear curves obtained for both dyes show that the law is verified in the concentration range studied.

- **pH effect**

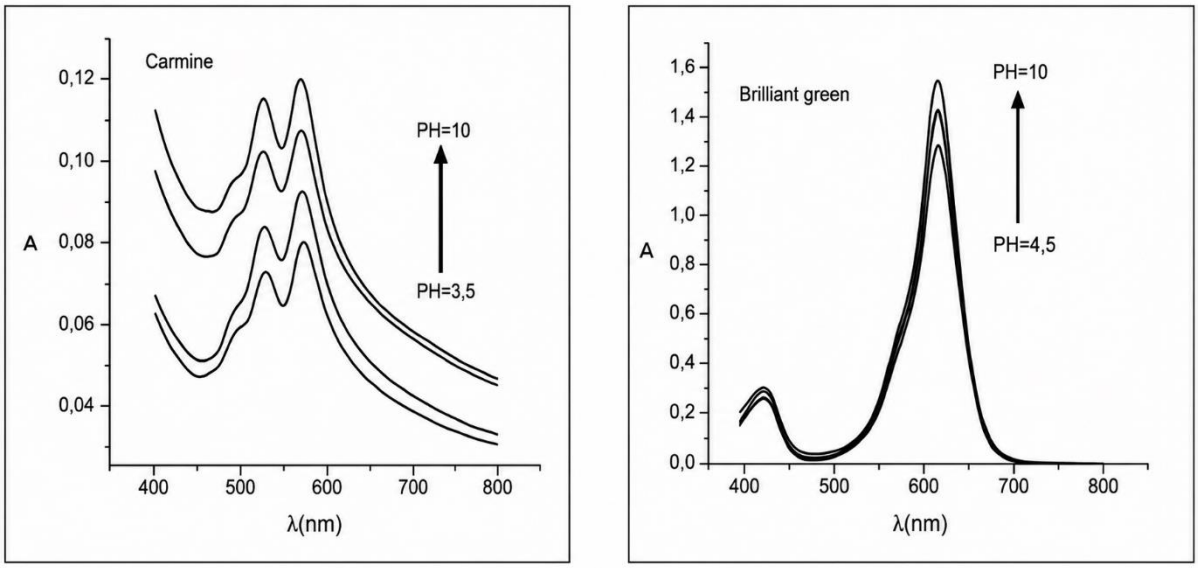

Figure IV.17: Bright Green Carmine absorption spectra as a function of wavelength at different pH levels at 25°C.

IV.6 Study of Carmine and brilliant green adsorption on NPS nanoparticles

IV.6.1 Introduction

The aim of this section is to study the influence of physicochemical parameters such as contact time, initial dye concentration, adsorbent mass and the effect of agitation on adsorption by calcined SiNPS.

IV.6.2 Description of the experimental set-up

Dye adsorption experiments are carried out by bringing a quantity of nanomaterial (SiNPS) into contact with the dye solution without stirring. Then, in a 50 mL Erlenmeyer flask, the solution is stirred with a magnetic stirrer to homogenize the solid-liquid mixture. Adsorption is carried out at room temperature (25 ± 1°C). At the end of the tests, the samples are filtered and then analyzed by UV-visible spectrophotometry. The influence of various parameters (calcined nanoparticle concentration, contact time, agitation and temperature) on the adsorption capacity of the calcined nanoparticle was studied.

IV.6.3 Study of NPS by UV-visible

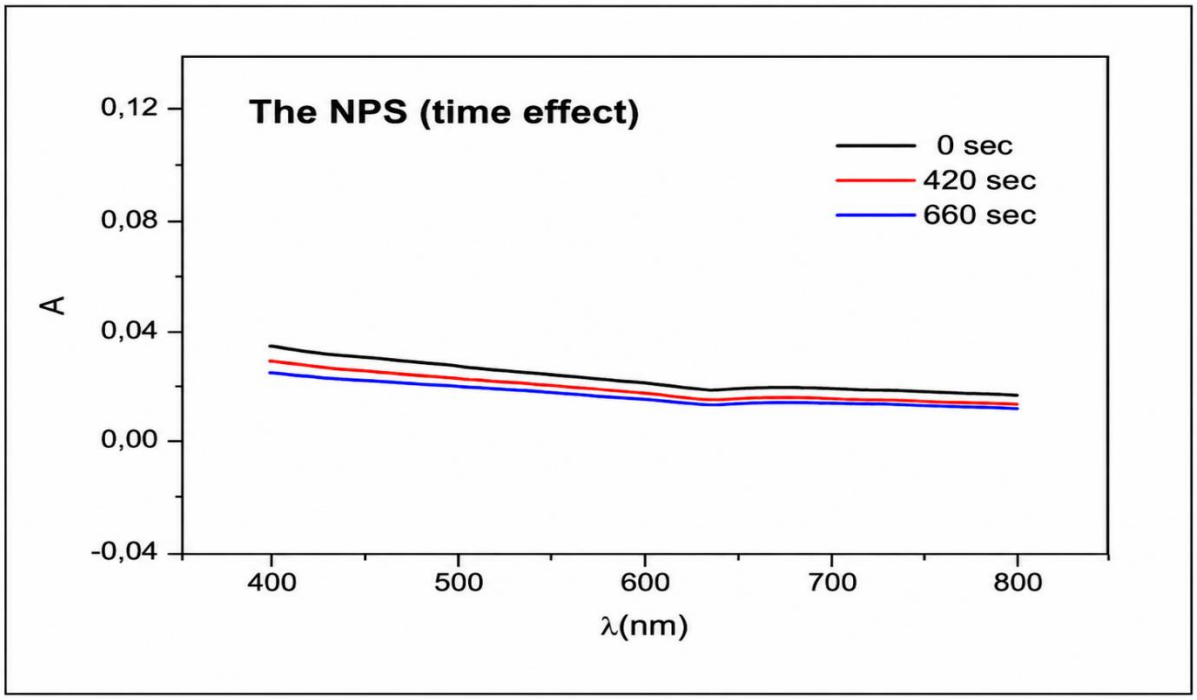

Figure IV.18: absorbance (A) of NPS as a function of wavelength at T~25°C for different contact times.

Figure IV.18 shows the kinetics of NPS absorbance (A) versus length at T~25°C. The pattern found indicates that our nanoparticle the NPS does not absorb in this studied range of λ.

IV.6.4 Study of adsorption kinetics

In order to study the effectiveness of the nanoparticle (NPS) and its ability to remove the two dyes, we carried out adsorption of the dyes with different masses of NPS. Tests were carried out in two modes:

Firstly, the adsorption of the different mixtures without stirring was monitored as a function of time using UV spectrophotometry. In the second, the mixture was placed under magnetic stirring, followed by sampling at different time intervals until equilibrium was reached. After filtration, the residual dye concentration was determined by UV spectrophotometry.

Mass effect of NPS

With out agitation

Carmine+0.5mgNPS

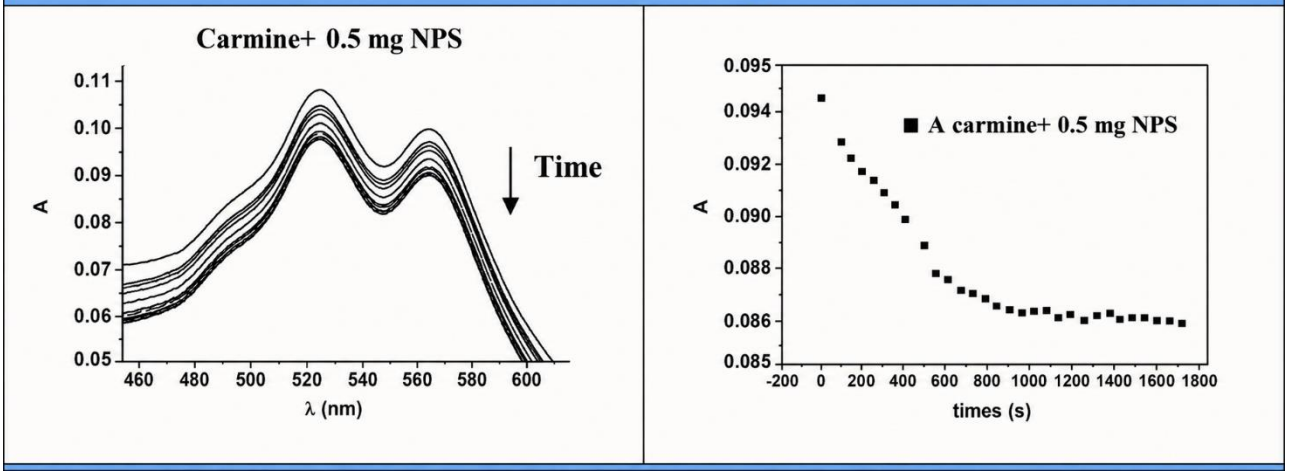

carmine +1mg NPS

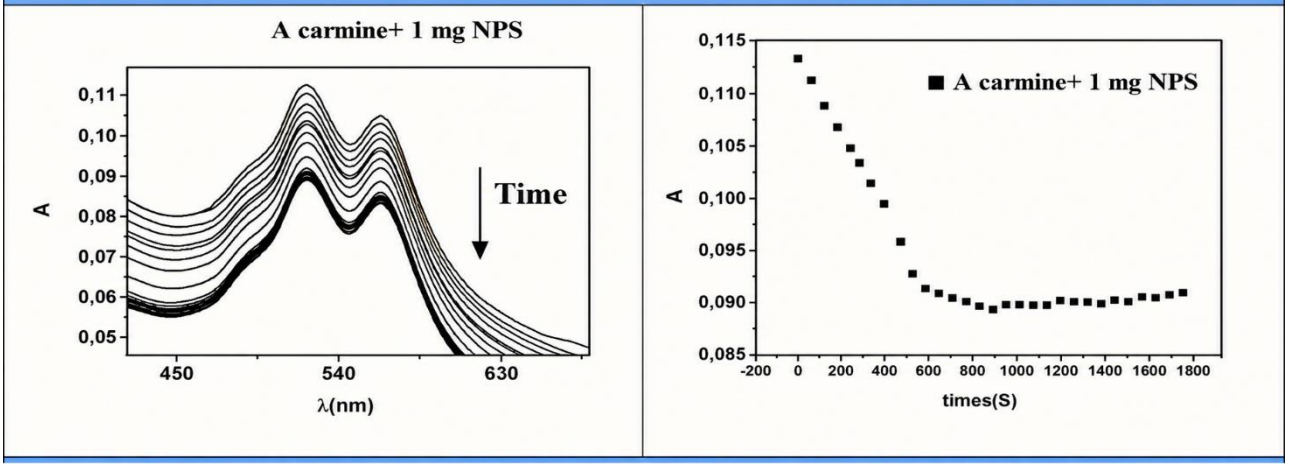

Carmine +1,5mg NPS

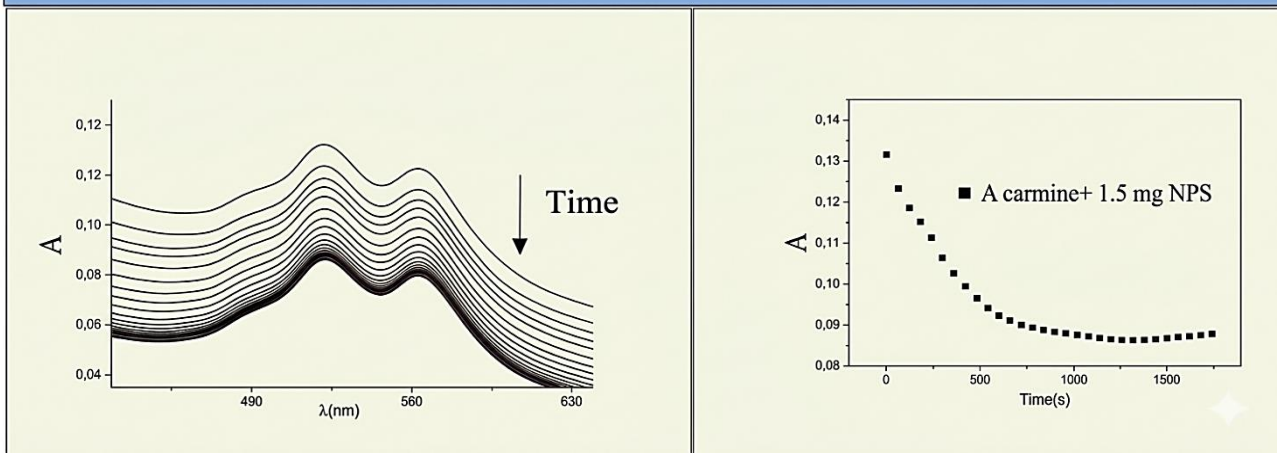

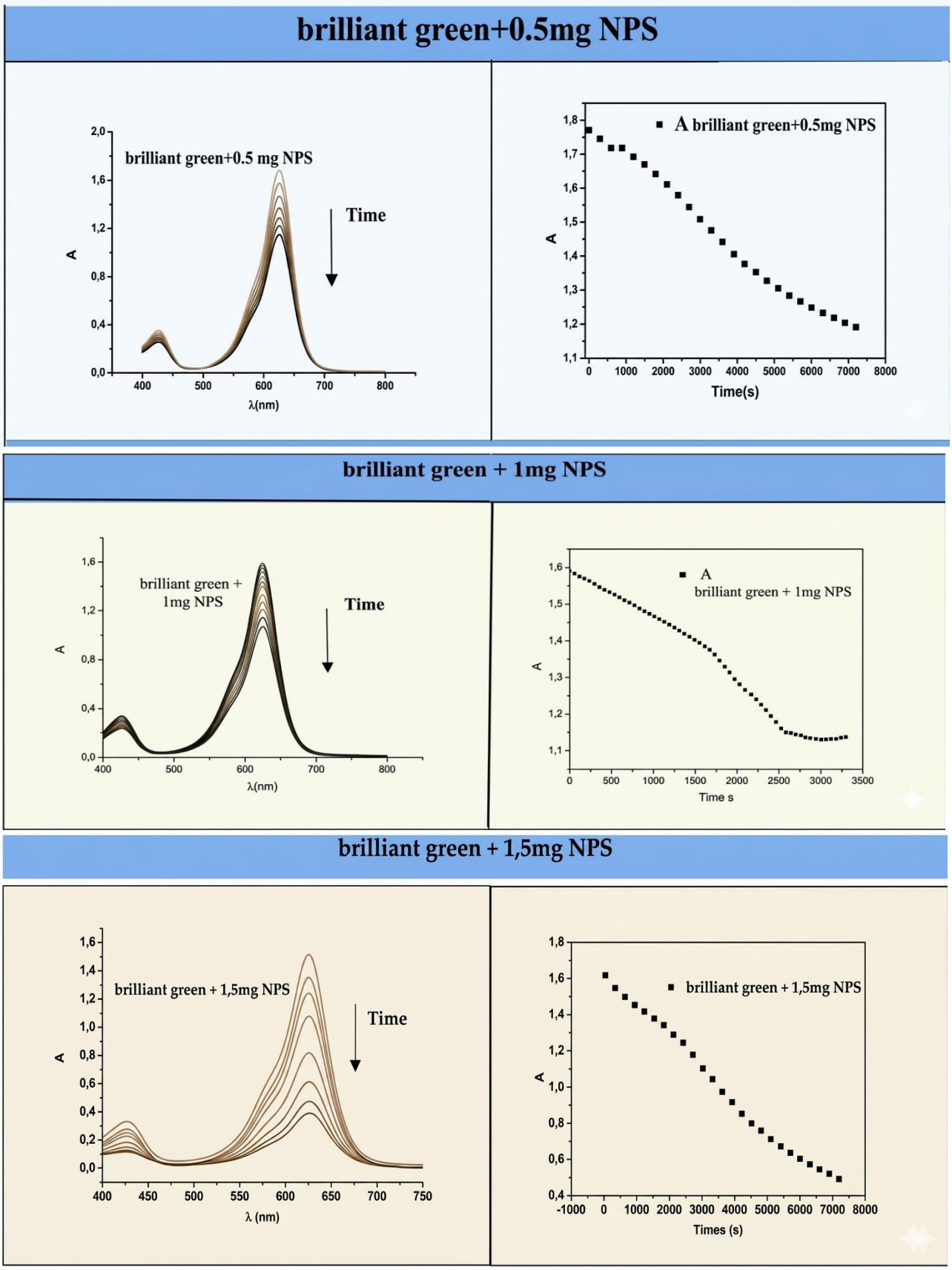

Figure IV.19: Influence of nanoparticle mass (NPS) on the adsorption of the two dyes Carmine and Brilliant Green (BG) as a function of time without agitation

Figure IV.19 shows rapid adsorption during the first 5 minutes for Carmine and 1h for VB. Thereafter, adsorption tends to level off. The rapid initial increase in adsorption is due to the instant availability of a large surface area and the presence of free sites on it. The slowdown in kinetics at the plateau may be due to the saturation of sites on the nanoparticle surface. In the light of these results, we can conclude that the equilibrium time is t=15min for Carmine and t= 45min for VB.

In the case of Carmine adsorption, we note from the graphs that NPS with Carmine show faster adsorption kinetics than with VB. In the case of VB, adsorption kinetics are relatively slow and the quantities adsorbed are greater.

IV.6.5 The effect of agitation

The effect of stirring speed on the adsorption of Carmine dye and VB is shown in **Figure IV.20:**

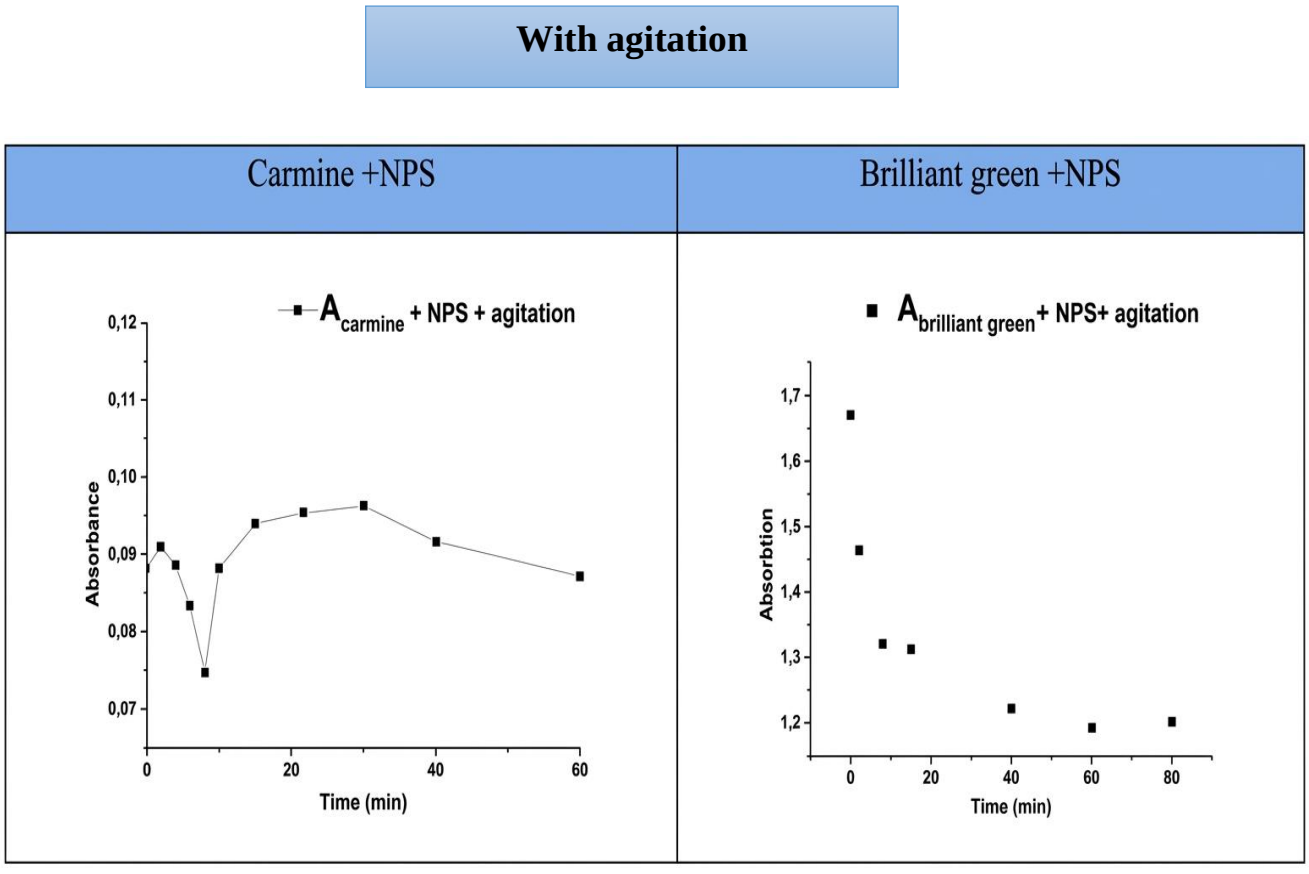

Figure IV.20: Effect of agitation on the adsorption of the two dyes Carmine and Brilliant Green (VB) by the nanoparticle (NPS) as a function of time

Figure IV.15 shows that in the case of adsorption of VB adsorption, we can see that the adsorption capacity of NPS increases as we increase the stirring speed, reaching equilibrium around the first 10 minutes. In this case, the effect of agitation on the increase in VB adsorption can be explained by the increase in electrostatic attraction between the negatively charged NPS and the positively charged VB dye (cationic dye).

In the case of Carmine, on the other hand, agitation causes desorption after the first 10 minutes. This can be explained by the fact that high agitation speeds break the adsorption forces in the pores, preventing Carmine from diffusing properly into the NPS.

IV.6.6 Temperature effect on adsorption

The effect of solution temperature on the adsorption of the dyes Carmine and VB is shown in **Figure IV.21**.

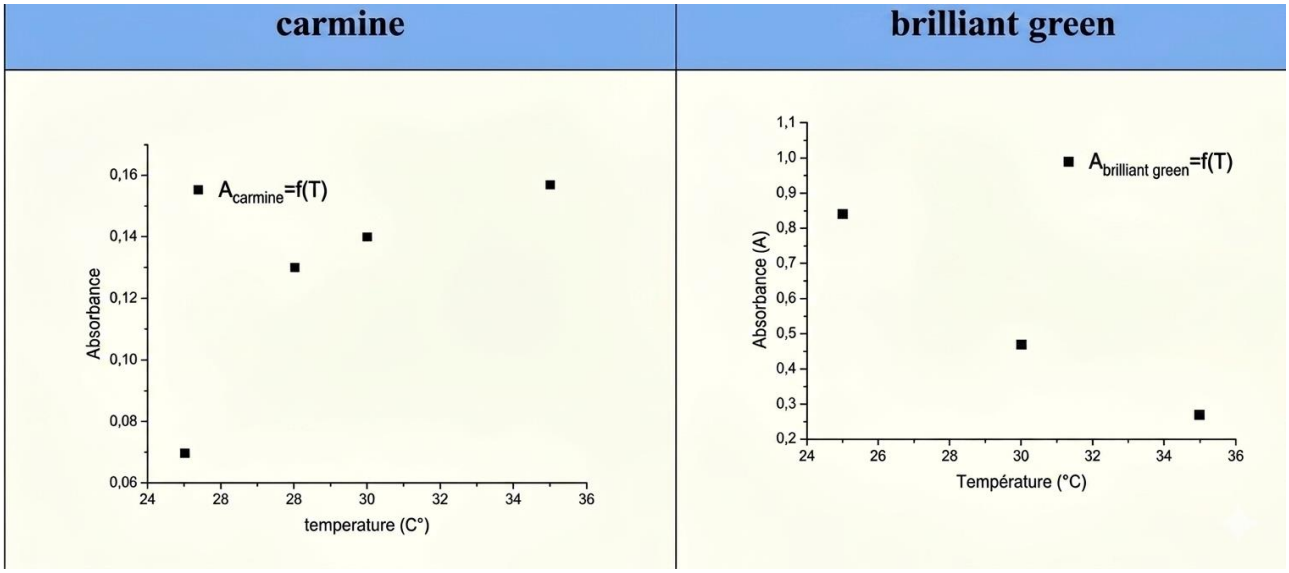

Figure IV.21: evolution of adsorption of the two dyes by NPS as a function of temperature

Figure IV.21 shows that carmine adsorption is favored by increasing temperature. This can be explained by the fact that temperature stabilizes the physical attractive forces involved. For VB adsorption, the adsorption capacity decreases with increasing temperature. These results show that the adsorption reaction can be exothermic, and that increasing temperature induces an

increase in the mobility of the dye particles in solution, and a decrease in the forces of dye attraction or diffusion on the active surface of the nanoparticles.

IV.7 Impregnation of Procaine Anesthesia Drug in SiNPs

IV.7.1 Introduction

Silica nanoparticles (SiNPs) have emerged as a versatile platform for drug delivery due to their high surface area, tunable porosity, biocompatibility, and ease of surface modification. The impregnation of drugs into SiNPs involves the incorporation of therapeutic molecules within the nanoparticle structure like Procaine, either through physical adsorption, covalent bonding, or encapsulation within mesoporous or solid silica frameworks. This approach enhances drug stability, improves solubility, and allows for controlled and sustained drug release, thereby improving therapeutic efficacy while minimizing side effects.

Mesoporous SiNPs (MSNs) are particularly attractive for drug loading due to their well-defined pore structure, which enables the efficient encapsulation of hydrophobic and hydrophilic drugs. The impregnation process is influenced by factors such as surface chemistry, pore size, drug-polymer interactions, and the physicochemical properties of the drug. Various loading techniques, including solvent evaporation, impregnation from solution, and covalent functionalization, have been explored to optimize drug loading and release kinetics. In this work we will study the possibility of loading the drug procaine in SiNPs and we will confirm this through different analysis devices.

IV.7.2 Comparison between X-ray diffraction of SiNPs loaded and free of Procaine (PRC) prepared by microemulsion process

- **XRD analysis of SiNPs (TX-100) loaded and free of PRC**

The X-ray diffraction (XRD) analysis of silica nanoparticles prepared via the microemulsion process using the TX-100 surfactant **Figure IV.22 (c)** reveals distinct features both with and without procaine. Both samples exhibit a SiO2 peak at $2\theta = 21.70°$.65 However, when procaine is loaded onto the nanoparticles, the XRD pattern shows additional small sharp peaks at 14°, 28.39°, and 35.78°, suggesting potential interactions or structural changes induced by procaine.

These differences in the XRD patterns indicate that the presence of procaine affects the crystallinity of the silica nanoparticles during the microemulsion synthesis process.

- **XRD analysis of SiNPs (CTAB) loaded and free of PRC**

The X-ray diffraction (XRD) analysis of SiNPs prepared via the microemulsion process using the CTAB surfactant **Figure IV.22 (d)** reveals distinct patterns in the presence and absence of procaine. Both samples show a SiO_2 peak at $2\theta = 21.44°$, indicating a crystalline phase. However, when procaine is loaded onto the nanoparticles, the XRD pattern shows a sharp peak at 21.44° with lower intensity. Additionally, small sharp peaks appear at 16.32°, 19.45°, 24.57°, and 25.61° in the procaine-loaded sample, suggesting potential interactions or the presence of crystalline impurities. In contrast, SiNPs without procaine display a sharp peak at 21.61° and a very low-intensity peak at 24.49°, indicating a different crystalline pattern. These observed differences in XRD patterns suggest that procaine may influence the crystallinity of the silica nanoparticles, possibly due to interactions or templating effects during the microemulsion synthesis process.

The well-defined broad and sharp diffraction planes at $2\theta = 21.44°$ and 21.70° for CTAB and TX-100-mediated particles indicate the presence of SiNPs across all synthesized materials. However, a broader diffraction angle (2θ) spanning a range of 20°-25° reveals a mesoporous amorphous nature, characterized by Miller indices of d (100). The broadness of the peak suggests the possibility of indexing to the hexagonal phase of mesoporous silica nanoparticles. This broadening indicates decreased crystallinity, reinforcing the amorphous character.[102],[155] These findings are consistent with previous studies by Sharma et al.[139] and Sarawade et al.[156], supporting the notion of comparable outcomes in the produced SiNPs. Additionally, slight variations in the 2θ range of diffraction peaks among mesoporous SiNPs synthesized with different chemical and surfactant compositions may be attributed to variations in the production quantities of SiNPs.[139]

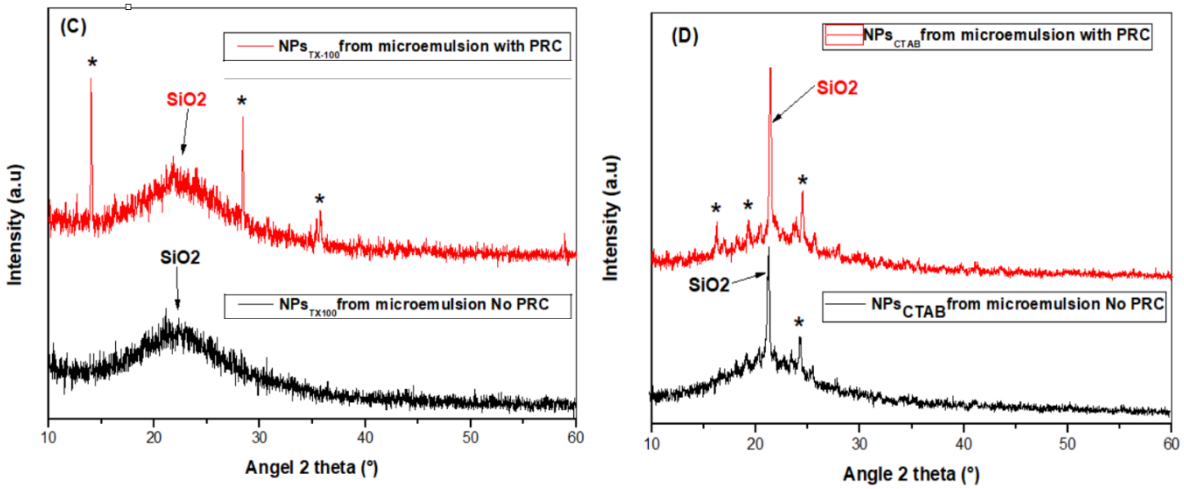

Figure IV.22:(C) Comparison between SiNPs prepared through the microemulsion process using TX-100 surfactant loaded and free of PRC and (D) Comparison between SiNPs prepared through the microemulsion process using CTAB surfactant loaded and free of PRC.

- **XPS Analysis**

Upon functionalization with procaine, the N1s peak around 402 eV (**Figure IV.23 d** and **Figure IV.24 d**) confirms the successful integration of the anesthetic. This peak is characteristic of nitrogen atoms in organic amine functionalities, a group present in procaine. The integration of procaine into the SiNPs is further supported by changes in the O1s and C1s spectra (**Figure 4.23 c, e and 24 c, e)**, suggesting the formation of new chemical environments around these elements, possibly due to the formation of Si-O-C linkages or the adsorption of procaine onto the nanoparticle surface.

A comparative assessment of the XPS data from CTAB- and TX-100-mediated SiNPs, both with and without procaine, underscores the nuanced influence of the surfactant environment on the surface chemistry of SiNPs. The slight differences in binding energies and peak shapes in the O1s and C1s regions between the two surfactant-mediated systems suggest variations in surface-bound species and the degree of organic residue. The introduction of procaine clearly alters the surface electronic environment, as evidenced by the N1s signals and the associated changes in the oxygen and carbon regions, which could significantly impact the drug loading capacity and release kinetics of the SiNPs.

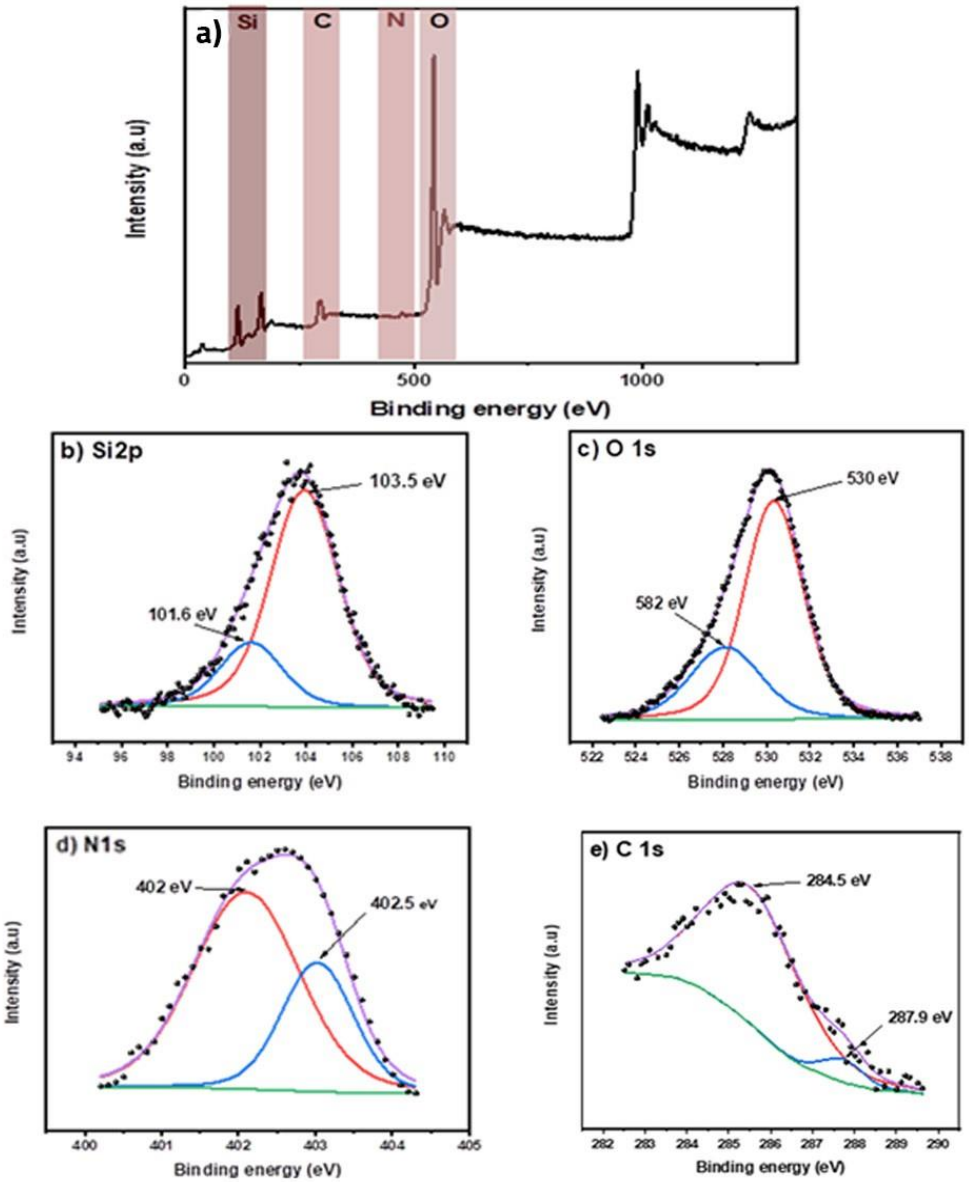

Figure IV.23: XPS spectra of CTAB mediated silica nanoparticles by microemulsion with Procaine. (a) survey (b) Si 2p, (c) O 1s, (d) N 1s and (e) C 1s.

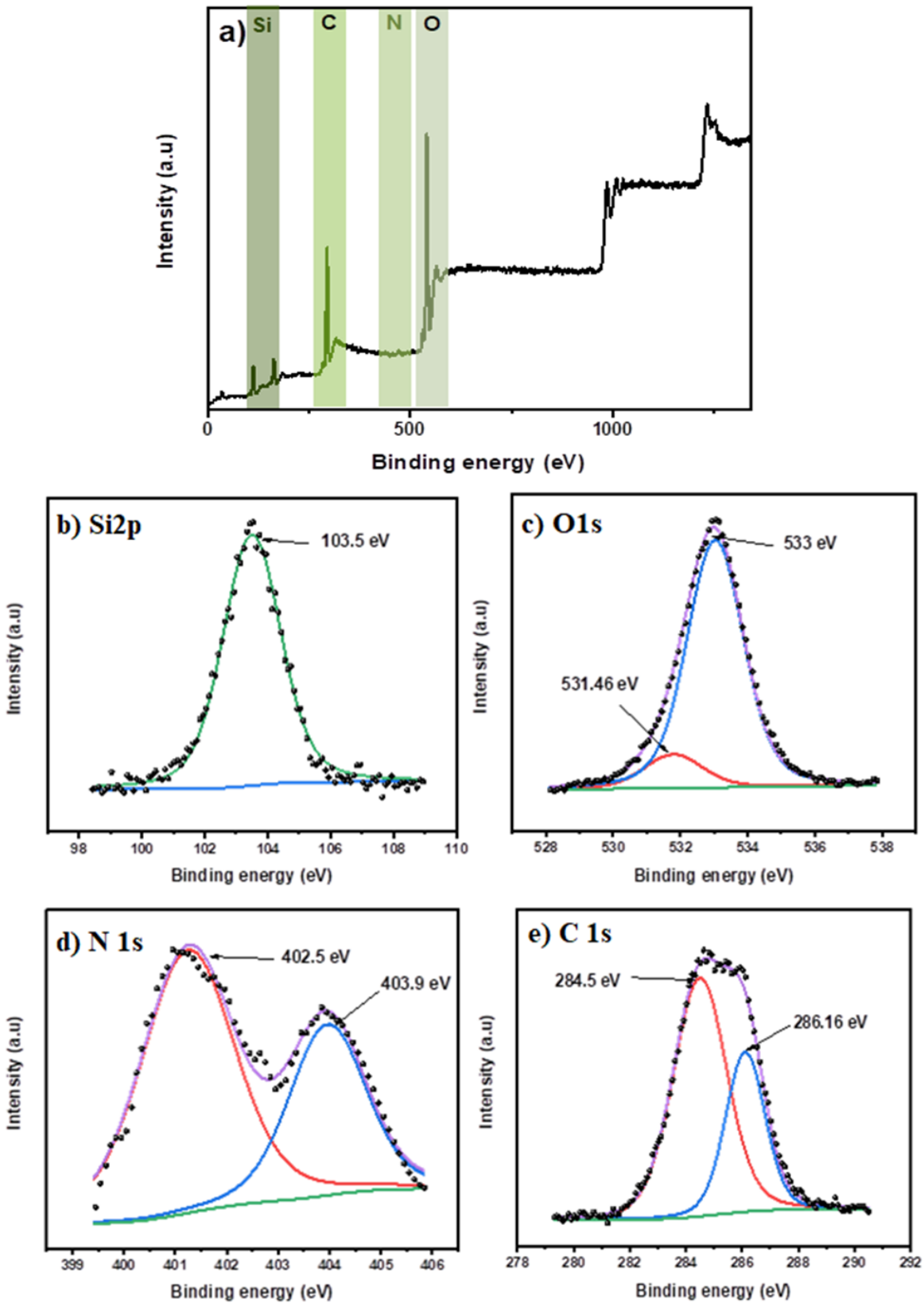

Figure IV.24:XPS spectra of TX-100 mediated silica nanoparticles by microemulsion with Procaine. (a) survey (b) Si 2p, (c) O 1s, (d) N 1s and (e) C 1s.

- **Characterization of SiNPs using ssNMR Spectroscopy**

Acquisition of $^{1}H \rightarrow ^{29}Si$ CP/MAS NMR spectra (**Figure IV.25**) for three SiNPs (water preparation, TX-100 W/O, and TX-100 W/O with PRC) enable analysis and composition of the SiNPs surface. Each spectrum features a narrow pattern composed of two or more overlapping patterns. Additionally, the water preparation (**Figure IV.25 a**) is significantly lower in intensity relative to both TX-100 W/O preparations. Therefore, indicating a significantly lower amount of neighboring hydrogens from hydroxyl groups in $Si(OH)_n$. Each of the patterns can be assigned to various Q-units present in each sample.

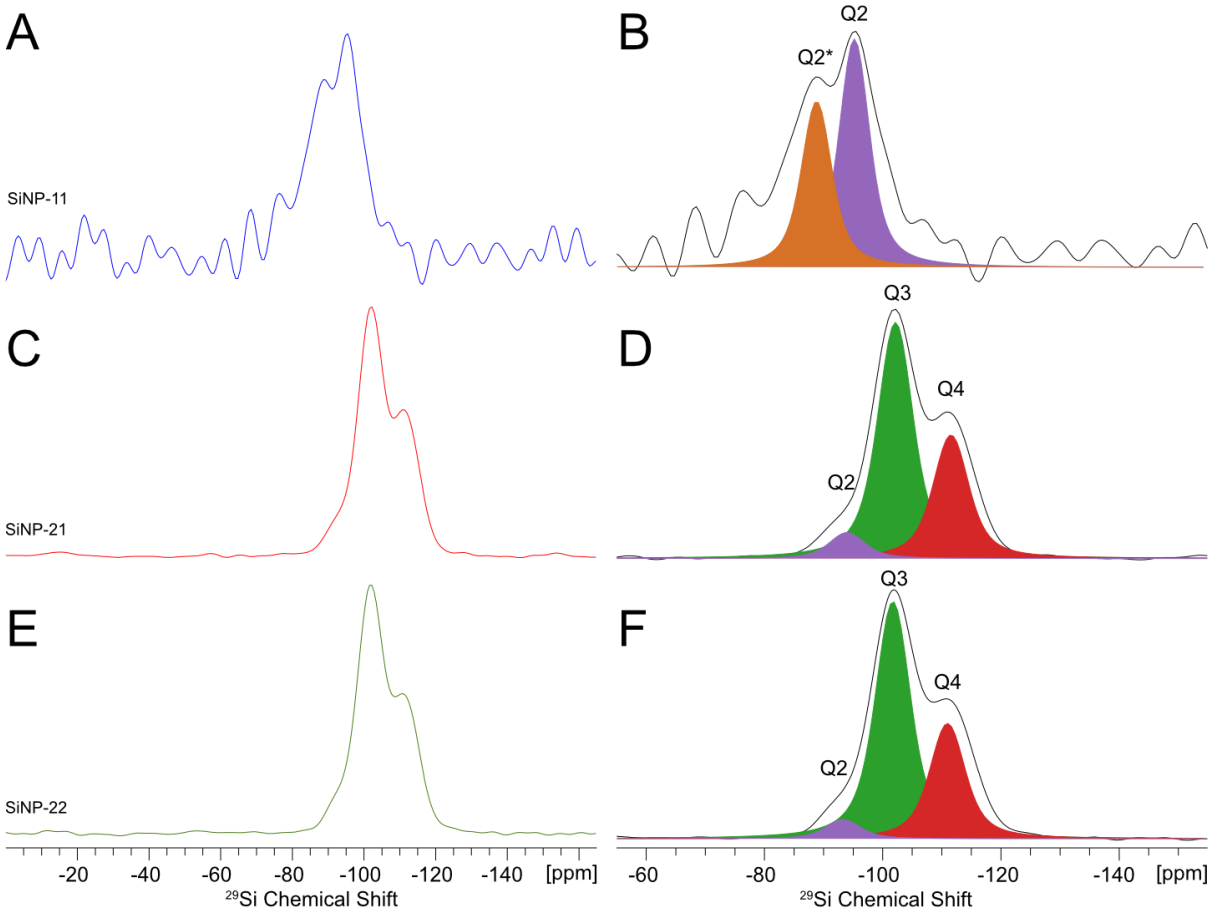

Figure IV.25: Experimental 1H-29Si CP/MAS ssNMR spectra for SiNPs prepared by (A) water, (C) microemulsion with TX-100 without PRC, and (E) microemulsion with TX-100 with PRC with corresponding deconvolutions shown on the right (B, D, and F).

This is supported by the $^{29}Si\{^{1}H\}$ spin echo spectra (**Figure IV.26**) where the water preparation has the greatest intensity, whereas the TX-100 W/O with and without PRC are significantly lower in intensity. Each of the CP/MAS patterns can be assigned to various Q-units present in each sample. For the water preparation (**Figure IV.25 a and d)**, the two distinct patterns can be assigned to Q2-type silicon environments.[71] Comparatively, for the microemulsion preparations with TX-100 with and without PRC (**Figure IV.25 b to f**), three distinct patterns are present and can be assigned to Q2, Q3, and Q4 silicon environments. ^{1}H spin echo MAS spectra were acquired at 12 kHz spinning for all three SiNP samples (**Figure IV.27**). Faulkner and coworkers [72] summarized the ^{1}H chemical shifts for various preparations of SiNPs and comparing our preparations to theirs, the overall line shapes strongly resemble those previously reported. Also, there is an additional small peak at δiso = 2.34 ppm in the TX-100 W/O with PRC, which could indicate the encapsulation of PRC.

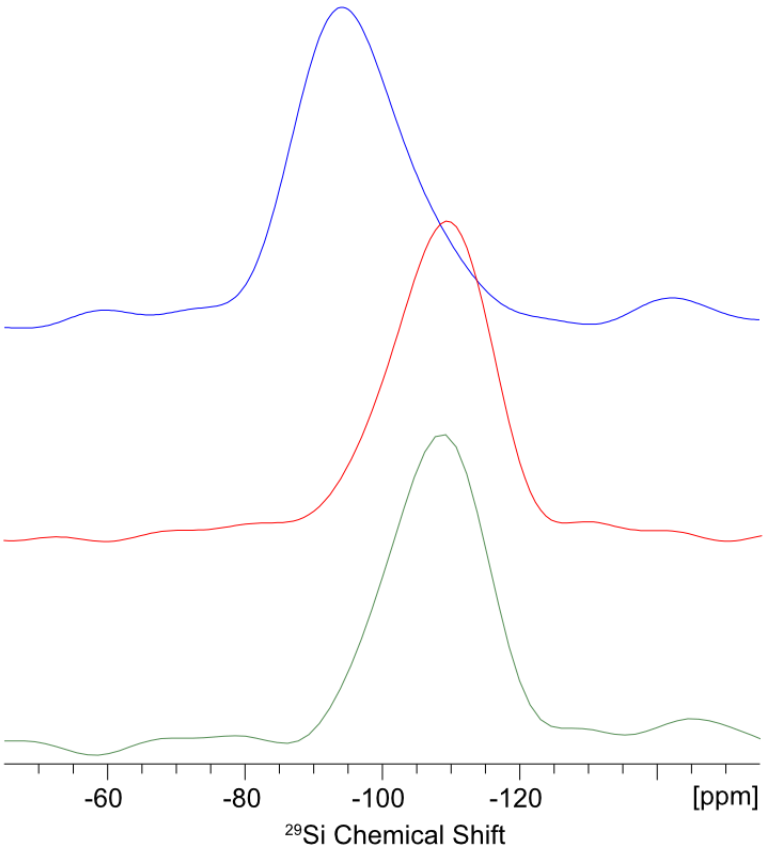

Figure IV.26: Experimental 29Si ssNMR acquired at 9.4 T under spinning conditions (νrot = 12 kHz).

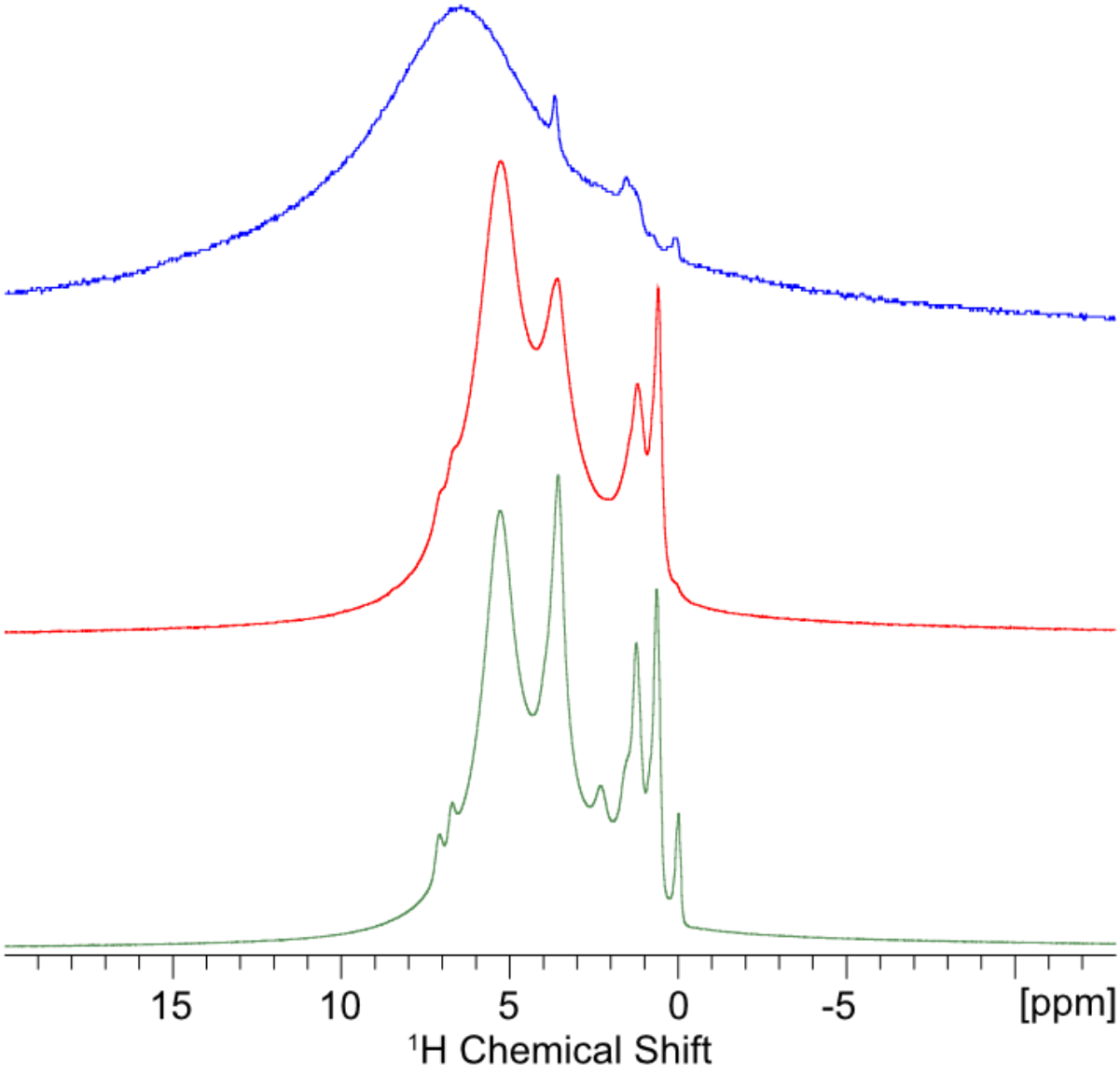

Figure IV.27: Experimental 1H MAS NMR acquired at 9.4 T under MAS conditions (vrot = 12 kHz).

- **PL spectroscopy of SiNPs from microemulsion preparation loaded and free of PRC**

The photoluminescence (PL) spectra of SiNPs, as shown in **Figure IV23**, offer critical insights into their electronic structure and the presence of defect-related emission centers. These spectra reveal distinct emission peaks associated with specific electronic transitions and defects within the SiNPs. **Figure IV23a** presents the PL spectrum of SiNPs synthesized via the TX-100 microemulsion method without procaine. The pronounced peak centered around 415 nm is typically attributed to the recombination of excitons at silicon-oxide-related defects, such as

non-bridging oxygen hole centers (NBOHC) or oxygen-deficient centers (ODC).[157][158] In **Figure IV.28 b**, the PL spectrum of SiNPs with procaine shows an additional peak at 459 nm, which may be linked to electronic transitions associated with procaine molecules. This peak could result from π-π* transitions within the aromatic rings or electronic transitions of nitrogen-containing groups in procaine. The presence of this peak indicates that procaine molecules not only absorb onto the surface but also influence the electronic structure of the SiNPs. The PL spectrum of CTAB-mediated SiNPs without procaine, depicted in **Figure IV.28 c**, similarly displays a dominant emission peak at 415 nm, attributable to the silicon-oxide network. The similarity in emission between CTAB-mediated and TX-100-mediated SiNPs without procaine suggests that the choice of surfactant does not significantly alter the primary defect centers contributing to the PL

However, upon the addition of procaine, as shown in **Figure IV.28 d**, the spectrum of CTAB-mediated SiNPs exhibits a distinct emission feature at 445 nm, labeled as NOV, which does not appear in the TX-100-mediated SiNPs with procaine. This NOV peak may indicate a different interaction mechanism or complexation between procaine and the CTAB-mediated SiNPs, which is absent in the TX-100 system. The comparative analysis of the PL spectra from both CTAB- and TX-100-mediated SiNPs, with and without procaine, underscores the influence of surfactant choice and drug incorporation on the defect-related luminescence properties of the nanoparticles. The introduction of procaine appears to introduce new electronic states or modify existing defect states, as evidenced by the emergence of new PL peaks and changes in peak intensities. These alterations in PL characteristics not only provide a fingerprint of the material's purity and defect states but also have implications for potential optical applications, where controlled luminescence properties are essential.

In conclusion, the PL spectra analysis confirms the sensitivity of the SiNPs' electronic structure to both synthesis conditions and subsequent functionalization with organic molecules. This sensitivity is crucial for tailoring the optical properties of SiNPs for specific applications, including bio-imaging and drug tracking within biological systems.

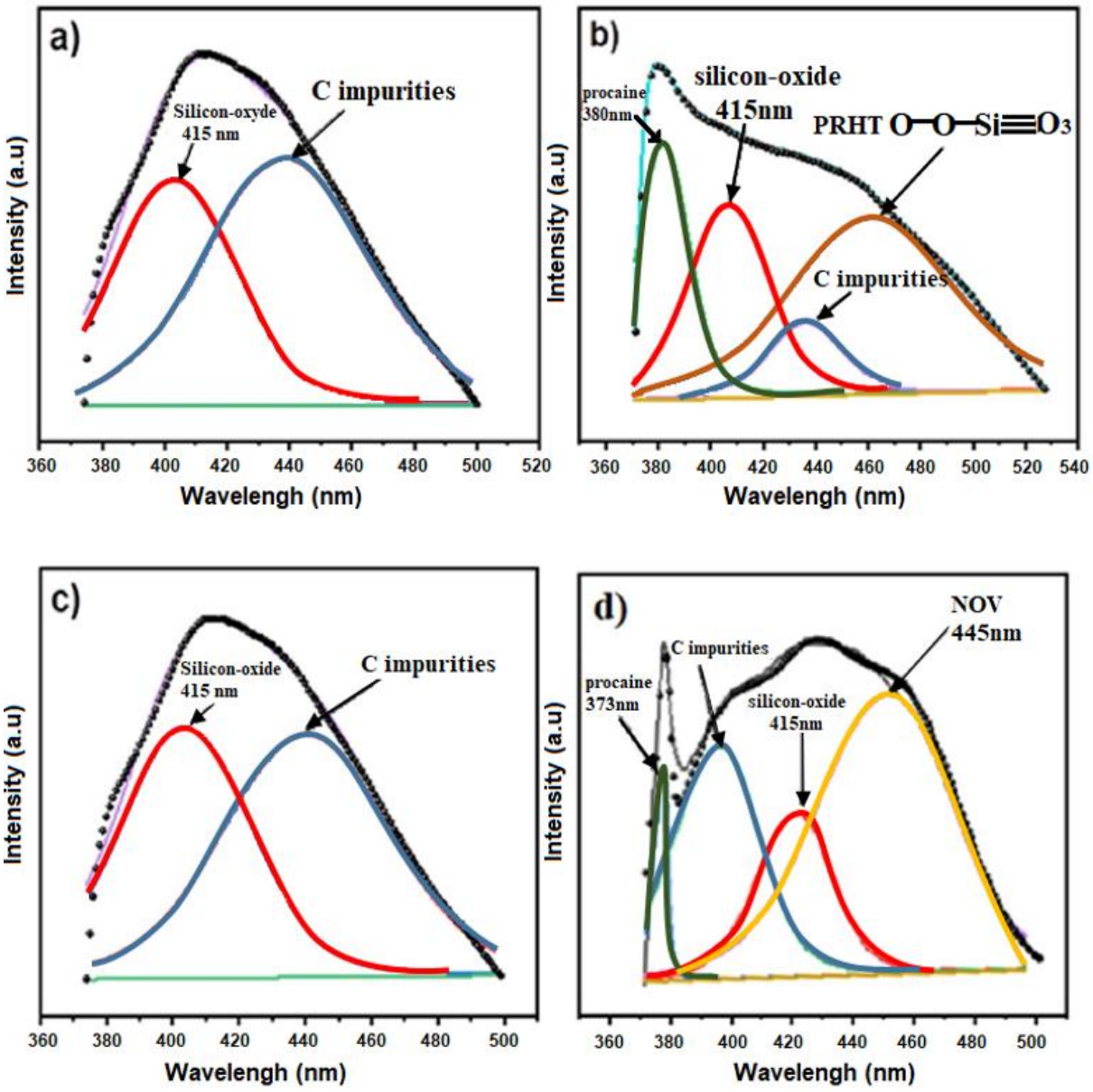

Figure IV.28:(a) The photoluminescence spectra of SiNPs from TX-100 by microemulsion without procaine, (b) SiNPs with procaine drug from TX-100 by microemulsion. (c) SiNPs from CTAB by microemulsion without procaine, and (d) SiNPs with procaine drug from CTAB by microemulsion

V. Conclusion

The aim of this work was to study the use of a silica-based nanoparticle (NPS) in the adsorption of two food colorants, carmine and brilliant green as the first application of NPS. These dyes, recognized as potentially toxic, are present in industrial and domestic waste. Two physico-chemical techniques were used: UV visible spectrophotometry and light scattering (DLS).

Initially, the study focused on the synthesis of mesoporous silica nanoparticles (NPS) prepared by the micellar template sol gel synthesis method. The silica phases develop around micelles of the cationic surfactant CTAB, which are arranged in structures around 100nm in size. However, the structural properties of the synthesized nanoparticles appear to be affected by the structure of the template micelles. which serves as a template. The results obtained by DLS concerning the nanoparticle size distribution (NPS) indicate that our nanoparticle has a homogeneous monodisperse size of around 100nm. These nanoparticles are stable, unaffected by dilution and retained their size after calcination. Secondly, we evaluated the performance and capacity of nanoparticles (NPS) in the adsorption of two dyes, carmine and brilliant green. The influence of various experimental parameters was studied using UV visible spectrophotometry, such as contact time, adsorbent mass and the effect of agitation on adsorption by calcined NPS. The results obtained for the no-stir mode showed slow kinetics and a pronounced affinity of NPS for Brilliant Green in comparison with carmine. On the other hand, in the case of VB adsorption, we find that the adsorption capacity of NPS increases when we increase the stirring speed. This can be explained by the increased electrostatic attraction between the negatively charged NPS and the positively charged VB dye (cationic dye). For Carmine, on the other hand, agitation causes desorption after the first 10 minutes. This can be explained by the fact that high agitation velocities break the adsorption forces in the pores and prevent good diffusion of Carmine in the NPS. With regard to the effect of temperature, the results show that Carmine adsorption is favored by increasing temperature.

This increase can be explained by the fact that temperature stabilizes the physical forces of attraction involved. In the case of VB adsorption, the adsorption capacity decreases with increasing temperature. These results show that the increase in temperature in the case of VB induces an increase in the mobility of dye particles in solution and a decrease in the forces of dye attraction or diffusion on the active surface of the dyes

decrease dye attraction or diffusion forces on the active surface of nanoparticles, as high stirring speeds break the adsorption forces in the pores and prevent good diffusion of Carmine into the NPS.

As far as the effect of temperature is concerned, the results show that carmine adsorption is enhanced by increasing temperature. This can be explained by the fact that temperature stabilizes the physical forces of attraction.

What is also important in this study we employed two different chemical surfactants, CTAB and TX-100, to mediate the synthesis of silica nanoparticles (SiNPs) using an effective sol-gel method at low and ambient temperatures. This approach allowed for a comparison between SiNPs prepared in an aqueous medium and those synthesized via microemulsion, yielding particles with diameters ranging from 110 to 800 nm. In the aqueous medium, small variations in base concentration were sufficient to control the SiNPs diameter, as these changes affected the concentration of hydroxyl ions. Additionally, maintaining a lower pH led to a slight decrease in SiNPs diameter. The geometry of the aggregates formed by the surfactant molecules (TX-100 and CTAB) in solution is influenced by the interplay between the hydrophobic affinity of the carbon chain, electrostatic repulsions, and steric constraints of the hydrophilic polar heads. These structural outcomes can be predicted by the surfactant parameters. In water-in-oil (W/O) microemulsions, ionic surfactants stabilize the system through electrostatic repulsion, while nonionic surfactants do so via steric repulsion. This study explored reverse micellar systems containing water, (TX-100 or CTAB), 1-butanol, and n-hexane. Reverse micelles can form within a specific concentration range of TX-100 or CTAB, requiring significant amounts of surfactants and cosurfactants for microemulsion preparation. For the micellar system using TX-100, the hierarchical distribution of the micellar interface facilitates the material exchange of tetraethoxysilane (TEOS) and limits its hydrolysis within the micelles. This process promotes the complete hydrolysis of TEOS in the micellar cores, resulting in SiNPs with excellent monodispersity. Conversely, the reverse microemulsion of CTAB leads to an unstable emulsion, producing SiNPs with flocculated dispersion due to an excess of water and insufficient surfactant. This provided insights into the optimal and reproducible preparation of SiNPs. The use of microemulsion with TX-100 enabled the completion of the synthesis process, culminating in the successful incorporation of the anesthetic procaine.

VI. References:

[1] J. E. Amonette and J. Matyáš, "Functionalized silica aerogels for gas-phase purification, sensing, and catalysis: A review," *Microporous Mesoporous Mater.*, vol. 250, pp. 100–119, 2017.

[2] A. P. Wardanu and N. S. Indrasti, "Green Synthesis of Silica Nanoparticles (Si-NPs) from Palm Oil Fuel Ash (POFA) and its Application to Purification Water: A Review," in *IOP Conference Series: Earth and Environmental Science*, IOP Publishing, 2024, p. 12015.

[3] O. V Dement'eva *et al.*, "Drug-templated mesoporous silica nanocontainers with extra high payload and controlled release rate," *Colloids Surfaces B Biointerfaces*, vol. 185, p. 110577, 2020.

[4] S. Seré *et al.*, "Altering the biodegradation of mesoporous silica nanoparticles by means of experimental parameters and surface functionalization," *J. Nanomater.*, vol. 2018, 2018.

[5] Y. He *et al.*, "One-pot synthesis of chlorhexidine-templated biodegradable mesoporous organosilica nanoantiseptics," *Colloids Surfaces B Biointerfaces*, vol. 187, p. 110653, 2020.

[6] C. Argyo, V. Weiss, C. Bräuchle, and T. Bein, "Multifunctional mesoporous silica nanoparticles as a universal platform for drug delivery," *Chem. Mater.*, vol. 26, no. 1, pp. 435–451, 2014.

[7] W. Stöber, A. Fink, and E. Bohn, "Controlled growth of monodisperse silica spheres in the micron size range," *J. Colloid Interface Sci.*, vol. 26, no. 1, pp. 62–69, 1968.

[8] T. Ribeiro *et al.*, "Silica nanocarriers with user-defined precise diameters by controlled template self-assembly," *J. Colloid Interface Sci.*, vol. 561, pp. 609–619, 2020, doi: 10.1016/j.jcis.2019.11.036.

[9] C. Mochizuki, J. Nakamura, and M. Nakamura, "Development of non-porous silica nanoparticles towards cancer photo-theranostics," *Biomedicines*, vol. 9, no. 1, p. 73, 2021.

[10] H.-P. Lin and C.-Y. Mou, "Structural and morphological control of cationic surfactant-

templated mesoporous silica," *Acc. Chem. Res.*, vol. 35, no. 11, pp. 927–935, 2002.

[11] M. El Hariri El Nokab, "Formation and Structural Analysis of Ultra Low-Density Silica Based Aerogels." University of Siegen Siegen, Germany, 2018.

[12] Y.-D. Chiang, H.-Y. Lian, S.-Y. Leo, S.-G. Wang, Y. Yamauchi, and K. C.-W. Wu, "Controlling particle size and structural properties of mesoporous silica nanoparticles using the Taguchi method," *J. Phys. Chem. C*, vol. 115, no. 27, pp. 13158–13165, 2011.

[13] L. Sierra, B. Lopez, and J.-L. Guth, "Preparation of mesoporous silica particles with controlled morphology from sodium silicate solutions and a non-ionic surfactant at pH values between 2 and 6," *Microporous mesoporous Mater.*, vol. 39, no. 3, pp. 519–527, 2000.

[14] H. B. S. Chan, P. M. Budd, and T. deV Naylor, "Control of mesostructured silica particle morphology," *J. Mater. Chem.*, vol. 11, no. 3, pp. 951–957, 2001.

[15] P. Linton, H. Wennerström, and V. Alfredsson, "Controlling particle morphology and size in the synthesis of mesoporous SBA-15 materials," *Phys. Chem. Chem. Phys.*, vol. 12, no. 15, pp. 3852–3858, 2010.

[16] L. Han *et al.*, "One-pot morphology-controlled synthesis of various shaped mesoporous silica nanoparticles," *J. Mater. Sci.*, vol. 48, pp. 5718–5726, 2013.

[17] X. Wang *et al.*, "Synthesis of ordered mesoporous silica with tunable morphologies and pore sizes via a nonpolar solvent-assisted stober method," *Chem. Mater.*, vol. 28, no. 7, pp. 2356–2362, 2016.

[18] H. Yamada, C. Urata, S. Higashitamori, Y. Aoyama, Y. Yamauchi, and K. Kuroda, "Critical roles of cationic surfactants in the preparation of colloidal mesostructured silica nanoparticles: control of mesostructure, particle size, and dispersion," *ACS Appl. Mater. Interfaces*, vol. 6, no. 5, pp. 3491–3500, 2014.

[19] H. Yamada, C. Urata, H. Ujiie, Y. Yamauchi, and K. Kuroda, "Preparation of aqueous colloidal mesostructured and mesoporous silica nanoparticles with controlled particle size in a very wide range from 20 nm to 700 nm," *Nanoscale*, vol. 5, no. 13, pp. 6145–6153, 2013.

[20] I. I. Slowing, J. L. Vivero-Escoto, B. G. Trewyn, and V. S.-Y. Lin, "Mesoporous silica

nanoparticles: structural design and applications," *J. Mater. Chem.*, vol. 20, no. 37, pp. 7924–7937, 2010.

[21] L. P. Singh *et al.*, "Sol-Gel processing of silica nanoparticles and their applications," *Adv. Colloid Interface Sci.*, vol. 214, pp. 17–37, 2014.

[22] A. Corma, "From microporous to mesoporous molecular sieve materials and their use in catalysis," *Chem. Rev.*, vol. 97, no. 6, pp. 2373–2420, 1997.

[23] J. R. Jones *et al.*, "Controlling particle size in the Stöber process and incorporation of calcium".

[24] R. S. Fernandes, I. M. Raimundo Jr, and M. F. Pimentel, "Revising the synthesis of Stöber silica nanoparticles: A multivariate assessment study on the effects of reaction parameters on the particle size," *Colloids Surfaces A Physicochem. Eng. Asp.*, vol. 577, pp. 1–7, 2019.

[25] K. Landfester, "Synthesis of colloidal particles in miniemulsions," *Annu. Rev. Mater. Res.*, vol. 36, pp. 231–279, 2006.

[26] C.-L. Chang and H. S. Fogler, "Controlled formation of silica particles from tetraethyl orthosilicate in nonionic water-in-oil microemulsions," *Langmuir*, vol. 13, no. 13, pp. 3295–3307, 1997.

[27] Y.-S. Lin, S.-H. Wu, C.-T. Tseng, Y. Hung, C. Chang, and C.-Y. Mou, "Synthesis of hollow silica nanospheres with a microemulsion as the template," *Chem. Commun.*, no. 24, pp. 3542–3544, 2009.

[28] L. Yao, G. Xu, W. Dou, and Y. Bai, "The control of size and morphology of nanosized silica in Triton X-100 based reverse micelle," *Colloids Surfaces A Physicochem. Eng. Asp.*, vol. 316, no. 1–3, pp. 8–14, 2008.

[29] Y. Zhang, B. Zhen, Y. Hu, G. Liang, and Y. Feng, "A reverse micellar system with Triton X-100: effect of surfactant polydispersity and preparation of monodisperse silica nanoparticles," *Soft Matter*, vol. 16, no. 2, pp. 383–389, 2020.

[30] M. A. Malik, M. Y. Wani, and M. A. Hashim, "Microemulsion method: A novel route to synthesize organic and inorganic nanomaterials: 1st Nano Update," *Arab. J. Chem.*, vol. 5, no. 4, pp. 397–417, 2012.

[31] M. E. Flores *et al.*, “Water-induced phase transition in Cyclohexane/n-Hexanol/Triton X-100 mixtures at a molar composition of 1/16/74 studied by NMR,” *J. Phys. Chem. B*, vol. 121, no. 4, pp. 876–882, 2017.

[32] G. C. Carvalho *et al.*, “Cetyltrimethylammonium bromide in the synthesis of mesoporous silica nanoparticles: general aspects and in vitro toxicity,” *Adv. Colloid Interface Sci.*, p. 102746, 2022.

[33] L. Ernawati, R. Balgis, T. Ogi, and K. Okuyama, “Tunable synthesis of mesoporous silica particles with unique radially oriented pore structures from tetramethyl orthosilicate via oil–water emulsion process,” *Langmuir*, vol. 33, no. 3, pp. 783–790, 2017.

[34] S. Schacht, Q. Huo, I. G. Voigt-Martin, G. D. Stucky, and F. Schüth, “Oil-water interface templating of mesoporous macroscale structures,” *Science (80-.).*, vol. 273, no. 5276, pp. 768–771, 1996.

[35] Z. Wu *et al.*, “Solid and hollow nanoparticles templated using non-ionic surfactant-based reverse micelles and vesicles,” *Colloids Surfaces A Physicochem. Eng. Asp.*, vol. 634, p. 127917, 2022.

[36] J. Yin *et al.*, “Design, synthesis and biological evaluation of novel procaine derivatives for intravenous anesthesia,” *Bioorg. Med. Chem. Lett.*, vol. 60, p. 128587, 2022.

[37] T. Kasaba, S. Onizuka, and M. Takasaki, “Procaine and mepivacaine have less toxicity in vitro than other clinically used local anesthetics,” *Anesth. Analg.*, vol. 97, no. 1, pp. 85–90, 2003.

[38] S. Wiedling and C. Tegnér, “7 Local Anaesthetics,” *Prog. Med. Chem.*, vol. 3, pp. 332–398, 1963.

[39] A. B. Seifen, A. A. Ferrari, E. E. Seifen, D. S. Thompson, and J. Chapman, “Pharmacokinetics of intravenous procaine infusion in humans,” *Anesth. Analg.*, vol. 58, no. 5, pp. 382–386, 1979.

[40] B. L. Steinberg, “INTRAVENOUS PROCAINE: ITS EFFECT ON LIVER FUNCTION IN MAN AS DETERMINED BY THE CEPHALIN FLOCCULATION TEST,” in *The Journal of the American Society of Anesthesiologists*, The American Society of Anesthesiologists, 1949, pp. 739–742.

[41] D. Li, Y. Yan, L. Yu, and Y. Duan, “Procaine attenuates pain behaviors of neuropathic pain model rats possibly via inhibiting JAK2/STAT3,” *Biomol. Ther. (Seoul).*, vol. 24, no. 5, p. 489, 2016.

[42] A. S. Keats, G. L. D’Alessandro, and H. K. Beecher, “A controlled study of pain relief by intravenous procaine,” *J. Am. Med. Assoc.*, vol. 147, no. 18, pp. 1761–1763, 1951.

[43] D. S. Thompson, A. B. Seifen, A. A. Ferrari, and N. W. Lawson, “Reappraisal of intravenous procaine as a short-acting anesthetic adjuvant,” *Am. J. Surg.*, vol. 138, no. 6, pp. 798–804, 1979.

[44] V. P. Torchilin, “Micellar nanocarriers: pharmaceutical perspectives,” *Pharm. Res.*, vol. 24, pp. 1–16, 2007.

[45] K. Letchford and H. Burt, “A review of the formation and classification of amphiphilic block copolymer nanoparticulate structures: micelles, nanospheres, nanocapsules and polymersomes,” *Eur. J. Pharm. Biopharm.*, vol. 65, no. 3, pp. 259–269, 2007.

[46] G. Gillberg, H. Lehtinen, and S. Friberg, “NMR and IR investigation of the conditions determining the stability of microemulsions,” *J. Colloid Interface Sci.*, vol. 33, no. 1, pp. 40–53, 1970.

[47] J. H. Schulman, W. Stoeckenius, and L. M. Prince, “Mechanism of formation and structure of micro emulsions by electron microscopy,” *J. Phys. Chem.*, vol. 63, no. 10, pp. 1677–1680, 1959.

[48] T. P. Hoar and J. H. Schulman, “Transparent water-in-oil dispersions: the oleopathic hydro-micelle,” *Nature*, vol. 152, no. 3847, pp. 102–103, 1943.

[49] J. Salager, R. E. Antón, D. A. Sabatini, J. H. Harwell, E. J. Acosta, and L. I. Tolosa, “Enhancing solubilization in microemulsions—state of the art and current trends,” *J. Surfactants Deterg.*, vol. 8, no. 1, pp. 3–21, 2005.

[50] J. BRIANT, *Phénomènes d’interface. Agents de surface: principes et modes d’action*. Editions Technip, 1989.

[51] J. H. Schulman and D. P. Riley, “X-ray investigation of the structure of transparent oil-water disperse systems. I,” *J. Colloid Sci.*, vol. 3, no. 4, pp. 383–405, 1948.

[52] B. K. Paul and S. P. Moulik, “Microemulsions: an overview,” *J. Dispers. Sci. Technol.*,

vol. 18, no. 4, pp. 301–367, 1997.

[53] K. Shinoda and E. Hutchinson, “Pseudo-phase separation model for thermodynamic calculations on micellar solutions1,” *J. Phys. Chem.*, vol. 66, no. 4, pp. 577–582, 1962.

[54] P. A. Winsor, “Solvent properties of amphiphilic compounds,” *(No Title)*, 1954.

[55] B. K. Paul and S. P. Moulik, “Uses and applications of microemulsions,” *Curr. Sci.*, pp. 990–1001, 2001.

[56] M. Ebelmen, “Sur l’hyalite artificielle et l’hydrophane,” *Comptes rendus l’académie des Sci.*, vol. 25, pp. 854–856, 1847.

[57] J. Livage, “revue verre, vol 5, n 6,«,” *Les procédés sol-gel*, pp. 205–206, 2000.

[58] M. Amoura, N. Nassif, C. Roux, J. Livage, and T. Coradin, “Sol–gel encapsulation of cells is not limited to silica: Long-term viability of bacteria in alumina matrices,” *Chem. Commun.*, no. 39, pp. 4015–4017, 2007.

[59] N. Nassif, O. Bouvet, M. Noelle Rager, C. Roux, T. Coradin, and J. Livage, “Living bacteria in silica gels,” *Nat. Mater.*, vol. 1, no. 1, pp. 42–44, 2002.

[60] S. Sakka, *Handbook of sol-gel science and technology. 1. Sol-gel processing*, vol. 1. Springer Science & Business Media, 2005.

[61] D. Bradley, R. C. Mehrotra, I. Rothwell, and A. Singh, *Alkoxo and aryloxo derivatives of metals*. Elsevier, 2001.

[62] N. Y. Turova, E. P. Turevskaya, V. G. Kessler, and M. I. Yanovskaya, *The chemistry of metal alkoxides*. Springer Science & Business Media, 2007.

[63] A.-M. Siouffi, “Silica gel-based monoliths prepared by the sol–gel method: facts and figures,” *J. Chromatogr. A*, vol. 1000, no. 1–2, pp. 801–818, 2003.

[64] P. Innocenzi, G. Brusatin, M. Guglielmi, R. Signorini, R. Bozio, and M. Maggini, “3-(Glycidoxypropyl)-trimethoxysilane–TiO2 hybrid organic–inorganic materials for optical limiting,” *J. Non. Cryst. Solids*, vol. 265, no. 1–2, pp. 68–74, 2000.

[65] R. Pardo, M. Zayat, and D. Levy, “Photochromic organic–inorganic hybrid materials,” *Chem. Soc. Rev.*, vol. 40, no. 2, pp. 672–687, 2011.

[66] J. Livage, M. Henry, and C. Sanchez, “Sol-gel chemistry of transition metal oxides,”

Prog. solid state Chem., vol. 18, no. 4, pp. 259–341, 1988.

[67] E. Kroke, Y.-L. Li, C. Konetschny, E. Lecomte, C. Fasel, and R. Riedel, "Silazane derived ceramics and related materials," *Mater. Sci. Eng. R Reports*, vol. 26, no. 4–6, pp. 97–199, 2000.

[68] M. Mennig, M. Zahnhausen, and H. K. Schmidt, "Novel nonhydrolytic sol-gel route to low-OH-and CH-containing organic-inorganic composites," in *Organic-inorganic hybrid materials for photonics*, SPIE, 1998, pp. 68–78.

[69] R. J. P. Corriu, "Hypervalent species of silicon: structure and reactivity," *J. Organomet. Chem.*, vol. 400, no. 1–2, pp. 81–106, 1990.

[70] M. Ricaud and O. Witschger, *Les nanomatériaux: définitions, risques toxicologiques, caractérisation de l'exposition professionnelle et mesures de prévention*. INRS, 2009.

[71] L. E. Zapata, G. Portela, O. M. Suárez, and O. Carrasquillo, "Rheological performance and compressive strength of superplasticized cementitious mixtures with micro/nano-SiO2 additions," *Constr. Build. Mater.*, vol. 41, pp. 708–716, 2013.

[72] L. Senff, D. Hotza, S. Lucas, V. M. Ferreira, and J. A. Labrincha, "Effect of nano-SiO2 and nano-TiO2 addition on the rheological behavior and the hardened properties of cement mortars," *Mater. Sci. Eng. A*, vol. 532, pp. 354–361, 2012.

[73] D. F. Lin, K. L. Lin, W. C. Chang, H. L. Luo, and M. Q. Cai, "Improvements of nano-SiO2 on sludge/fly ash mortar," *Waste Manag.*, vol. 28, no. 6, pp. 1081–1087, 2008.

[74] G. H. Barbhuiya, M. A. Moiz, S. D. Hasan, and M. M. Zaheer, "Effects of the nanosilica addition on cement concrete: A review," *Mater. Today Proc.*, vol. 32, pp. 560–566, 2020.

[75] L. R. Hirsch *et al.*, "Nanoshell-mediated near-infrared thermal therapy of tumors under magnetic resonance guidance," *Proc. Natl. Acad. Sci.*, vol. 100, no. 23, pp. 13549–13554, 2003.

[76] M. Vallet-Regí, "Mesoporous silica nanoparticles: their projection in nanomedicine," *Int. Sch. Res. Not.*, vol. 2012, 2012.

[77] B. Munoz, A. Ramila, J. Perez-Pariente, I. Diaz, and M. Vallet-Regi, "MCM-41 organic modification as drug delivery rate regulator," *Chem. Mater.*, vol. 15, no. 2, pp.

500–503, 2003.

[78] J. Lu, M. Liong, J. I. Zink, and F. Tamanoi, “Mesoporous silica nanoparticles as a delivery system for hydrophobic anticancer drugs,” *small*, vol. 3, no. 8, pp. 1341–1346, 2007.

[79] P. Krasucka, W. Stefaniak, A. Kierys, and J. Goworek, “Polymer–silica composites and silicas produced by high-temperature degradation of organic component,” *Thermochim. Acta*, vol. 615, pp. 43–50, 2015.

[80] S. Kang, S. Il Hong, C. R. Choe, M. Park, S. Rim, and J. Kim, “Preparation and characterization of epoxy composites filled with functionalized nanosilica particles obtained via sol–gel process,” *Polymer (Guildf).*, vol. 42, no. 3, pp. 879–887, 2001.

[81] G. Ragosta, M. Abbate, P. Musto, G. Scarinzi, and L. Mascia, “Epoxy-silica particulate nanocomposites: chemical interactions, reinforcement and fracture toughness,” *Polymer (Guildf).*, vol. 46, no. 23, pp. 10506–10516, 2005.

[82] M. Niederberger and N. Pinna, “Aqueous and nonaqueous sol-gel chemistry,” *Met. oxide nanoparticles Org. solvents Synth. Form. Assem. Appl.*, pp. 7–18, 2009.

[83] M. J. Van Bommel and A. B. De Haan, “Drying of silica aerogel with supercritical carbon dioxide,” *J. Non. Cryst. Solids*, vol. 186, pp. 78–82, 1995.

[84] P. R. Aravind, P. Shajesh, G. D. Soraru, and K. G. K. Warrier, “Ambient pressure drying: a successful approach for the preparation of silica and silica based mixed oxide aerogels,” *J. sol-gel Sci. Technol.*, vol. 54, pp. 105–117, 2010.

[85] C. J. Brinker, “Hydrolysis and condensation of silicates: effects on structure,” *J. Non. Cryst. Solids*, vol. 100, no. 1–3, pp. 31–50, 1988.

[86] D. R. Uhlmann and D. R. Ulrich, *Ultrastructure processing of advanced materials*. Wiley New York, 1992.

[87] I. C. Tilgner, P. Fischer, F. M. Bohnen, H. Rehage, and W. F. Maier, “Effect of acidic, basic and fluoride-catalyzed sol-gel transitions on the preparation of sub-nanostructured silica,” *Microporous Mater.*, vol. 5, no. 1–2, pp. 77–90, 1995.

[88] C. J. Cornelius, “Physical and gas permeation properties of a series of novel hybrid inorganic-organic composites based on a synthesized fluorinated polyimide.” Virginia

Polytechnic Institute and State University, 2000.

[89] T. Matsoukas and E. Gulari, “Dynamics of growth of silica particles from ammonia-catalyzed hydrolysis of tetra-ethyl-orthosilicate,” *J. Colloid Interface Sci.*, vol. 124, no. 1, pp. 252–261, 1988.

[90] T. Matsoukas and E. Gulari, “Monomer-addition growth with a slow initiation step: a growth model for silica particles from alkoxides,” *J. Colloid Interface Sci.*, vol. 132, no. 1, pp. 13–21, 1989.

[91] R. I. Nooney, D. Thirunavukkarasu, Y. Chen, R. Josephs, and A. E. Ostafin, “Synthesis of nanoscale mesoporous silica spheres with controlled particle size,” *Chem. Mater.*, vol. 14, no. 11, pp. 4721–4728, 2002.

[92] Y.-B. Zhang, X.-F. Qian, Z.-K. Li, J. Yin, and Z.-K. Zhu, “Synthesis of novel mesoporous silica spheres with starburst pore canal structure,” *J. Solid State Chem.*, vol. 177, no. 3, pp. 844–848, 2004.

[93] M.-J. Schwuger, K. Stickdorn, and R. Schomaecker, “Microemulsions in technical processes,” *Chem. Rev.*, vol. 95, no. 4, pp. 849–864, 1995.

[94] K. Osseo-Asare and F. J. Arriagada, “Preparation of SiO2 nanoparticles in a non-ionic reverse micellar system,” *Colloids and surfaces*, vol. 50, pp. 321–339, 1990.

[95] A. van Blaaderen and A. P. M. Kentgens, “Particle morphology and chemical microstructure of colloidal silica spheres made from alkoxysilanes,” *J. Non. Cryst. Solids*, vol. 149, no. 3, pp. 161–178, 1992.

[96] R. G. Larson, “Self-assembly of surfactant liquid crystalline phases by Monte Carlo simulation,” *J. Chem. Phys.*, vol. 91, no. 4, pp. 2479–2488, 1989.

[97] M.-P. Pileni, T. Zemb, and C. Petit, “Solubilization by reverse micelles: solute localization and structure perturbation,” *Chem. Phys. Lett.*, vol. 118, no. 4, pp. 414–420, 1985.

[98] P. Sharma, S. Brown, M. Varshney, and B. Moudgil, “Surfactant-mediated fabrication of optical nanoprobes,” *Interfacial Process. Mol. Aggreg. Surfactants*, pp. 189–233, 2008.

[99] I. Capek, “Preparation of metal nanoparticles in water-in-oil (w/o) microemulsions,”

Adv. Colloid Interface Sci., vol. 110, no. 1–2, pp. 49–74, 2004.

[100] J. Eastoe, M. J. Hollamby, and L. Hudson, "Recent advances in nanoparticle synthesis with reversed micelles," *Adv. Colloid Interface Sci.*, vol. 128, pp. 5–15, 2006.

[101] M. A. López-Quintela, C. Tojo, M. C. Blanco, L. G. Rio, and J. R. Leis, "Microemulsion dynamics and reactions in microemulsions," *Curr. Opin. Colloid Interface Sci.*, vol. 9, no. 3–4, pp. 264–278, 2004.

[102] S. Santra, R. Tapec, N. Theodoropoulou, J. Dobson, A. Hebard, and W. Tan, "Synthesis and characterization of silica-coated iron oxide nanoparticles in microemulsion: the effect of nonionic surfactants," *Langmuir*, vol. 17, no. 10, pp. 2900–2906, 2001.

[103] T. Aubert, "Nanoparticules de silice fonctionnelles à base de cluster d'éléments de transition." Université Rennes 1, 2011.

[104] X. Zhu and T. Gao, "Spectrometry," in *Nano-inspired biosensors for protein assay with clinical applications*, Elsevier, 2019, pp. 237–264.

[105] F. Babick, "Dynamic light scattering (DLS)," in *Characterization of nanoparticles*, Elsevier, 2020, pp. 137–172.

[106] M. Knoll and E. Ruska, "Das elektronenmikroskop," *Zeitschrift für Phys.*, vol. 78, pp. 318–339, 1932.

[107] E. Ruska, "The development of the electron microscope and of electron microscopy," *Rev. Mod. Phys.*, vol. 59, no. 3, p. 627, 1987.

[108] M. Suga *et al.*, "Recent progress in scanning electron microscopy for the characterization of fine structural details of nano materials," *Prog. Solid State Chem.*, vol. 42, no. 1–2, pp. 1–21, 2014.

[109] D. C. Joy and C. S. Joy, "Low voltage scanning electron microscopy," *Micron*, vol. 27, no. 3–4, pp. 247–263, 1996.

[110] J. W. Jeffery, "Methods in X-ray Crystallography," 1971.

[111] C. ARONICA, "La diffraction des rayons X: Principes et applications d'une méthode de caractérisation des arrangements atomiques dans les solides cristallisés," *Actual. Chim.*, no. 346, 2010.

[112] P. Sinha, A. Datar, C. Jeong, X. Deng, Y. G. Chung, and L.-C. Lin, “Surface area determination of porous materials using the Brunauer–Emmett–Teller (BET) method: limitations and improvements,” *J. Phys. Chem. C*, vol. 123, no. 33, pp. 20195–20209, 2019.

[113] N. Nasuha and B. H. Hameed, “Adsorption of methylene blue from aqueous solution onto NaOH-modified rejected tea,” *Chem. Eng. J.*, vol. 166, no. 2, pp. 783–786, 2011.

[114] C. E. Chitour, “Physico-chimie des surfaces. 2eme édition augmentée.” Office des publications universitaire, Alger, 2004.

[115] H. Hertz, “Ueber einen Einfluss des ultravioletten Lichtes auf die electrische Entladung,” *Ann. Phys.*, vol. 267, no. 8, pp. 983–1000, 1887.

[116] A. Einstein, “Über einen die Erzeugung und Verwandlung des Lichtes betreffenden heuristischen Gesichtspunkt.” Albert Einstein-Gesellschaft, 1905.

[117] K. Siegbahn, “Atomic, molecular and solid state structure studied by means of electron spectroscopy,” in *ESCA*, 1967.

[118] D. Briggs, “Practical Surface analysis second edition Vol. 1, Auger and X-ray photoelectron spectroscopy,” *John Wiley Sons Ltd., New York*, 1990.

[119] T. M. Duc, “Analyse de surface par ESCA. Principe et instrumentation,” *Tech. l’ingénieur. Anal. caractérisation*, vol. 4, no. P2625, pp. P2625-1, 1998.

[120] J. Reichman, “Handbook of optical filters for fluorescence microscopy,” *Chroma Technol. Corp.*, 2000.

[121] G. D. Gilliland, “Photoluminescence spectroscopy of crystalline semiconductors,” *Mater. Sci. Eng. R Reports*, vol. 18, no. 3–6, pp. 99–399, 1997.

[122] C. R. Ronda, “Emission and excitation mechanisms of phosphors,” *CMOS-MEMS*, 2008.

[123] M. Anpo, M. Kondo, C. Louis, M. Che, and S. Coluccia, “Application of dynamic photoluminescence spectroscopy to the study of the active surface sites on supported molybdenum/silica catalysts: features of anchored and impregnated catalysts,” *J. Am. Chem. Soc.*, vol. 111, no. 24, pp. 8791–8799, 1989.

[124] N. Yahiaoui, “Etude de l’absorption des composes phenologiques des margines d’olive

sur carbonate de calcium, hydroxypatite et charbon actif." Tizi Ouzou, 2012.

[125] A. Camut, "Mise en place du contrôle terminal des préparations d'anticancéreux injectables par spectrométrie UV-visible-IRTF, Multispec® à l'Unité de Pharmacie Clinique et Cancérologique de l'Hôpital Bon Secours de Metz: aspects analytiques et organisationnels." UHP-Université Henri Poincaré, 2009.

[126] S. HAMRI, "Etude thermophysique de la diffusion de molécules de bas poids moléculaire dans des réseaux de polymères acryliques." Université de Tlemcen-Abou Bekr Belkaid, 2013.

[127] L. Boukemara and C. Boukhalfa, "Etude de l'adsorption des ions phosphate sur des oxy-hydroxydes. Cas de l'hydroxyde de fer," 2009.

[128] N. A. Negm and A. M. El Sabagh, "Interaction between cationic and conventional nonionic surfactants in the mixed micelle and monolayer formed in aqueous medium," *Quim. Nova*, vol. 34, pp. 1007–1013, 2011.

[129] C. Vautier-Giongo and B. L. Bales, "Estimate of the ionization degree of ionic micelles based on Krafft temperature measurements," *J. Phys. Chem. B*, vol. 107, no. 23, pp. 5398–5403, 2003.

[130] T. Ribeiro *et al.*, "Silica nanocarriers with user-defined precise diameters by controlled template self-assembly," *J. Colloid Interface Sci.*, vol. 561, pp. 609–619, 2020.

[131] H. Chaimovich, J. B. S. Bonilha, M. J. Politi, and F. H. Quina, "Ion exchange in micellar solutions. 2. Binding of hydroxide ion to positive micelles," *J. Phys. Chem.*, vol. 83, no. 14, pp. 1851–1854, 1979.

[132] D. E. Mazouzi *et al.*, "Auto-combustion designed BiFeO3/Bi2O3 photocatalyst for improved photodegradation of nitrobenzene under visible light and sunlight irradiation," *Surfaces and Interfaces*, vol. 44, p. 103581, 2024.

[133] K. A. Naumova, O. V Dement'eva, I. N. Senchikhin, and V. M. Rudoy, "Mesoporous silica particles based on complex micelles of poorly water-soluble compounds. One simple step to multidrug carriers," *Microporous Mesoporous Mater.*, vol. 316, p. 110911, 2021.

[134] 김이중, "Aggregation of silica nanoparticles and its impact on particle mobility under

high-salinity conditions," 2015.

[135] R. P. Bagwe, L. R. Hilliard, and W. Tan, "Surface modification of silica nanoparticles to reduce aggregation and nonspecific binding," *Langmuir*, vol. 22, no. 9, pp. 4357–4362, 2006.

[136] R. J. Robson and E. A. Dennis, "The size, shape, and hydration of nonionic surfactant micelles. Triton X-100," *J. Phys. Chem.*, vol. 81, no. 11, pp. 1075–1078, 1977.

[137] T. Wang, W. Ma, J. Shangguan, W. Jiang, and Q. Zhong, "Controllable synthesis of hollow mesoporous silica spheres and application as support of nano-gold," *J. Solid State Chem.*, vol. 215, pp. 67–73, 2014.

[138] E. Mine, D. Nagao, Y. Kobayashi, and M. Konno, "Solvent effects on particle formation in hydrolysis of tetraethyl orthosilicate," *J. sol-gel Sci. Technol.*, vol. 35, pp. 197–201, 2005.

[139] R. K. Sharma *et al.*, "A novel BMSN (biologically synthesized mesoporous silica nanoparticles) material: synthesis using a bacteria-mediated biosurfactant and characterization," *RSC Adv.*, vol. 11, no. 52, pp. 32906–32916, 2021.

[140] R. K. Sharma *et al.*, "Influence of chemical and bio-surfactants on physiochemical properties in mesoporous silica nanoparticles synthesis," *J. Mater. Res. Technol.*, vol. 24, pp. 2629–2639, 2023.

[141] D. Jager, D. Kupka, M. Vaclavikova, L. Ivanicova, and G. Gallios, "Degradation of Reactive Black 5 by electrochemical oxidation," *Chemosphere*, vol. 190, pp. 405–416, 2018.

[142] T. Robinson, G. McMullan, R. Marchant, and P. Nigam, "Remediation of dyes in textile effluent: a critical review on current treatment technologies with a proposed alternative," *Bioresour. Technol.*, vol. 77, no. 3, pp. 247–255, 2001.

[143] A. Ramdani, S. Taleb, A. Benghalem, and N. Ghaffour, "Removal of excess fluoride ions from Saharan brackish water by adsorption on natural materials," *Desalination*, vol. 250, no. 1, pp. 408–413, 2010.

[144] N. Barka, A. Assabbane, A. Nounah, and Y. A. Ichou, "Photocatalytic degradation of indigo carmine in aqueous solution by TiO2-coated non-woven fibres," *J. Hazard. Mater.*, vol. 152, no. 3, pp. 1054–1059, 2008.

[145] M. Doğan, M. Alkan, A. Türkyilmaz, and Y. Özdemir, “Kinetics and mechanism of removal of methylene blue by adsorption onto perlite,” *J. Hazard. Mater.*, vol. 109, no. 1–3, pp. 141–148, 2004.

[146] M. Hajjaji and A. Alami, “Influence of operating conditions on methylene blue uptake by a smectite rich clay fraction,” *Appl. Clay Sci.*, vol. 44, no. 1–2, pp. 127–129, 2009.

[147] M. W. Munthali, E. Johan, H. Aono, and N. Matsue, “Cs+ and Sr2+ adsorption selectivity of zeolites in relation to radioactive decontamination,” *J. Asian Ceram. Soc.*, vol. 3, no. 3, pp. 245–250, 2015.

[148] S. Mirnezhad, S. Safapour, and M. Sadeghi-Kiakhani, “Dual-mode adsorption of cochineal natural dye on wool fibers: Kinetic, equilibrium, and thermodynamic studies,” *Fibers Polym.*, vol. 18, no. 6, pp. 1134–1145, 2017, doi: 10.1007/s12221-017-6923-3.

[149] N. Galaffu, K. Bortlik, and M. Michel, *An industry perspective on natural food colour stability*, no. 2. Elsevier Ltd., 2015. doi: 10.1016/B978-1-78242-011-8.00005-2.

[150] S. R. Shirsath, A. P. Patil, R. Patil, J. B. Naik, P. R. Gogate, and S. H. Sonawane, “Removal of Brilliant Green from wastewater using conventional and ultrasonically prepared poly (acrylic acid) hydrogel loaded with kaolin clay: a comparative study,” *Ultrason. Sonochem.*, vol. 20, no. 3, pp. 914–923, 2013.

[151] M. Ghaedi *et al.*, “A novel acorn based adsorbent for the removal of brilliant green,” *Desalination*, vol. 281, pp. 226–233, 2011.

[152] V. S. Mane and P. V. V. Babu, “Studies on the adsorption of Brilliant Green dye from aqueous solution onto low-cost NaOH treated saw dust,” *Desalination*, vol. 273, no. 2–3, pp. 321–329, 2011.

[153] M. P. Tavlieva, S. D. Genieva, V. G. Georgieva, and L. T. Vlaev, “Kinetic study of brilliant green adsorption from aqueous solution onto white rice husk ash,” *J. Colloid Interface Sci.*, vol. 409, pp. 112–122, 2013.

[154] Y. Miyah *et al.*, “Removal of cationic dye ‘crystal violet’ in aqueous solution by the local clay,” *J. Mater. Environ. Sci*, vol. 8, no. 10, pp. 3570–3582, 2017.

[155] R. Si, Y. Zhang, L. You, and C. Yan, “Rare-Earth oxide nanopolyhedra, nanoplates, and nanodisks,” *Angew. Chemie Int. Ed.*, vol. 44, no. 21, pp. 3256–3260, 2005.

[156] P. B. Sarawade, J.-K. Kim, A. Hilonga, and H. T. Kim, “Recovery of high surface area mesoporous silica from waste hexafluorosilicic acid (H2SiF6) of fertilizer industry,” *J. Hazard. Mater.*, vol. 173, no. 1–3, pp. 576–580, 2010.

[157] D. L. Griscom and E. J. Friebele, “Fundamental defect centers in glass: Si 29 hyperfine structure of the nonbridging oxygen hole center and the peroxy radical in a-Si O 2,” *Phys. Rev. B*, vol. 24, no. 8, p. 4896, 1981.

[158] D. P. Yu *et al.*, “Amorphous silica nanowires: Intensive blue light emitters,” *Appl. Phys. Lett.*, vol. 73, no. 21, pp. 3076–3078, 1998.